



universität
wien

DIPLOMARBEIT

Titel der Diplomarbeit

„First Steps of Implementation of Image Guided Adaptive
Radiation Therapy“

Verfasser

Johannes Hopfgartner

angestrebter akademischer Grad

Magister der Naturwissenschaften (Mag. rer.nat)

Wien, 2009

Studienkennzahl lt.
Studienblatt:

A 411

Studienrichtung lt.
Studienblatt:

Physik

Acknowledgement

Hereby, I would like to thank all the people, who contributed to the success of this work. Above all, I want to thank my parents, Margareth and Hubert Hopfgartner, who provided me the chance to study and supported me mentally and financially throughout the course of my studies.

Sincere thanks are given to Dipl.-Ing. Dr. Markus Stock for his great support and valuable advice. His guidance was of great endorsement for me and intensely helpful. Especially I am obliged to him for reviewing this thesis several times.

I am much indebted to Univ. Doz. Dipl.-Ing. Dr. Dietmar Georg, who made this thesis possible and provided an excellent research environment.

I would also like to express my gratitude to Prof. Dr. Richard Pötter, Head of the Department of Radiotherapy, Medical University of Vienna (MUW)/AKH Vienna, for the possibility to perform scientific work in his department.

I want to thank all the physicists and technicians for giving me helpful advises and assistance.

Last but not least, cordial thanks are due to all my colleagues and friends for their friendship, mental support and patience.

Eidesstattliche Erklärung

Hiermit versichere ich, dass ich diese Arbeit selbständig verfasst, keine anderen als die angegebenen Hilfsmittel benutzt und mich auch sonst keiner unerlaubten Hilfe bedient habe.

Wien, Juni 2009

Table of contents

Abbreviations	v
Motivation and Purpose of this study	ix
1 Basics of radiation therapy	1
1.1 Introduction	1
1.2 Radiation physics	2
1.2.1 Interactions of photons with matter	3
1.2.2 Coherent scattering	4
1.2.3 Photoelectric effect	5
1.2.4 Compton effect	7
1.2.5 Pair production	9
1.2.6 Relative importance of the various processes	10
1.2.7 Interaction of charged particles	11
1.3 New therapy options	15
1.3.1 Image Guided Radiation Therapy	15
1.3.2 Adaptive Radiation Therapy	15
1.4 Radiation therapy process	17
1.4.1 Volume definition	17
1.4.2 Treatment planning system	19
1.4.3 Dose calculation algorithms	19
1.4.4 Linear accelerator	21
1.4.5 Cone Beam Computed Tomography	22
1.4.5.1 Artifacts in CBCT	23
2 Materials and Methods	27
2.1 Linac	27
2.1.1 Flat panel detector	28
2.1.2 kV Imaging	28

2.1.3	<i>MV Imaging</i>	31
2.2	<i>Computed Tomography</i>	31
2.3	<i>Treatment planning system</i>	31
2.4	<i>Dosimetric equipment</i>	32
2.4.1	<i>Diodes</i>	32
2.4.2	<i>Ionization chambers</i>	33
2.5	<i>Phantoms</i>	34
2.5.1	<i>Dose measurement phantoms</i>	34
2.5.1.1	<i>Water phantom</i>	34
2.5.2	<i>Image quality phantoms</i>	36
2.5.2.1	<i>TOR 18 FG phantom</i>	36
2.5.2.2	<i>Cube phantom</i>	36
2.5.2.3	<i>CATPhan® phantom</i>	37
2.5.2.4	<i>Single ball bearing phantom</i>	38
2.5.3	<i>Electron density calibration phantoms</i>	39
2.5.3.1	<i>Gammex® RMI phantom</i>	39
2.5.4	<i>Dose calculation phantoms</i>	40
2.5.4.1	<i>Pelvis phantom</i>	40
2.5.4.2	<i>Multipurpose phantom</i>	40
3	<i>Quality Assurance of CBCT</i>	43
3.1	<i>General aspects</i>	43
3.2	<i>Customer Acceptance Test</i>	43
3.2.1	<i>QA in 2 dimensions</i>	44
3.2.1.1	<i>2D Low contrast visibility</i>	44
3.2.1.2	<i>2D Spatial resolution</i>	44
3.2.1.3	<i>2D Geometric accuracy</i>	45
3.2.1.4	<i>Off isocenter distance distortion</i>	45
3.2.2	<i>QA in 3 dimensions</i>	47
3.2.2.1	<i>Low contrast visibility</i>	47
3.2.2.2	<i>Image scale</i>	48
3.2.2.3	<i>Spatial resolution</i>	49

3.2.2.4	<i>Modulation Transfer Function</i>	50
3.2.2.5	<i>Uniformity</i>	53
3.2.2.6	<i>Registration and geometric accuracy tests</i>	54
3.2.3	<i>Table movement assistant accuracy</i>	56
4	<i>Basic Beam Data</i>	59
4.1	<i>Introduction</i>	59
4.2	<i>Nominal linac output</i>	59
4.3	<i>Percentage depth dose</i>	61
4.3.1	<i>Definition of the required data sets</i>	61
4.3.2	<i>Results</i>	61
4.4	<i>Dose profiles</i>	66
4.4.1	<i>Definition of the required data sets</i>	66
4.4.2	<i>Diagonal radial dose profiles</i>	67
4.4.2.1	<i>Measurement setup</i>	67
4.4.2.2	<i>Results</i>	68
4.4.3	<i>Transversal dose profiles</i>	69
4.4.3.1	<i>Penumbra</i>	70
4.4.3.2	<i>Measurement setup</i>	71
4.4.3.3	<i>Results</i>	72
4.5	<i>Scatter factors</i>	76
4.5.1	<i>Definition</i>	76
4.5.2	<i>Results</i>	78
4.6	<i>Acceptance and commissioning of iPlan® TPS</i>	80
4.6.1	<i>Gamma evaluation</i>	80
4.6.2	<i>Results</i>	82
5	<i>Adaptive Dose Calculation</i>	89
5.1	<i>Introduction</i>	89
5.2	<i>Hounsfield units</i>	90

5.3	<i>HU/ED calibration curves</i>	90
5.3.1	<i>Scanning parameter dependency</i>	96
5.3.2	<i>Temporal stability</i>	97
5.4	<i>Dose difference due to curve exchange</i>	99
5.5	<i>Dose comparison</i>	102
5.5.1	<i>Preparations and methods</i>	102
5.5.2	<i>Results</i>	104
6	<i>Summary and outlook</i>	111
	<i>Bibliography</i>	115
	<i>Abstract</i>	119
	<i>Zusammenfassung</i>	121
	<i>Curriculum vitae</i>	125

Abbreviations

3D	three dimensional
AKH	Allgemeines Krankenhaus
AP	Anterior - Posterior
ART	Adaptive Radiation Therapy
BTF	Bow Tie Filter
CAT	Customer Acceptance Test
CBCT	Cone Beam Computed Tomography
CRT	Conformal Radiation Therapy
CT	Computed Tomography
CTV	Clinical Target Volume
DR	Dose Rate
DTA	Distance To Agreement
ED	Electron Density
EPID	Electronic Portal Imaging Device
FOV	Field Of View
FS	Field Size
GTV	Gross Tumor Volume
H&N	Head and Neck
HU	Hounsfield Unit
IEC	International Electrotechnical Commission
IGRT	Image Guided Radiation Therapy
IMRT	Intensity Modeled Radiation Therapy
IQ	Image Quality
kV	Kilo Voltage
L	Large
LC	Low Contrast
LCV	Low Contrast Visibility
LDPE	Low Density Polyethylene
Linac	Linear Accelerator
M	Medium
MCA	Monte Carlo Algorithm

MLC	Multi Leaf Collimator
MPD	Maximum Percentage Difference
MTF	Modulation Transfer Function
MU	Monitor Unit
MUW	Medizinische Universität Wien
MV	Mega Voltage
OAR	Organs At Risk
OP	Output
OPF	Output Factor
PBA	Pencil Beam Algorithm
pCT	Planning CT
PDD	Percentage Depth Dose
PSF	Point Spread Function
PSR	Phantom Scatter Ratio
PTV	Planning Target Volume
QA	Quality Assurance
ROI	Region Of Interest
RT	Radiation Therapy
S	Small
SSD	Source to Surface Distance
TPS	Treatment Planning System
TSF	Total Scatter Factor

Motivation and purpose of this study

The overall aim of Radiation Therapy (RT) treatments is to achieve maximum dose to the tumor volume while sparing surrounding tissue as much as possible. Modern linear accelerators (Linacs) are not only designed to deliver the requested dose to the tumor volume, but also to ensure that targets are accurately localized at treatment by use of volumetric image guidance. It is absolutely important that the patient's positioning is precise and reproducible and the tumor is localized accurately during the course of all fractions, in which a radiation therapy is split [1].

Recently, the new concept of Adaptive Radiation Therapy (ART) has been developed. In ART, one or multiple modifications of the initial irradiation plan take place between single fractions. With the adaptation of the irradiation plan, anatomical changes in the patient as well as positioning uncertainties are taken into account. With the help of Cone Beam Computed Tomography (CBCT) it is possible to detect and monitor such changes. As a consequence of this, the size of the Planning Target Volume (PTV) may be decreased, which leads to sparing of surrounding tissue and hence eventual Organs At Risk (OAR). According to these recently acquired data sets a new, adapted irradiation plan can be provided steadily by the Treatment Planning System (TPS).

In the context of this diploma thesis an extensive Quality Assurance (QA) of the CBCT device, which represents the principle tool of ART, is fulfilled. The new technology of such CBCT devices and their inclusion in the ART process demands an accurate detection of tolerances of Image Quality (IQ) and geometrical uncertainties. This is necessary, because the decisions of radiation oncologists regarding patient repositioning and/or plan adaptation are based on CBCT images. The stability of IQ and indirectly the entire image reconstruction should be investigated. Additionally, the precision of the treatment couch and other geometrical uncertainties have to be determined. It is crucial to develop a device specific protocol of QA to monitor the workflow and to determine eventual time trends in image quality. The QA is a continuation of the M.Sc. project carried out by Mag. Marlies Pasler in 2008 [2].

To satisfy the requirement for accuracy evaluation of CBCT based dose calculation for ART, a powerful TPS is requested. For subsequent dose calculation and comparison purposes, the TPS iPlan® of BrainLAB was benchmarked. For iPlan®, the dose calculation accuracy of 6 MV, 10 MV and 18 MV photon beams, provided by our treatment machine, was determined. These studies encompass the basic beam datasets required by iPlan® for the Pencil Beam (PBA) as well as for the Monte Carlo (MCA) dose calculation algorithm. Nominally, depth dose curves, dose profiles and dosimetric quantities describing beam quality like scatter factors and linac output were measured. These basic beam data sets are the basis for tuning the dose calculation algorithms in the TPS.

The final part of the thesis focuses on the applicability of CBCT data sets for ART. Most of interest was if CBCT images can be used for dose calculations and how accuracy is influenced by CBCT image technology. An important step regarding this is the relation of Hounsfield Units (HU) to Electron Density (ED) as well as the constancy of HUs of CBCT images for different image protocols. The reliability on dose calculation, based on CBCT images, has to be verified by comparing simple dose distributions, calculated by iPlan® to CT based calculation.

1 Basics of radiation therapy

1.1 Introduction

Generally, there are two techniques in radiation therapy, external beam radiotherapy, known as teletherapy, and brachytherapy. Teletherapy is the most frequently used form of radiotherapy, whereby dose is delivered to the patient by an external radiation source. About 90% of the radiation used in external radiotherapy is photon radiation. On the other hand, brachytherapy uses radioactive seed-sources to deliver dose at short distances to the tumor either by intercavitary, intravascular or interstitial application.

In order to provide the patient with the most benefitting therapy, an adequate treatment technique must be chosen and the appropriate treatment plan must be created. A TPS, which allows computation and optimization of the dose distribution in accordance with the clinical objectives and a compatible accelerator able to deliver the required beams, are needed.

Not only physical and technical aspects, but also radiobiology, must be taken into account when handling with radiation therapy. The maximum dose coverage of malign tissue and contemporary minimal exposure of the healthy tissue does not only depend on spatial dose distribution. Temporal dose distribution, so named fractionation, plays an important role as well. Direct strikes of radiation provoke DNA strand breaks, which above all induce the desired damage to the tumor. Exposure of biological tissue to ionizing radiation leads to ionization and excitation of their constituent atoms. These damage effects are caused by basic physical effects, which are explained in the following sections. The molecules, where these atoms reside, tend to fall apart resulting in so called free radicals. Water is the predominant molecule within cells, so most of the free radicals are produced by its radiolysis. Free radicals are highly unstable. They react with other nearby molecules, thereby transferring chemical damage to them.

Experimental methods have been developed to detect the recovery of tumor cells and tissue from radiation exposure. These recovery processes are of direct relevance

to clinical RT, because the effect of a given radiation dose is less if split into several fractions that are delivered a few hours or longer apart. This is utilized in RT to allow predominantly healthy tissue to recover [3]. For such purposes, the fact that tumor tissue recovers slower than healthy tissue is exploited. An acceptable ratio between them has to be found for an adequate therapy success.

Chapter 1 is meant to represent a brief overview of the basics of radiation physics and a brief introduction into the most commonly used devices of photon therapy. Additionally, several modern treatment techniques are discussed.

1.2 Radiation physics

In clinical practice there are different types of radiation utilized. Approximately 90% consist of electromagnetic waves like X- or Gamma rays. The other 10 % comprise charged particles such as electrons, protons or heavier ions.

The energy range of the photons used in medicine spreads from low energies (several keV) to very high energies (up to 50 MeV) [5]. Such photons can be produced either in X-ray tubes or by accelerators. In both cases, the produced radiation has not a discrete but a continuous spectrum, so called bremsstrahlung spectrum. In such spectra, the mean energy is known to be approximately one third of the maximal energy, which characterizes the spectrum. In the next paragraphs, which are dedicated to a description of basic interaction processes, the photon radiation is assumed to be monoenergetic.

When photons interact with atoms of an absorbing material (in medicine the human tissue), single photons are either absorbed or scattered. If such an interaction occurs, either charged particles, like electrons or positrons, or again photons are emitted. Charged particles deposit their kinetic energy close to their appearance site and hence contribute to the local energy deposition. As a consequence of such energy depositions, surrounding matter is ionized and consequently cells can lose their reproductive capability. It is very important to consider secondary photons because they contribute on the one hand to the photon fluence inside and outside the irradiated body and on the other hand to the dose when they produce secondary electrons [3].

1.2.1 Interaction of photons with matter

The reduction of photon number, when an X- or gamma ray passes through absorbing matter, is proportional to the number of incident photons and to the thickness of the absorbing layer. The proportionality constant is μ , the so called linear attenuation coefficient. Mathematically, this relationship is depicted by the following equation.

$$dN = -\mu \cdot N \cdot dx \quad (1.1)$$

The minus in equation (1.1) indicates that the number of photons decreases as the absorber thickness increases. The physical meaning of μ is clearly apparent if one keeps in mind, that it is the quotient of the relative number of the loss of primary photons and the thickness dx . If the thickness of the absorbing medium is given in centimeters, the unit of μ is 1/cm. μ is related to the energy of the incident photons, the atomic mass A and the density ρ of the absorbing material and to the atomic cross section σ . The relationship is expressed in the subsequent formula.

$$\mu(A, \rho, \sigma) = \frac{N_A}{A} \cdot \rho \cdot \sigma \quad (1.2)$$

Where N_A is the Avogadro constant.

The number of photons can be directly classified in terms of intensity. The result is as follows.

$$dI = -\mu \cdot I \cdot dx \quad (1.3)$$

This equation is identical with the equation of the radioactive decay, when the linear attenuation coefficient μ is exchanged by the radioactive decay constant λ . It can be basically solved, which leads to the following equation that describes the attenuation of the beam.

$$I(x) = I_0 \cdot e^{-\mu \cdot x} \quad (1.4)$$

$I(x)$ stands for the transmitted intensity and I_0 for the incident intensity on the absorber.

In practice, often the so called mass attenuation coefficient μ/ρ is used. It is simply derived from equation (1.2) by dividing it with the density ρ of the attenuating medium. As a consequence of this, the recently obtained quantity is density independent and hence easier to handle. μ/ρ has the unit cm^2 / g . Thus, in equation (1.4) the absorber thickness should be expressed as ρx in order to obtain unity in terms of units in the exponent of the exponential function.

The mass attenuation coefficient is a characteristic constant of the absorbing medium and it is additively composed of the different coefficients of the particular photon interactions, which is illustrated in equation (1.5). Attenuation of photons in matter is principally caused by 4 processes: Coherent scattering, Photoelectric effect, Compton scattering and pair production. Each of the mentioned processes can be characterized by a proper attenuation coefficient, namely σ_{coh} , τ , σ_C and π respectively.

$$\frac{\mu}{\rho} = \frac{\sigma_{coh} + \tau + \sigma_C + \pi}{\rho} \quad (1.5)$$

The particular processes of photon interaction are described in the next sections.

1.2.2 Coherent scattering

Coherent scattering, also termed Rayleigh scattering, is a consequence of the wave nature of electromagnetic radiation. The interaction consists of an electromagnetic wave passing near an electron and forcing it to oscillate. The only arising effect is scattering of the incident photons at small angles. Since no energy is absorbed in the medium, the scattered X-ray has the same wavelength as the incident beam. Coherent scattering is probable in materials with high atomic numbers and for photons with low energy. Such low energies are not used in radiation therapy, because they do not lead to destruction of irradiated tissue and consequently tumor control. The process is illustrated in figure (1.1).

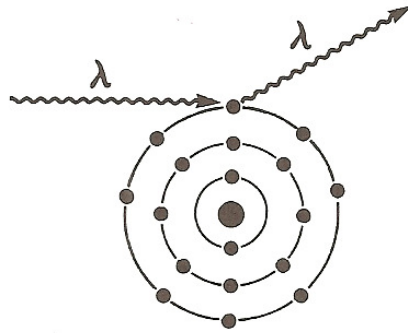


Figure 1.1: Coherent scattering [6, p.65]

1.2.3 Photoelectric effect

For this reaction process, an incoming photon interacts with the electronic shell of an atom and ejects one of its orbital electrons. Thereby the entire energy $h\nu$ of the incident photon is transferred to the electron, which is located either in the K- L- or M-shell. The electron adopts the difference between the energy of the incident photon and its binding energy as kinetic energy. For the photoelectric effect in order to take place, the energy of the photon needs to be higher than the binding energy of the ejected electron.

The cross section diagram shows discontinuities at such photon energies, which correspond to the binding energies in atomic shells. These discontinuities are named absorption edges of electronic shells and they are shown for lead and water in figure (1.2). The angular distribution of electrons emitted by a photoelectric effect strongly depends on the incident photon energy. As photon energy increases, electrons are more and more emitted in forward direction.

The vacancy in the atomic shell, which is generated by the ejection of one of its inner electrons, can be immediately refilled by an outer electron by the emission of so called characteristic X-rays. Another option to suspend the excited state of the atom is the emission of Auger electrons, which have discrete energy spectra.

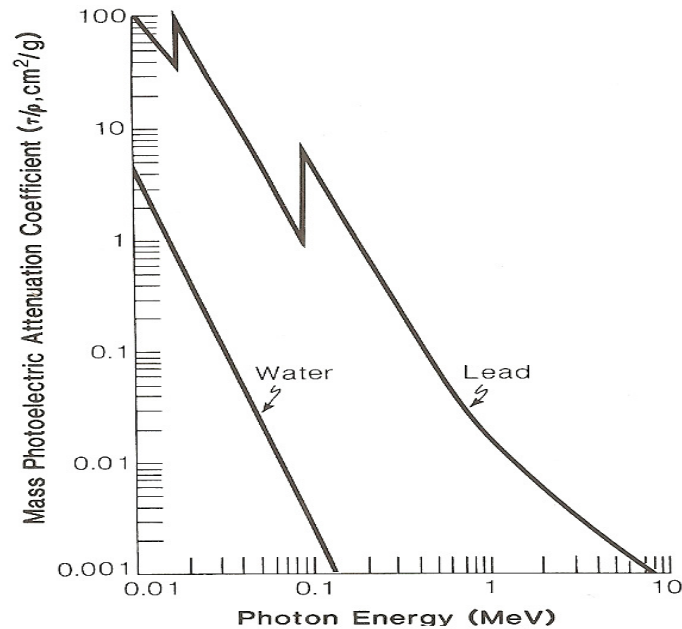


Figure 1.2: Absorption edges [6, p.66]

Auger electrons are produced due to the immediate absorption of characteristic X-rays by another shell electron, which is consequently ejected. The Auger process can somehow be interpreted as an inner secondary photoelectric effect triggered by a primary one. A graphical illustration of the photoelectric effect is given in figure (1.3).

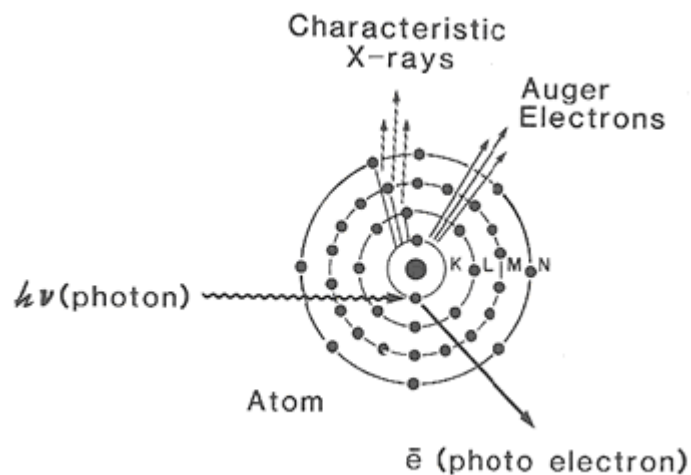


Figure 1.3: Photoelectric effect [6, p.65]

The probability of a photoelectric effect to take place depends on the incident photon energy E , the atomic number Z of the absorber and its density.

The relation between them is delineated by the following equation.

$$\frac{\tau}{\rho} \propto \frac{Z^n}{E^3} \quad (1.6)$$

Here, n ranges from 3 up to 5 depending on the atomic number. It is larger for light elements and smaller for their heavy counterparts.

1.2.4 Compton effect

Compton interaction is an effect that can occur with an incident photon and an electron of the atomic shell, which is considered to be 'quasi free'. Quasi free is a term which characterizes the binding energy of the atomic electron in relation to the energy of the incident photon.

When a Compton scatter event occurs, the electron assumes part of photon's energy and momentum and leaves the atomic shell at an angle θ relative to the direction of the incident photon. The photon, with former energy $h\nu$, is scattered at an angle Φ and its energy lowers due to this interaction. The process is depicted in figure (1.4).

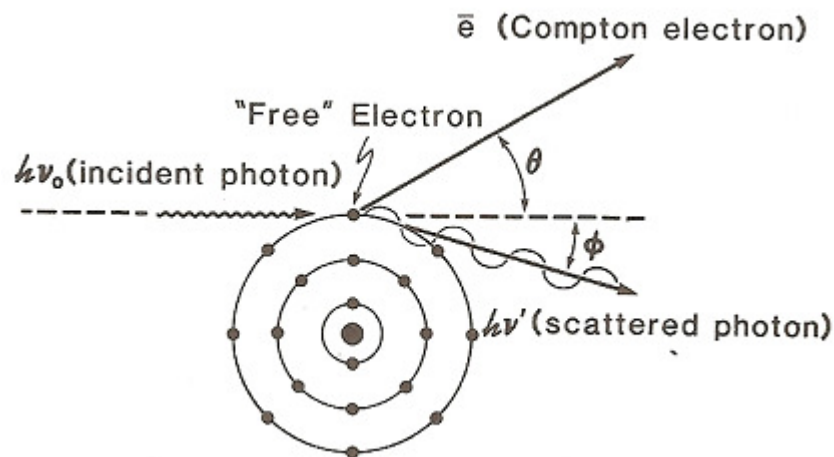


Figure 1.4: Compton effect [6, p.67]

The Compton process can mathematically be deduced from the laws of conservation of energy and momentum, by imagining a collision between two particles, an electron and a photon. The energy $h\nu'$ of the scattered photon is given by equation (1.7), whereas m_e is the mass of the electron and c is the light speed.

$$h\nu' = \frac{h\nu}{1 + \frac{h\nu}{m_e \cdot c^2} \cdot (1 - \cos(\Phi))} \quad (1.7)$$

Equation (1.7), where values from 0° to 180° can be obtained for Φ , shows that the photon loses no energy when scattered in forward direction, which means that the electron is emitted perpendicular to the incident photon direction. The forward scatter probability increases with rising energy of the incoming photon.

By backward scattering, the photon loses the largest fraction of its energy by transferring it to the electron. The first requirement for the Compton effect is that the incident photon energy must be large compared with the binding energy of the electron. This stands in contrast to the photoelectric effect, which becomes most probable when the energy of the photon is equal or slightly greater than the binding energy.

The probability of the Compton effect is characterized with the Compton attenuation coefficient, which comprises the Compton scatter coefficient $\sigma_{scatter}$ and the Compton energy transfer coefficient σ_{tr} as shown in equation (1.8).

$$\sigma_C = \sigma_{scatter} + \sigma_{tr} \quad (1.8)$$

Because in the Compton interaction quasi free electrons are involved, it is independent on atomic number. The only atomic parameter that influences the Compton cross section is the number of electrons per atom. This is also intuitively understandable concerning the electronic screen effect of the nuclear Coulomb potential provoked by the inner electrons. Like all other attenuation coefficients, the Compton coefficient is proportional to the density of the absorber material. The dependency on the photon energy in Compton effect dominated materials at

energies between 0.2 MeV and 10 MeV can be described approximately by the following expression.

$$\frac{\sigma_c}{\rho} \propto \frac{1}{\sqrt{E}} \quad (1.9)$$

1.2.5 Pair production

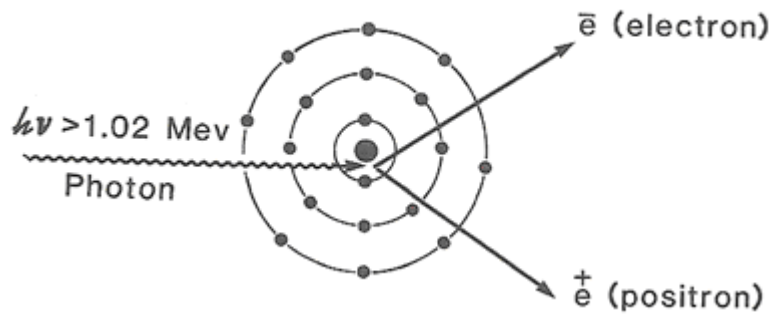


Figure 1.5: Pair production [6, p.71]

If the energy of the incoming photon exceeds 1.022 MeV, it might interact with material by the mechanism of pair production. In this case, strong interaction of the incident photon and the electromagnetic field of the nucleus takes place (figure 1.5). The photon immediately loses all of its energy by generating a pair of an electron and a positron. The exact amount of 1.022 MeV is required in order to satisfy the energy equivalent of the rest masses of the antimatter- matter pair. Photon energy in excess of this threshold energy is shared between the two particles as kinetic energy. The total kinetic energy available for the electron-positron pair is given by

$$E_{kin} = (h\nu - 2 \cdot m_0 \cdot c^2) = (h\nu - 1,022) \text{ MeV} \quad (1.10)$$

The produced particles tend to be emitted in forward direction relative to the incident photon. It is most probable that each particle achieves half of the available energy, but other energy distributions are possible as well. After generation of the antimatter-matter pair, both particles excite and ionize surrounding matter while traversing it. As the positron slows down, it combines with a nearby free electron, what gives rise to

so named annihilation radiation. Annihilation radiation comprises two photons of 511 keV leaving each other in opposite direction due to conservation of momentum.

Evidently, the probability of pair production to take place is dependent on the atomic number of the absorbing material because the process itself results from interaction with the electromagnetic field of the nucleus.

The following equation states the relationship between the attenuation coefficient of pair production, incident photon energy and atomic number, respectively.

$$\frac{\pi}{\rho} \propto Z \cdot \log E \quad (1.11)$$

1.2.6 Relative importance of the various processes

As mentioned in previous explanations, the various basic interaction processes all depend differently on incident photon energy and atomic number in more or less complicated ways.

Equation (1.5) states that the total mass attenuation coefficient is the sum of the individual mass attenuation coefficients belonging to the diverse processes. Figure (1.6) depicts the relative importance of the various interaction mechanisms. Coherent scattering has been omitted, because as already stated, it doesn't play a significant role according to therapeutic photon energies.

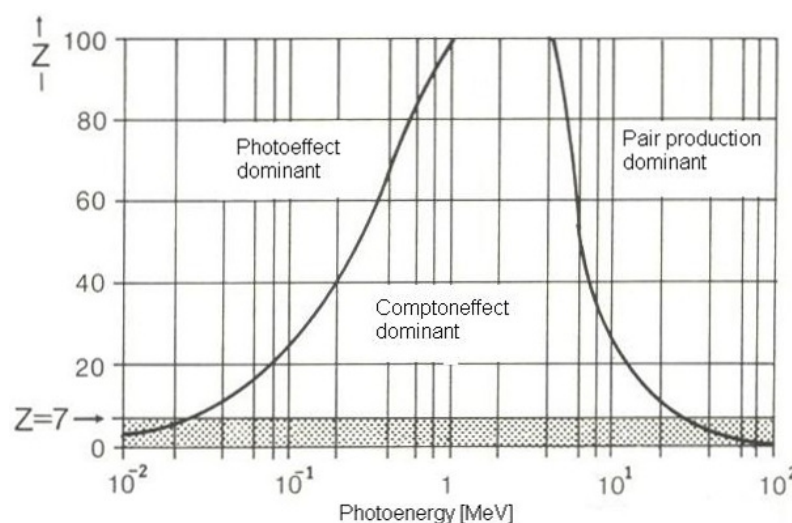


Figure 1.6: Area diagram of interaction probability, displaying regions of predominant effects [5, p.125]

The materials subjected to radiation therapy, for instance human tissue and phantoms, have effective atomic numbers between 7 and 8. Concerning this, the lower pointed area represents the relevant part. For human tissue, Compton effect is the predominant effect.

In the energy region of the Compton effect, the total mass attenuation coefficients of different materials do not differ greatly, since this type of interaction is independent of atomic number.

However, the attenuation coefficient of the photoelectric effect decreases with increasing energy and at energy of 20 MeV the pair production process becomes essential for materials with low atomic numbers.

Materials used for radiation safety, like tungsten or lead, are heavy elements with high atomic number and therefore characterized by higher leveled horizontal lines.

More detailed explanation regarding interactions processes of photons can be found in [5] and [6].

1.2.7 Interaction of charged particles

So far, uncharged photons have been protagonists of consideration. The following section gives a short overview of interaction of charged particles. It is based on the corresponding chapters in [5] and [6]. More detailed information can be found there if desired.

The interaction of charged particles can be split and explained separately into two parts. First part is the direct interaction of slow particles with the atom. In such a case an electron strikes another electron directly. This results in ionization and excitation of the atom. Its counterpart, involving high electron energies, is the interaction between the electromagnetic field of the atomic nucleus and the incidental electron. The second process is named Coulomb scattering, if an electron undergoes scattering without a significant energy loss. On the other hand it is called bremsstrahlung production, if electrons lose part of their energy, which is then transformed into photon radiation. In confrontation with heavier charged particles, electrons undergo greater multiple scattering and changes in direction of motion due to their much smaller mass. All of the following considerations involve relativistic electrons, because electron velocities in RT always exceed one tenth of light speed.

Due to the continuous energy loss caused by excitation and ionization, electrons have a finite penetration depth in matter. In human tissue this might be synonymous with an average range of a few centimeters.

A physical quantity, which can be utilized to characterize the kinetic energy loss per unit path length, is the stopping power.

The largest part of energy is lost by inelastic scattering of the electron with the atomic shell. The transferred energy is released in form of infrared light after the recombination of the shell electrons. This radiation leads to heating of the absorber. The collision stopping power S_{Col} , the quotient of the energy loss of an electron to its covered distance, is a material specific constant of the absorber. S_{Col} is proportional to the density and to the quotient of the atomic- to the mass number of the medium and indirect proportional to the energy of the electron. The following equation can be used for handling the mass collision stopping power mathematically.

$$\frac{S_{Col}}{\rho} \propto \frac{Z}{A} \cdot \frac{m_e}{E} \quad (1.12)$$

The second phenomenon includes the energy loss by the interaction of the Coulomb field of the atomic nucleus with any charged particle. By passing the nucleus at small impact parameters, charged particles suffer from deflection and acceleration and consequent energy losses through bremsstrahlung. Energy degradation increases with bending angle and reduction of the impact parameter. The grade of energy loss also depends on the energy of the projectile and the intensity of the nuclear Coulomb field. It is furthermore dependent on density and atomic number of the absorbing material. Summarizing all of these proportionalities, formula (1.13) can be used to express the mass radiation stopping power.

$$\frac{S_{Rad}}{\rho} = \left(\frac{e}{m}\right)^2 \cdot Z^2 \cdot E \quad (1.13)$$

The produced spectrum is continuous as a result of the randomized impact parameters. It is not emitted uniformly in all directions. For low electron energies (under 100 keV) the maximum of emission occurs laterally at 60 - 90 degrees to the incident electron beam.

The higher the electron energy, the more the spectrum is forward peaked, as shown in figure (1.7).

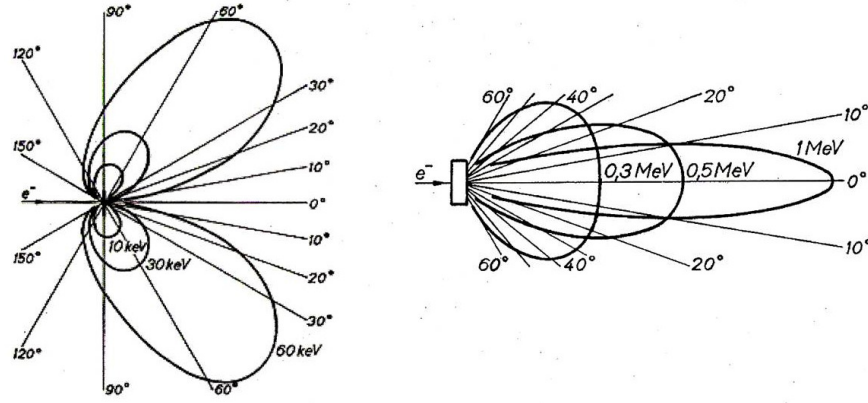


Figure 1.7: Angular distribution of bremsstrahlung spectra [5, p.168]

The total energy loss per unit path length is the sum of both of the contributing mechanisms and it is classified in terms of the total mass stopping power.

$$\left(\frac{S}{\rho}\right)_{Tot} = \frac{S_{Col} + S_{Rad}}{\rho} \quad (1.14)$$

The ratio of S_{Col} and S_{Rad} depends on the energy of the incoming electron, as described by the following equations.

$$E > 500\text{keV:} \quad \frac{S_{Rad}}{S_{Col}} \approx \frac{Z \cdot E}{800} \quad (1.15)$$

$$E < 150\text{keV:} \quad \frac{S_{Rad}}{S_{Col}} \approx \frac{Z \cdot E}{1400} \quad (1.16)$$

In figure (1.8), the mass stopping power and the mass radiation stopping power of electrons in different materials are depicted as function of their kinetic energy.

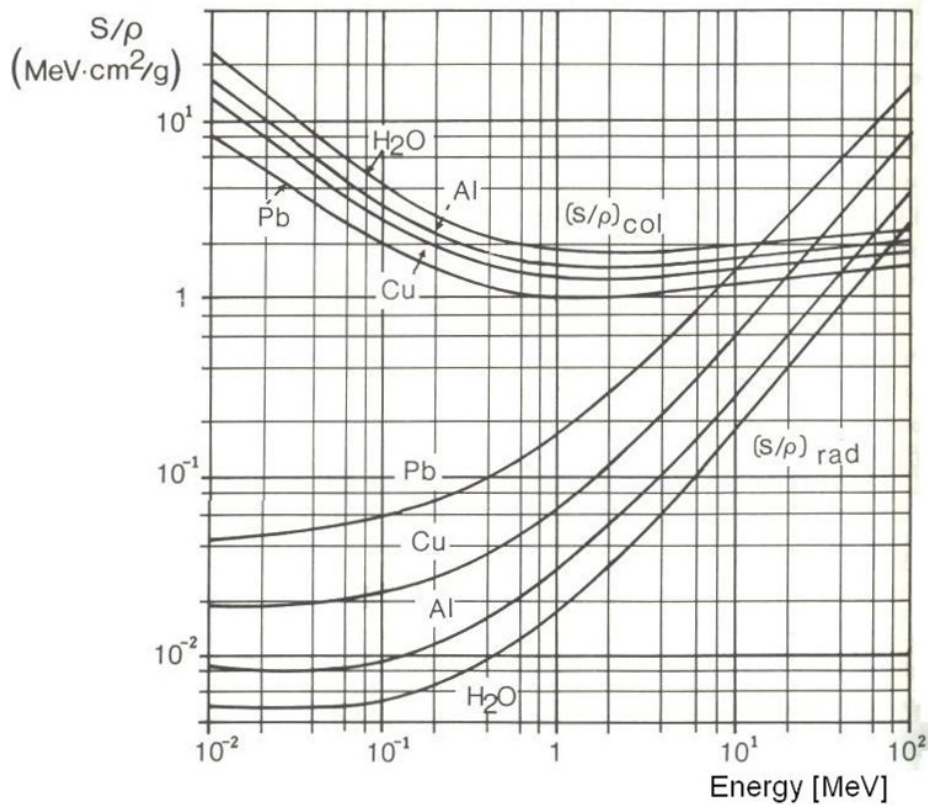


Figure: 1.8: Mass collision - and radiation stopping power as a function of energy [5, p.170]

The principal interest of dosimetry is the local energy deposition, because it is directly related to the biological effects in the cell.

The bremsstrahlung process, which forms the principal mechanism of photon production in linear accelerators, does barely contribute to the local energy deposition, because the thereby emerged photon radiation is very pervasive. As a consequence of this the so called restricted stopping power $S_{Col,\Delta}$ is introduced in radiation dosimetry, whereas Δ represents the upper barrier of the energy, which is taken into account for considerations of the local energy deposition.

1.3 New therapy options

1.3.1 Image Guided Radiation Therapy

New treatment technologies like Intensity Modulated Radiation Therapy (IMRT) can only deploy their full potential, if the patient and the tumor are positioned reproducibly during the course of all treatment fractions.

Image Guided Radiation Therapy (IGRT) denotes the process of localizing the target position by using imaging modalities in direct conjunction with the treatment [2]. Generally, generous safety margins are applied around the target and optionally OAR such that under- and overtreatment due to geometrical uncertainties can be avoided with an acceptable probability. By reducing inaccuracies, tighter margins can safely be applied to reduce exposure of OAR or to improve local control through dose escalation. For this reason, a variety of IGRT systems have been devised that allow verification and correction of the target position prior to each RT session [4]. Integrated options in the treatment room, so called in-room modalities, are kV X-ray imaging, MV portal imaging or megavoltage and kilovoltage CBCT, for instance. IGRT- techniques all rely on comparison of images acquired prior to the treatment with reference images of patient's anatomy in order to guarantee coincidence of treatment delivery and treatment planning.

1.3.2 Adaptive Radiation Therapy

Adaptive Radiation Therapy (ART) is directly related to IGRT. By the use of imaging modalities, tumor volumes as well as healthy tissue can be clearly detected. Volumetric images, as provided by CBCT, can be used for frequent verification of the setup of the patient and for correction of eventual positioning uncertainties. The problem occurring by changes in patient's anatomy and simultaneous dose escalation in healthy tissue is solvable with the application of altered irradiation plans on a regular basis.

In contradiction to a more or less static treatment approach, where the planning CT (pCT) based irradiation plan is not modified over the period of all fractions, ART takes into account anatomical changes. These changes could be weight loss, filling levels of bladder and shrinking of the tumor. A logical consequence of IGRT using CBCT images is to use them to recalculate the treatment plan according to patient's anatomy at the treatment day. A current challenge in ART is the research on how treatment plans can be added. Cumulative dose concerning PTV and OAR (see section 1.4.1), composed of individual treatment plan doses is a question of highest interest.

1.4 Radiation therapy process

1.4.1 Volume definition

The process of radiation therapy for tumor treatment involves many steps. One crucial step in the workflow is the determination of the location and the extent of the tumor relative to healthy tissue [7]. This process can be realized through various imaging techniques or a fusion of them. As the most common technology CT might be mentioned due to the coincident application for dose calculation. CT images are needed for the last purpose, because they provide the required information on attenuation coefficients of the tissue for the dose calculation algorithms. Such information is provided in terms of CT numbers or Hounsfield Units (HU) (see section (5.2)).

As a next step various volumes have to be identified and delineated. This is crucial for the treatment planning system in order to be able to calculate dose distributions and optimize treatment plans.

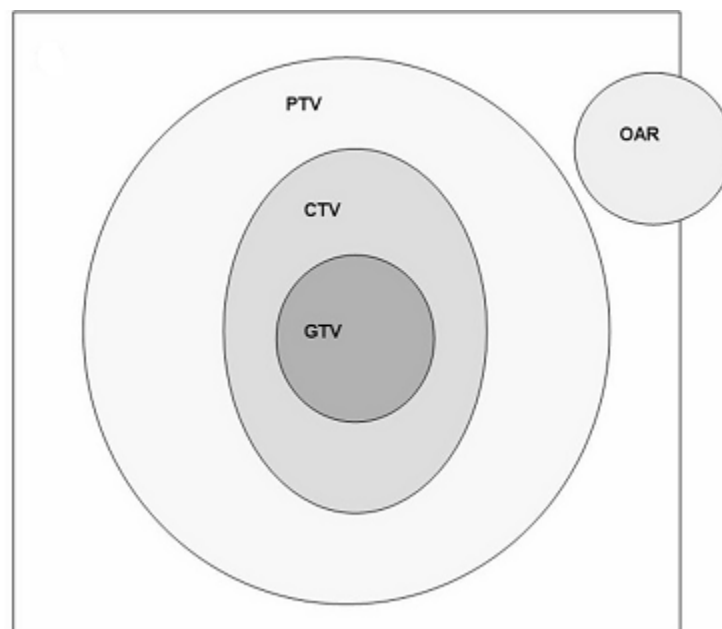


Figure 1.9: Volume concept in radiation oncology

In figure (1.9), the various volumes considered in radiation oncology are depicted. These standardized volumes are recommended in the ICRU reports No. 50 [8] and 62 [24]. They are described in more detail as follows.

Gross Tumor Volume (GTV)

The GTV is '*the gross visible/demonstrable extend and location of malignant growth*' [8]. GTV is build up of the primary tumor and its metastases.

Clinical Target Volume (CTV)

As demonstrated in clinical practice, there are generally microscopic focuses of disease located around the GTV. The CTV is '*a tissue volume that contains a demonstrable GTV and/or subclinical microscopic malignant disease, which has to be eliminated. This volume thus has to be treated adequately in order to achieve the aim of therapy, cure or palliation*' [8].

Planning Target Volume (PTV)

In theory, CTV is a fixed, static volume, which can be directly treated. In clinical practice it always comes to repositioning and other geometrical uncertainties for each fraction of treatment such as motion of the patient and mechanical setup inaccuracies such as field size, gantry angles and so on. For such possible alterations, the CTV has to be extended. The PTV is clarified as '*a geometrical concept, and it is defined to select appropriate beam sizes and beam arrangements, taking into consideration the net effect of all the possible geometrical variations, in order to ensure that the prescribed dose is actually absorbed in the CTV*' [8].

Organs At Risk (OAR)

Organs at risk are defined as tissue sites, which have to be spared as good as possible. It has to be found a consensus between sparing the OAR and delivering requested dose to the CTV.

Essential for meeting these goals are imaging devices, a planning workstation able to calculate required dose distributions and a linac with the equipment to deliver the desired dose.

1.4.2 Treatment planning system

In most of modern treatment techniques, a Treatment Planning System (TPS) is required. The task of the TPS is to calculate dose distributions accurately and fast. The knowledge of dose distribution is crucial for simulating the irradiation session in order to adjust beams and fields to cover the PTV with adequate dose and to spare OAR.

The TPS must be configured to simulate the treatment machine in order to provide specific treatment plans. Thus, every TPS requests a specific set of basic input data, which are the dosimetric characteristics of the linac that delivers the treatment.

After the implementation of the required basic beam data sets, the TPS is able to calculate the dose distribution in terms of dose calculation algorithms, which are explained briefly in the next chapter. Additionally, treatment plan parameters such as linac gantry angles and field sizes (FS) can be inputted into the TPS in order to shape and optimize the calculated dose distributions.

1.4.3 Dose calculation algorithms

'The intent of a dose calculation algorithm is to predict, with as much accuracy as possible, the dose delivered to any point within the patient' [7].

Dose algorithms are limited according to the boundary conditions stated in the underlying physical models. Consequently there are substantial inaccuracies under other circumstances. Different treatment scenarios require different accuracy so that dose calculation algorithms have to be chosen adequately.

Generally, dose calculation algorithms can be classified in three categories: Correction based-, Model based- and direct Monte Carlo method.

Correction based method

The class of correction based algorithms is semi empirical. They rely predominantly on measured data sets and are subsequently modified with several empiric correction functions and factors regarding attenuation, scattering, and radiologic path length. As a general example, the following equation can be considered.

$$D(x, y, z, c) = D_R \cdot \frac{K_1(c)}{D_R} \cdot \frac{K_2(z)}{K_1(c)} \cdot \dots \cdot \frac{K_n(z)}{K_{n-1}(.)} \quad (1.17)$$

Here, the index R refers to reference conditions, which denotes the circumstances under which the reference measurement took place. The various K_n stand for correction factors according to the above mentioned modifications of the reference dose.

Generally, their dose prediction accuracy is limited. Here, they are not discussed in too much detail.

Model based method

In this case, dose calculation is performed by applying (semi-) analytical models in order to simulate radiation transport. As a representative equation characterizing one class of model based algorithms, the following equation can be taken.

$$D(x, y, z) = \iint \Phi_{2D}(x', y') \cdot K_{pencil}(x', y', x, y, z) dx' dy' \quad (1.18)$$

Equation (1.18) is used for a description of the so called class of Pencil Beam Algorithms (PBA). The PBA was chosen here over the more general case of point dose algorithms, because it is amongst other used in iPlan® for the underlying study. In the formula above, K characterizes a so called scatter kernel, which is dependent on the particular geometric boundary conditions. A kernel can be considered as an energy distribution spread from a scattering point towards downstream voxels. The quantity Φ is proportional to the primary photon fluence incident upon the surface of the scatter kernel. By performing a convolution operation, the dose $D(x, y, z)$ in a point of interest (x, y, z) can be obtained. As further dose calculation algorithms, concerning the model based method, slab beam and point dose algorithms can be mentioned. They are chosen depending on the desired accuracy and geometrical requirements. The corresponding scatter kernels can be obtained either by measurements or by Monte Carlo computations. The model based methods and the in the next section outlined Monte Carlo method represent the most sophisticated dose calculation algorithms [6].

Direct Monte Carlo method

Regarding MCA, huge numbers of particles undergo virtual scattering processes towards a desired point of interest. Fundamental physical laws are taken as a basis for estimating probability distributions of individual interactions. Dose distribution is afterwards computed by accumulating ionization events in expressive voxels, hence absorbed dose. Unfortunately, for clinical acceptable precision of dose calculation, histories of billions of particles or photons have to be considered, which leads to excessively long computation times. Nevertheless, a balance between workload and benefit has to be found because considering accuracy, MCA is unmatched. Other than that mentioned PBA, MCA depicts the second algorithm used in iPlan®.

More detailed information considering dose calculation algorithms can be found in [6] and [7].

1.4.4 Linac

The medical linac has become the most wide-spread megavoltage radiation source in modern radiation therapy. It is designed compactly and offers an excellent opportunity to provide electrons, photons, protons or other ions with a wide range of energies. In this study, only photon radiation was used. High energy photons constitute the most commonly applied beams in radiation therapy. This is due to their great penetration compared to kilovoltage beams, which enables treatment of deep situated tumors. Besides this advantage, surface sites such as skin are barely damaged. In figure (1.10), depth dose curves are depicted, characterizing generic beam qualities.

Early megavoltage radiation therapy was carried out with the use of Cobalt-60 units. Compared to Cobalt-60 units, linacs provide more versatility in the choice of beam energy and have the ability to deliver a higher dose rate. With medical linacs photon energies of up to 25 MeV can be produced. Moreover, the source does not have to be replaced with time, as it is the case of Cobalt-60 units. Additionally, a collimator system located in the treatment head of modern linacs, provide the opportunity to individually shape irradiated fields. The treatment head can rotate along its rotation axis and can be set at all desired gantry angles. For more details, especially

concerning the general design and the basic components of a linac, [7] can be consulted.

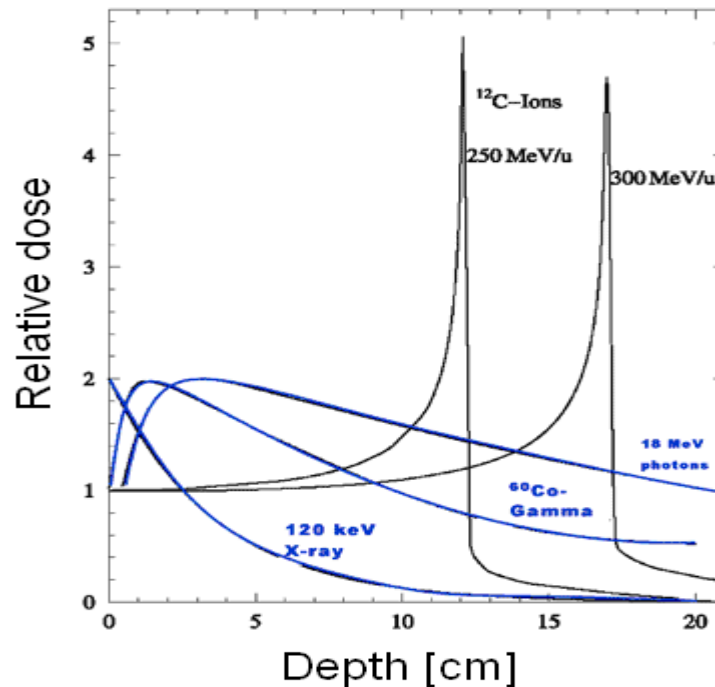


Figure (1.10): Generic depth dose curves representing X-rays, γ -rays as well as ion rays with various energies

1.4.5 Cone Beam Computed Tomography

Cone Beam Computed Tomography (CBCT) is an imaging modality recently integrated in the radiation therapy process. It makes it possible to acquire full 3 dimensional (3D) images of the patient on the treatment couch in treatment position. It consists of a kV X-ray source and an opposing flat panel imager. Both are mounted on a retractable arm onto the linac gantry at 90° to the treatment head for the acquisition of kV X-ray images for radiography, fluoroscopy and CBCT. The central axes of the kV imaging beam and the MV treatment beam should nominally cross at the isocenter. A CBCT scanner operates on the same principle as conventional CT, with the exception that an entire volumetric image is acquired during one single rotation of source and detector. This is possible by the use of a two dimensional detector instead of the one dimensional detector utilized in conventional CT [9]. With CBCT, a set of planar images is acquired by a cone shaped beam while the gantry of

the linac rotates around the treatment couch. A 3D volumetric image is then reconstructed from this series of planar projection images by the software of the imaging system with the use of a backprojection algorithm [11]. In figure (1.11) a), the principle of backprojection and detected intensity profiles are depicted and in b), the schematic geometric build-up of a CBCT system is shown.

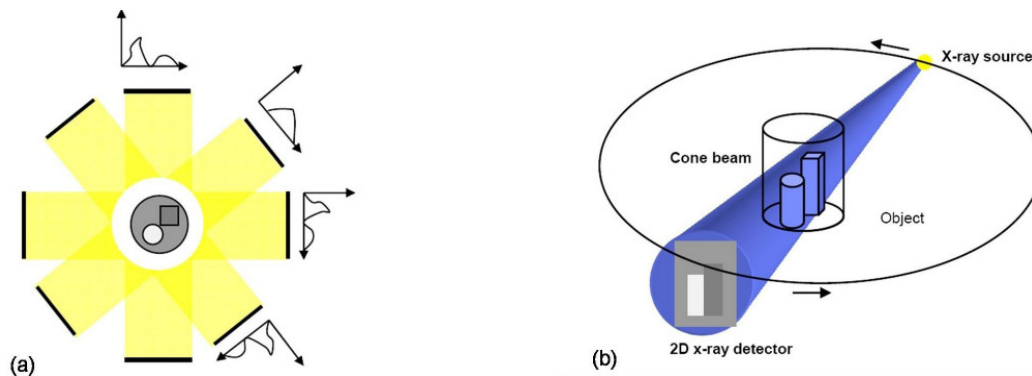


Figure 1.11: a) The principle of backprojection and b) build up of a CBCT system [10].

1.4.5.1 Artifacts in CBCT

In every diagnostic image it comes to a certain extent to characteristic imaging errors. Such influences can contribute unfavorably to the image quality. An artifact is a pattern on an image, which is not directly related to a geometrical object. Subsequently, it does not reflect anatomy or any other physical object, but it is instead generated by limitations of image acquisition [2].

Artifacts can arise from many causes. Some, which are primarily related to CBCT, are mentioned and described briefly below.

Ring artifacts

Ring artifacts are concentrically arranged circles in a CBCT image. They fake alternately more and less attenuating material.

Possible reasons of such image disturbance are detector malfunctions such as a defect of single detector elements. An example of a ring artifact is depicted in figure (1.12).

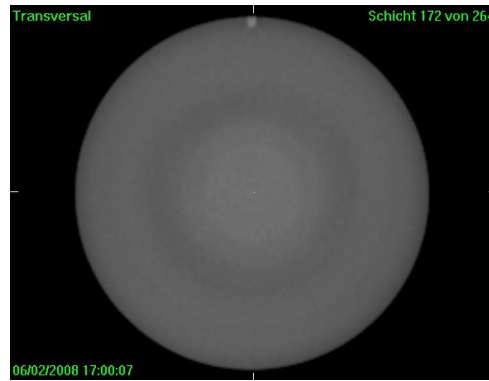


Figure (1.12): Ring artifact in the transverse view of the CATPhan® phantom
(section 2.5.2.3)

Streak artifacts

Streak artifacts appear as streaks or lines through the image. Most of them arise from the fact that the detector is susceptible to discontinuities of adjacent projection images from various sources.

Possible causes of such discontinuities are aliasing effects due to the limited number of acquired sample images and beam hardening effects due to shadowing phenomena because of high atomic number materials. An example of a streak artifact, arising in the multipurpose phantom (see section (2.5.4.2)) is shown in figure (5.11) in section (5.5.1).

Cupping artifacts

Cupping artifacts are deviations from a overall consistency of HUs across a homogeneous scan field. These make attenuation coefficients near the edges of scanned object to appear lower than close to the center. This happens, if X-rays pass through the center of an object and penetration increases with traversed distance due to beam hardening. Another reason for such artifacts may be scattered radiation.

Motion artifacts

Motion artifacts are caused by motion of the imaged object, which badly influence the sharpness of an imaging system. They manifest themselves as spreading of object boundaries and general blurring. While in CT it is possible to keep image acquisition time short and hence reduce patient's motion to a minimum, in CBCT it is not due to relative long acquisition times up to several minutes. These long acquisition times are

caused by a limitation of the gantry speed due to International Electrotechnical Commission (IEC) regulations. Involuntary motion, forced by location of the desired object close to lung or heart, can cause severe problems in image quality in CBCT.

2 Materials and Methods

2.1 Linac

All measurements in the framework of this diploma thesis were performed with the Elekta Synergy® linac (Elekta Oncology Systems Ltd, Crawley, UK), at the Department of Radiotherapy of the Medical University of Vienna (MUW)/AKH Vienna. This linac is a RT system, which is especially designed for IGRT. The system consists of a digital accelerator that is able to provide X-rays of maximal energies of 6, 10 and 18 MV and a high precision treatment couch. Additionally, various imaging modalities such as MV and kV imaging devices are included.

The MV imaging device (iViewGT™) is mounted opposite to the treatment head for the acquisition of planar MV images utilizing the treatment beam. By contrast, the kV imaging modality (XVI) is situated on a retractable robotic arm, displaced by 90° according to the therapy beam. The kV imaging tool comprises a kV X-ray tube with an opposing flat panel detector in order to acquire projection images for radiography, fluoroscopy and CBCT [12]. In figure (2.1), the entire Elekta Synergy® IGRT system is shown.

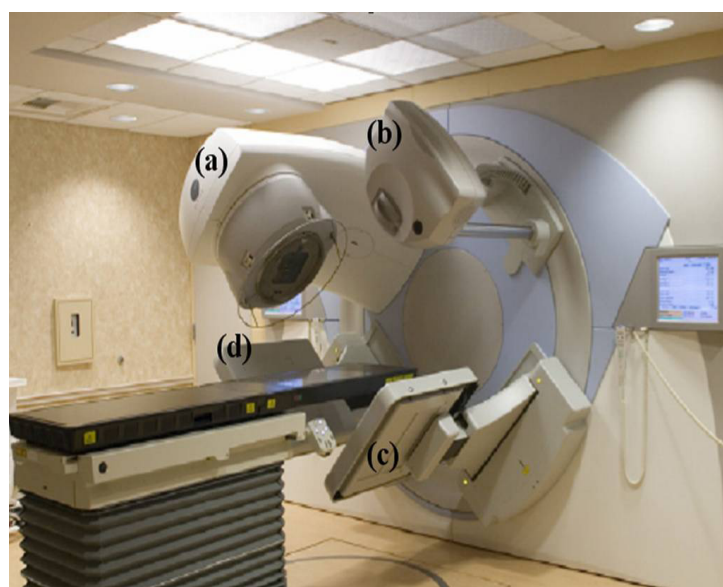


Figure 2.1: Elekta Synergy® System. a) Treatment head, b) kV X-ray tube, c) MV flat panel detector, d) kV flat panel detector

2.1.1 Flat panel detector

The detector that is applied for both, kV and MV imaging, is an amorphous silicon (a-Si) flat panel detector with a size of 410 mm x 410 mm, a pixel size of 0.4 mm and a maximum resolution matrix of 1024 x 1024 pixels. Basically, X-rays incident on the flat panel detector are scattered by a copper plate under the liberation of electrons. Subsequently, the generated Compton electrons are absorbed in a cesium iodide crystal, which serves as a scintillator in order to convert the electrons into visible light. Such produced light photons are then detected by the large photodiode array consisting of a-Si photodiodes. The major difference between the XVI- and the iViewGT™ panel is the elimination of the copper plate and the substitution of a gadolinium oxysulphide scintillator for the cesium iodide crystal [14].

2.1.2 KV Imaging

In the context of this project, 2 and 3 dimensional images are acquired by the use of the appropriate kV image acquisition modes, Planar View™ and Volume View™.

In Planar View™, the gantry of the linac remains still while acquiring an image. One image is made by recording a series of frames and averaging them to one single image. In the XVI software environment, various parameter collections are defined in so called ‘presets’, in order to guide different acquisition procedures. Such presets contain parameters in the manner of mAs and kV settings, collimator and filter prescriptions or information about reconstruction algorithms. For different anatomic regions there exist diverse protocols, such as head, pelvis and chest. In all of the three cases different kV and mAs settings are adopted. In the table below, these specifications are listed for each planar imaging protocol.

<u>Presets for planar imaging protocols</u>			
<i>Preset label</i>	<i>kV</i>	<i>mA/Frame</i>	<i>ms/Frame</i>
Head	100	10	10
Pelvis	120	32	40
Chest	120	25	40

Table 2.1: Predefined settings for image acquisition in 2D

In Volume View™, a set of planar images is acquired by a cone shaped beam, as outlined in the introduction. From these projection images, a full volumetric image is reconstructed by the system.

The resolution for the reconstruction can be chosen out of various defaults such as 0.5 mm, 1 mm and 2 mm voxels, respectively. One advantage of CBCT images acquired prior to daily treatment sessions it is to detect positioning uncertainties of the patient's setup. Furthermore, the XVI CBCT device allows selecting the width and the length of the X-ray field. The width refers to the so called Field of View (FOV). The FOV characterizes the irradiated coronal distance at the isocenter (target–bottom-direction) from the treatment couch. Consequently, it is directly related to the diameter of the region of the patient that is desired to be imaged. As parameters considering FOV, the user can choose either Small (S), Medium (M) or Large (L), respectively. The positions of the flat panel can be approached, as requested in the underlying imaging presets.

The length of the X-Ray field refers to the axial distance (Gun-target-direction) that is irradiated at the isocenter. This distance can be modified by manually inserting different collimator cassettes. In the following table, the various irradiated distances at the isocenter related to the appropriate collimators and FOV are listed.

<u>Irradiated distances at isocenter</u>			
<i>Collimator cassette label</i>	<i>Irradiated axial distance at the isocenter [mm]</i>	<i>FOV</i>	<i>Irradiated coronal distance at the isocenter [mm]</i>
20	276.7	S	138.4
10	135.42	M	213.2
20	276.7	M	213.2
10	143.23	L	262

Table 2.2: Irradiated geometrical field at the isocenter, as a function of collimator and FOV.

For the various protocols available in Volume View™, different settings regarding tube voltage, tube current, exposure time, and applied reconstruction algorithms are requested. Several examples are listed in the table below.

Parameter collections classifying CBCT protocols

<i>Preset label (Protocols)</i>	<i>FOV</i>	<i>kV</i>	<i>mAs</i>	<i>Reconstruction (voxel size) [mm]</i>
Image Quality	S	120	1040	0.5
Image Registration	S	120	16.5	0.5
Head and Neck (H&N)	S	100	36.1	1
Prostate	M	120	1038.4	1
Pelvis/Chest	M	120	649	1
Pelvis (BTF)	L	120	1664	1

Table 2.3: Acquisition parameters for particular CBCT protocols

Additionally, a Bow Tie Filter (BTF) is available for the protocols Prostate, Pelvis and Chest. A BTF is a filtering device, which can be inserted in front of the kV-X-ray source in order to reduce intensity fluctuations across the flat panel detector. As a consequence of alterations of intensity across the detector plane, several detector elements might go into saturation, which leads to image artifacts. The BTF is usually constructed of aluminum and oppositely shaped to the patient's curvature. In figure (2.2), a schematic drawing of the principle of a BTF is depicted.

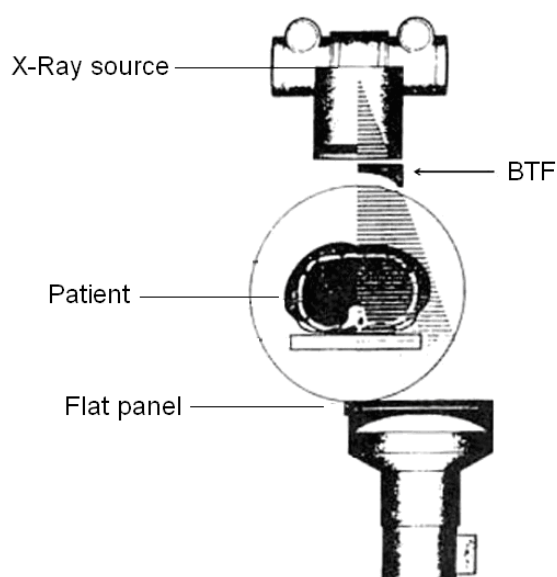


Figure 2.2: Schematic image of the BTF and its function

2.1.3 MV imaging

For MV imaging iViewGT™ is utilized. MV images are acquired by detecting the exit dose, delivered by the treatment beam, behind the patient. For this purpose, an Electronic Portal Imaging Device (EPID) is used. An EPID is a similar device to the kV flat panel imager of the XVI. The differences between them are described in section (2.1.1).

The restriction of MV imaging modalities is the loss of soft tissue contrast due to the domination of the Compton interaction, as visible in figure (1.6). In the context of the current study, iViewGT™ is not applied for imaging purposes.

2.2 Computed Tomography

All images of the phantoms, which are needed for dose comparisons in the further studies, were acquired with the Siemens Somatom Plus 4 Volume Zoom®, a four slice CT scanner.

The Volume Zoom® is capable of various default scanning protocols with different parameter settings, i.e. Chest, Pelvis and H&N. Slice width, field size, scan time and effective mAs can be set arbitrarily, while kV settings are fixed to 120 kV.

2.3 Treatment planning system

For dose calculations, which were performed in the framework of this diploma thesis, the Treatment Planning System (TPS) iPlan® of BrainLAB was used. This TPS offers a choice of many different contouring and modern planning techniques, such as stereotactic planning and IMRT. For illustration purposes, a screenshot representing the planning monitor of the TPS is shown in figure (2.3).

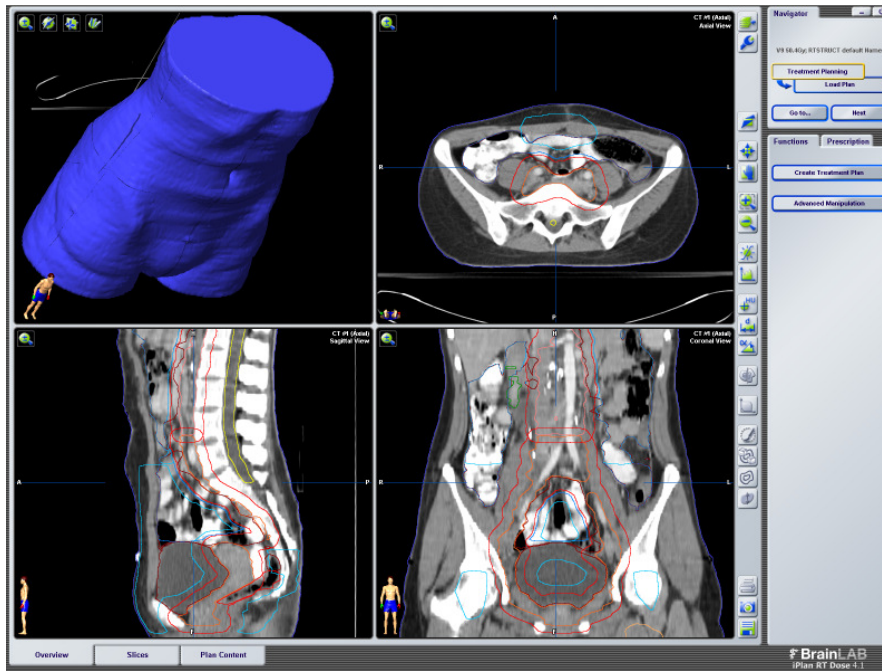


Figure 2.3: TPS iPlan® of BrainLAB

2.4 Dosimetric equipment

As dosimetric measurement devices for the acquisition of basic beam data sets (see chapter (4)), two types of detectors, i.e. diodes and ionization chambers were employed. For further information, see [16].

2.4.1 Diodes

A diode is a special device to detect the absorption of ionizing radiation. Ionizing photons are measured by means of the number of charge carriers set free in the active detector volume, which is located between two electrodes. While interacting with the consisting semiconducting matter, ionizing radiation produces free electrons and holes, whose number is proportional to their released energy. Consequently, a certain amount of electrons is lifted into the conduction band and the equal number of holes is created in the valence band. When an electric field is applied, electrons and holes travel to the appropriate electrodes to provoke an electric pulse which can be amplified and measured.

In our case, a diode with an active area of 2 mm diameter was used as field detector as well as reference detector between the treatment head and phantom. Diodes can be constructed very small, because compared to gas filled ionization chambers (see section (2.4.2)), because their density is very high. Hence, charged particles of high energies can give off their energy in a volume of relatively small dimension and thus spatial resolution of a diode is much better than for ionization chambers. Another advantage of diodes is their better energy resolution. This can be justified, because the energy requested for production of an electron-hole-pair is very low, compared to the energy requirement for production of paired ions in a gas filled detector. Consequently, the statistical variance of the pulse height is smaller and energy resolution increases. The response of diodes is energy dependent, which can cause problems, e.g. for Percentage Depth Dose (PDD) measurements (see section (4.3)). For such purposes especially modified diodes are utilized that compensate for energy dependencies.

The diodes can also be handled with an additional build up cup for air measurements in order to provide enough build up thickness and hence secondary particle equilibrium. In figure (2.4), the field diode and brass build up caps for several energies are illustrated.



Figure 2.4: Diode with diverse build up cups

2.4.2 Ionization chambers

An ionization chamber consists of a gas filled cavity between two conducting electrodes. When the gas between the electrodes is ionized, the produced ions and dissociated electrons move to the electrodes of the opposite polarity, thus creating

ionization current. This current can be amplified and measured. There are multiple designs of ionization chambers. For dose determination in water, the most common types are cylindrical chambers with air as counting gas. They consist of an active volume with a central collecting electrode, located in the axis of symmetry. Typically, the active volume of an ionization chamber in medical use ranges from 0.1 cm³ to 1 cm³ [15].

In our case, ionization chambers with an active volume of 0.13 cm³ were used for relative dose measurements in the water phantom, while a PTW 31003 ionization chamber (Farmer type chamber) with an active volume of 0.6 cm³ was used for absolute dosimetry. Again, brass build up cups for air measurements are available. All dosimetric equipment is provided by the company of Scanditronix Wellhöfer GmbH. In the figure below, one of the above mentioned chambers is displayed.



Figure 2.5: CC13 #6669 Ionization chamber

2.5 Phantoms

2.5.1 Dose measurement phantoms

2.5.1.1 Water phantom

Measurement of Basic Beam Data requires a full scatter water phantom. For such purposes, the 'Blue Phantom', provided by the company of Scanditronix Wellhöfer, is available at the department. Moreover, the OmniPro-Accept software can be utilized as measuring software that provides the user with the opportunity to visualize and analyze dosimetric entrance data. In figure (2.6), a screenshot of Omnipro-Accept can be seen. The Blue Phantom is depicted in the figure thereafter.

The Blue Phantom contains two detector holders, one for the field detector and the other for the reference detector, employed for relative dose measurements. The field detector is movable along all three rotation axes by the help of an electric engine, which allows the chamber or diode to be positioned with an accuracy of 0.5 mm. The holder of the reference detector is mounted statically onto the phantom walls during measurements.

For all the measurements the step by step mode was used for scanning the detector in the phantom.

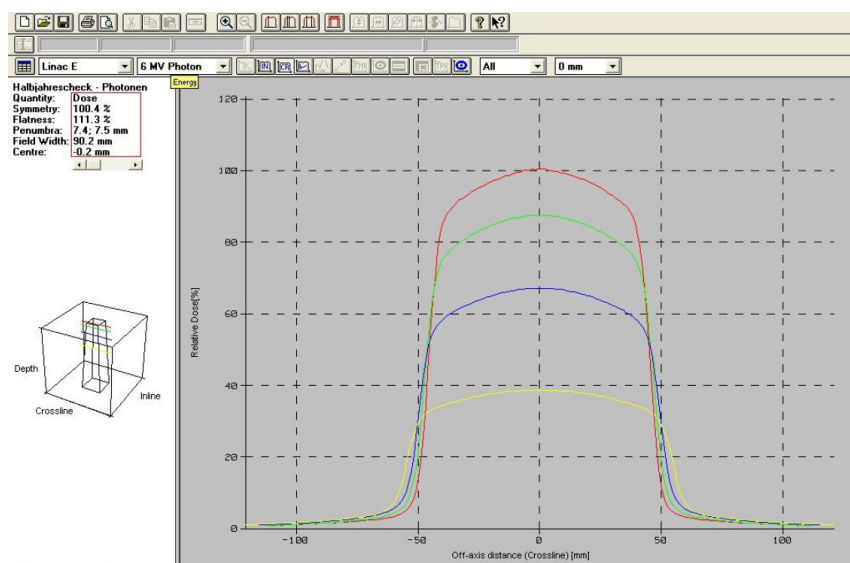


Figure 2.6: OmniPro-Accept software



Figure 2.7: Blue phantom

2.5.2 Image quality phantoms

For QA of the CBCT device various phantoms are required, which are given in the following.

2.5.2.1 TOR 18FG

The Tor 18 FG phantom (Leeds Test Objects, UK) is especially designed for QA purposes in two dimensions. It embodies a circular disk that comprises a resolution bar pattern test and a low contrast sensitivity test. On the basis of these tests, low contrast visibility and resolution of the planar X-ray system can be evaluated. The low contrast sensitivity test contains a series of disks with gradually decreasing contrast. Regarding resolution of the imaging system, there is a simple resolution indicator located in the center of the phantom. It consists of 21 separated groups of bar patterns, each distinguishable group representing certain resolution. The Tor 18 FG phantom is shown in figure (2.8).

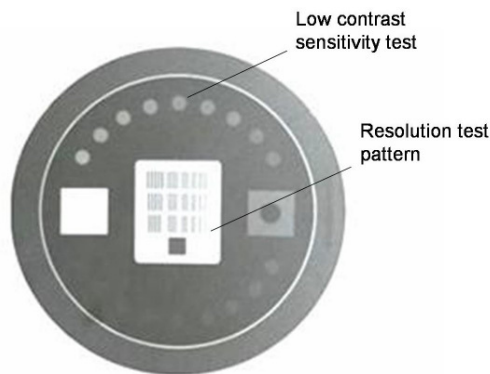


Figure 2.8: TOR 18 FG phantom

2.5.2.2 Cube phantom

The Cube phantom is an in-house developed phantom, exploited for verification of distance rendering in 2 dimensions. It consists of a 150 mm x 150 mm sized cube out of polystyrene with metal BBs on 5 sides, forming a trapeze.

The spots are localized on defined points, so that distances between them can be measured by the use of software tools. The Cube Phantom is illustrated in figure (2.9 (a)).

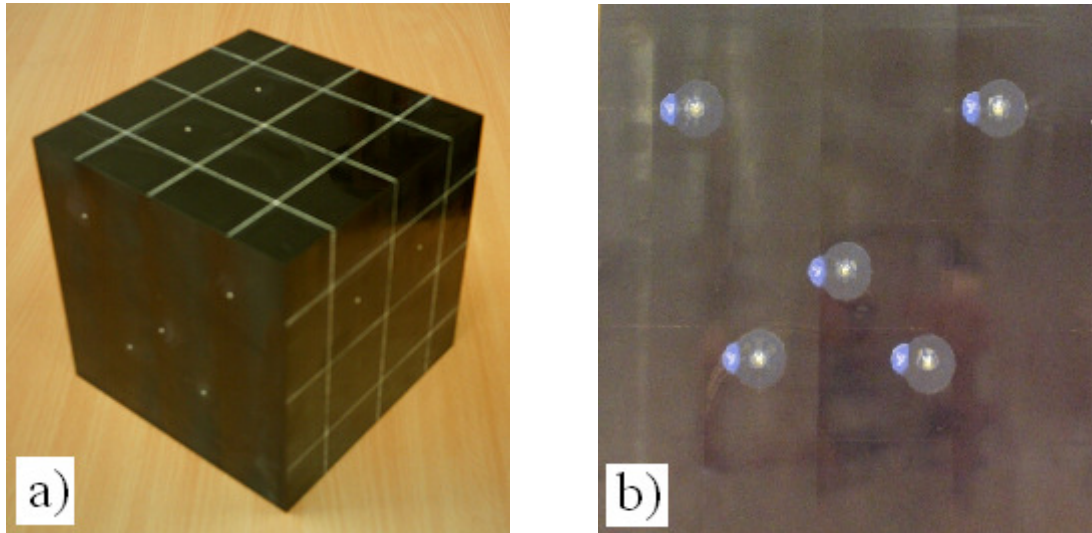


Figure 2.9: Cube phantom (a) and lateral view with BB trapeze (b)

2.5.2.3 CATPhan® phantom

The CATPhan® phantom (The Phantom Laboratory, Incorporated, NY) (figure 2.10) is especially designed for QA in three dimensions. It is a cylindrical phantom that contains various sections, each comprising different test opportunities. The modular design of the phantom enables the user to determine different image quality parameters by acquiring one single 3 dimensional image. In this study, three modules of the CATPhan® phantom were used for IQ evaluations. They are outlined in figure (2.11). In order to determine image uniformity, the especially therefore constructed image uniformity section is used. In this module, material's CT numbers are designed to represent water's density within 2%. Additionally, a tungsten wire is located in this module, which is used as a point source in order to evaluate the Modulation Transfer Function (MTF). Low Contrast Visibility (LCV) can be evaluated by scrolling into the Low Contrast (LC) module, containing LC targets. These targets consist of 7 tissue substitute materials, which highly differ in density from each other. The inserts, listed by increasing density, are: Air, PMP, Low Density Polyethylene (LDPE), Polystyrene, Acrylic, Delrin and Teflon. In order to optically determine the 3D resolution limit of the

XVI system, there is the high resolution module. This module contains a closing ranks line pair pattern, based on which resolution may be evaluated.

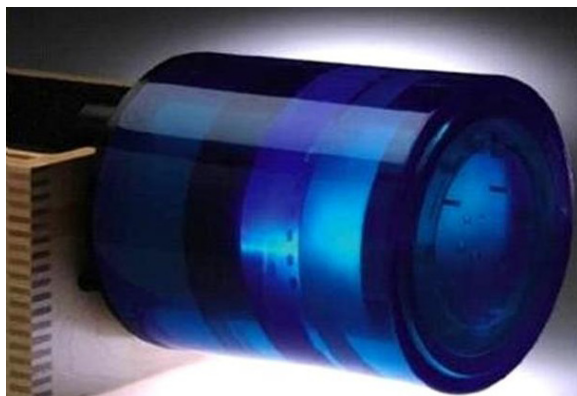


Figure 2.10: CATPhan® phantom

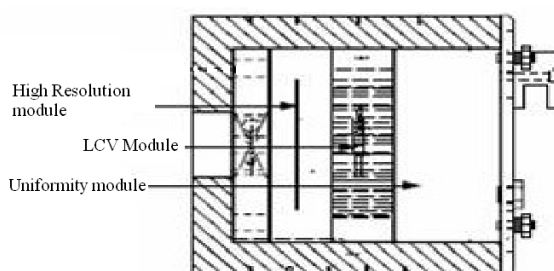


Figure 2.11: Modular design of the CATPhan® phantom

2.5.2.4 Single ball bearing phantom

The single ball bearing phantom (figure (2.12)) is designed for QA of image registration as well as table movement accuracy. It consists of a small steel ball, located exactly at the end of a long plastic tube, which is screwed onto the treatment couch. A set of vernier adjustment screws serves as connection part between table and tube. This vernier assembly allows the position of the ball to be adjusted in steps of 0.01 millimeters

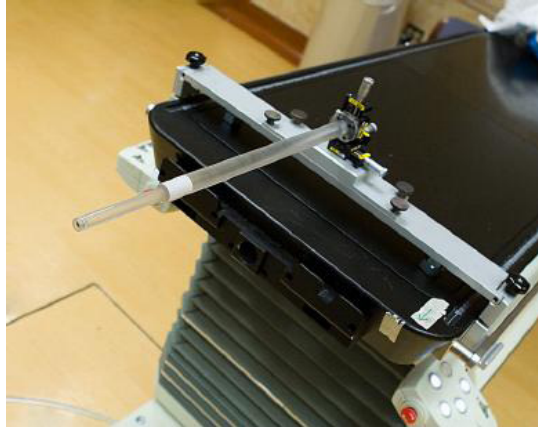


Figure 2.12: Single ball bearing phantom

2.5.3 Electron density calibration phantoms

For the establishment of the required relationship between Hounsfield Units (HU) and Electron Density (ED) (see chapter 5), calibration phantoms are needed in order to perform dose calculation.

The CATPhan® phantom (figure 2.10) was brought up as one of them.

2.5.3.1 Gammex RMI® phantom



Figure 2.13: Gammex RMI® phantom

The Gammex RMI® phantom is a narrow slice phantom, which is especially designed for ED calibration purposes of CT. The phantom includes several tissue equivalent inserts that are embedded in a plastic matrix. The insert materials are

among others: brain-, lung-, liver-, breast-, and adipose-tissue as well as various bone and water equivalent inserts.

For further explanations about the above invoked phantoms, the respective manuals [17], [18] and [19] can be consulted.

2.5.4 Dose calculation phantoms

2.5.4.1 Pelvis phantom

An in-house constructed, 'pelvis-shaped' phantom is dedicated to the task of evaluating possible dose differences, which may be provoked by applying different HU/ED calibration curves. It consists of several trapezoid polystyrene slabs, which are screwed together with two long treaded rods. In figure (2.14) the pelvis phantom is depicted.

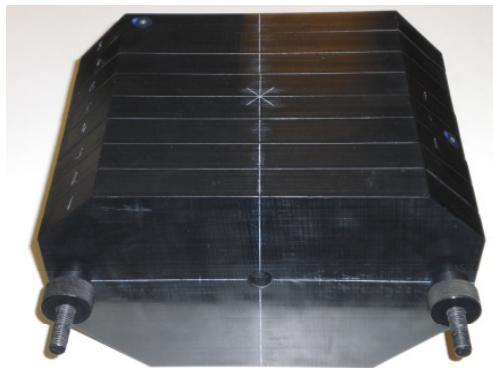


Figure 2.14: Pelvis phantom

2.5.4.2 'Multipurpose phantom'

An inhomogeneous slab phantom is used in order to perform dose calculations on. It was introduced predominantly to compare depth dose curves and dose profiles obtained from CT- and CBCT-based dose planning, but also composite plans, if needed.

The slab phantom (figure (2.15)) is build up alternately of polystyrene and cork slabs. Polystyrene is more or less water equivalent and cork simulates lung tissue well. In the second polystyrene section, an air and a wood insert are located, respectively.



Figure 2.15: Multipurpose phantom

3 Quality Assurance of CBCT

3.1 General aspects

IGRT with CBCT was adopted by many radiotherapy centers and became a key component in research in radiation therapy. CBCT images, acquired prior to treatment fractions, provide the option to detect positioning uncertainties and consequently patient setup can be adapted to the initial planning position. It can be expected that the accuracy and consequently the effectiveness of RT is therefore increased. There are various parameters in CBCT technology, such as the long detector to source distance, which are not optimal. Thus, a successful implementation of CBCT into RT requires a rigorous Quality Assurance (QA) program. Due to the lack of suggested and generally accepted procedures, the here performed QA program is based on the '*Customer Acceptance Test*' (by Elekta Synergy) [20] and IEC 61223-3-5 [21]. Some of the collected data are based on a study of Mag. Marlies Pasler, who implemented a similar QA procedure in 2007/2008 [2]. A well-thought-out QA refers to a safe, accurate and reliable operation of hardware as well as software. It addresses all the components of the system, which influence Image Quality (IQ) and positioning accuracy in two as well as in three dimensions.

3.2 Customer Acceptance Test

According to the IEC standard, *'the aim of an acceptance test is to demonstrate that the specified characteristics of the equipment lie within the specified tolerances as stated in accompanying documents. The accompanying documents shall include performance specification as stated by the manufacturer or as specified in the accompanying documents, including conditions of operations during acceptance testing as well as results from tests performed at the manufacturer's site or during installation, covering items of importance to quality. Furthermore, guidance as to the*

extent and frequency of maintenance procedures and reports on previous tests shall be provided' [21].

In the Customer Acceptance Test (CAT) of the Elekta Synergy® image guiding system XVI, various categories of checks of image quality, geometry as well as registration accuracy and table movement are mentioned. All tests and checks were performed on a monthly basis over a time span lasting from October 2008 to April 2009. The procedures were carried out by following precisely the instructions of the CAT.

3.2.1 QA in 2 dimensions

3.2.1.1 2D Low contrast visibility

In order to evaluate the 2D Low Contrast Visibility (LCV), the TOR 18 FG phantom was placed on the table top of the treatment couch and was aligned in the isocenter according to the laser system. Additionally, a copper plate was placed onto the phantom to avoid excessive scatter radiation and hence artifacts. Furthermore, the gantry of the linac was rotated to -90° and one X-ray image was acquired using the '*panel alignment – small FOV*' preset. In the actual image, LCV could be determined by setting contrast and brightness as stated in the CAT. The disks, which are still visible, were counted and the more disks were visible, the better the LCV. The CAT specifies that at least 12 visible disks out of 18 must be visible, which means that a LCV of smaller than 3 % is achieved. The general result of the 10 month lasting investigation was found to be located almost at the threshold of the specification limit. Between 13 and 14 disks could be determined. This corresponds to 2.3 % – 2.8 % LCV. No time trend could be observed.

3.2.1.2 2D Spatial resolution

Using the same X-ray image, acquired for the former test, 2D spatial resolution could be evaluated by observing the resolution grid (figure (3.1)) and counting the number of spatial frequency groups that can be resolved.



Figure 3.1: Resolution grid of TOR 18 FG

The purpose of this trial was to check, whether the CAT specification of at least 10 distinguishable frequency groups is met.

The results resulted in 12 - 13 groups, which corresponds to a resolution of 1.8 - 2 Line Pairs (lp) per millimeter and was located below from the CAT limit.

3.2.1.3 2D geometric accuracy

In order to evaluate 2-D geometric accuracy, 4 planar images of the ball bearing phantom, set at the MV isocenter, were acquired. Thereby, the kV X-ray source was positioned at the 4 cardinal gantry angles 0°, 90°, 180° and 270°, respectively. The coordinates of the steel ball centers in these images should match the coordinates of the image centers within 4 pixels (1.04 mm). The purpose of this test was to check, whether the display center of the acquired static image identifies the MV isocenter.

The deviation between the center of the ball bearing phantom and the coordinates of the image center never exceeded ± 2 pixels.

This result shows the high accuracy of the whole system, since the test was done right after the 3D registration accuracy test (see section 3.2.2.6), which correlates kV and MV isocenter.

3.2.1.4 Off isocenter distance distortion

The XVI system is calibrated that way that objects, which are located in the isocenter, are imaged to scale. The purpose of this test was to check how dimensions of

structures, placed apart from the isocenter, are transferred by the planar imaging system. It was expected that off isocenter distances are transferred according to the intercept theorem. For this check, images of the Cube Phantom (figure 2.9) were acquired at the four cardinal angles. On 5 sides of the phantom, metal markers are attached in a trapezoid manner (figure (2.9(b))). Concerning this test, the short as well as the long side of this geometrical shape, which have an offset of 75 mm from the isocenter, were determined. The long distance was known to be 90 mm and the short one was 50 mm, respectively. It was expected that the measured distances increase, when the markers lie nearer to the X-ray source. If the trapeze is closer to the detector, the reverse result should be detected. Distances were evaluated every third day over the period of almost two month. In the following table the results are depicted.

Off isocenter distance distortion

Source position	Short distance [mm]	σ_S [mm]	Long distance [mm]	σ_L [mm]
0°	54	0.1	97.1	0.2
90°	54	0.2	96.9	0.1
180°	46.1	0.1	82.6	0.1
270°	53.4	0.2	97	0.1

Table 3.1: Transferred off isocenter distances

Due to limited inherent accuracy of the XVI system, e.g. due to limited pixel size and blurring of the metal markers in the X-ray images, the test could not detect any distortions, which were not predicted by the intercept theorems. Possible gravitational flexes concerning X-Ray source and flat panel detector are therefore negligible. If there were deviations present, they were intended to be very small.

3.2.2 QA in 3 dimensions

All trials according to 3 dimensional IQ could be performed by exploring one single volumetric CBCT image of the CATPhan® phantom. For this purpose, the CATPhan® Phantom was placed onto the carbon treatment table and aligned according to the CAT instructions. Thereafter, the *CAT – Image Quality* preset was chosen in the VolumeView™ imaging mode, radiation was switched on and the gantry performed a full rotation. A volumetric image was then reconstructed from the acquired planar images. Based on this 3D volumetric image of the CATPhan® phantom, all the following tests were performed.

3.2.2.1 Low contrast visibility

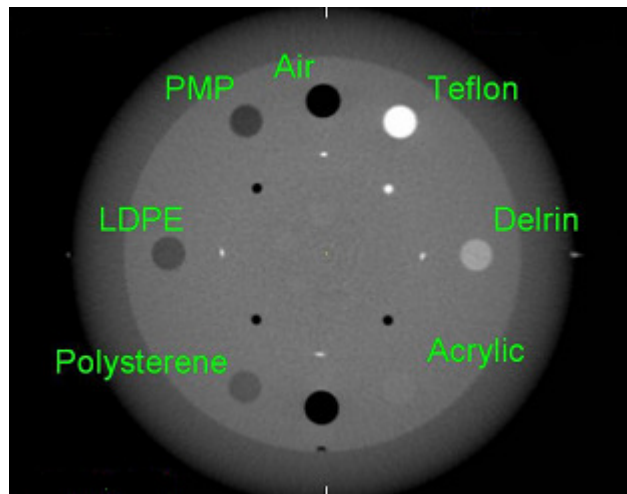


Figure 3.2: LCV module in the CATPhan® phantom

In order to evaluate 3D Low Contrast Visibility (LCV), the mean pixel values together with their standard deviation of two different inserts (polystyrene and LDPE) were investigated in the XVI software. These low contrast inserts are located in the LCV module of the CATPhan® phantom, as explained before. An image of this module is depicted in figure (3.2). LCV was calculated by the use of the following formula.

$$LCV = 2.7 \cdot \frac{(\sigma_{Poly} + \sigma_{LDPE})}{(\bar{x}_{Poly} - \bar{x}_{LDPE})} \% \quad (3.1)$$

Where \bar{x}_{Poly} and \bar{x}_{LDPE} refer to the mean CT value in the polystyrene and LDPE insert, respectively. σ_{Poly} and σ_{LDPE} are the corresponding standard deviations.

The purpose of this test was to demonstrate that the LCV meets the required specification of lower than 2 %.

In the following chart (figure (3.3)), the results are plotted. One can see that the required CAT specification was fulfilled every month.

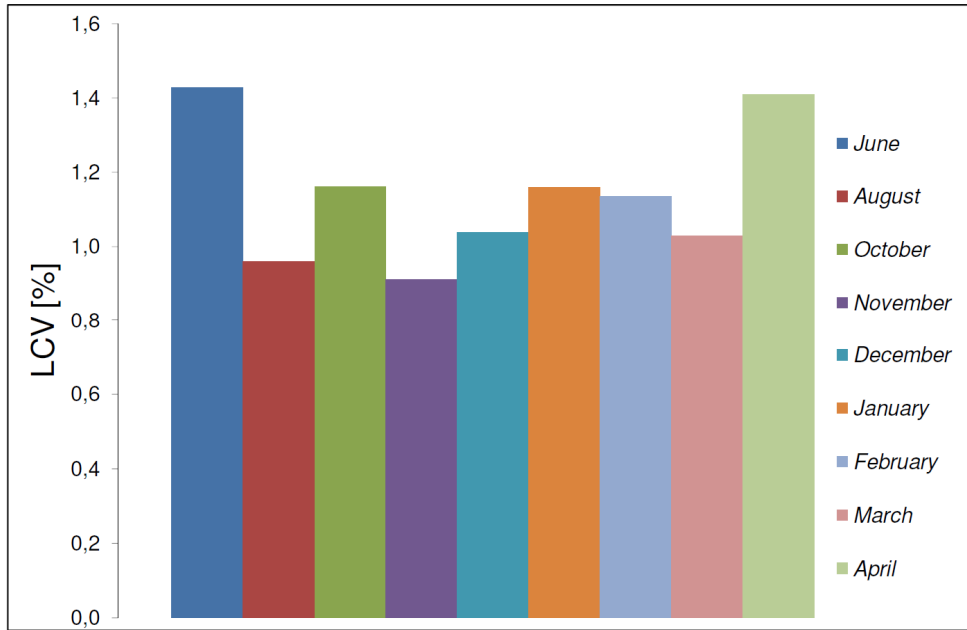


Figure 3.3: Results of the LCV evaluation

3.2.2.2 Image scale

The purpose of this test was to check how the CBCT system transfers distances between objects. This parameter should be assessed periodically, because it impacts the reconstructed image and the accuracy of recommended table shifts. As possible causes of discrepancies, drifts in the encoder, which indicate the distance and angles of mobile components of the XVI system and service manipulations can be mentioned [1]. In order to quantitatively evaluate disagreements of transferred distances, one can compare known distances in the CATPhan® phantom to distances obtained by the measurement tool in the XVI software environment. The CAT specification of this trial was such that distances in the CBCT image should agree within 4 pixels (1.04 mm) with the physical distances.

As test distances in the transversal view, the distances between the two air inserts and the LDPE and Delrin insert in the LCV module of the CATPhan® phantom could be used. On the other hand, the distance between the first and the forth alignment markers served as reference distance for the image scale verification test in the sagittal view.

The distance between the two air inserts as well as between the LDPE and Delrin inserts was known to be 117 mm. As vertical distance, a mean value of 117.1 ± 0.2 mm was found and for horizontal scale verification, results showed 117.0 ± 0.2 mm, respectively. None of the monthly samples exceeded the CAT specifications. Consequently, the specification of the CAT could confidently be reduced to lower than 0.5 mm. In case of the sagittal distance, the average scale value and its standard deviation were 110.4 ± 0.3 mm, while the real distance was known to be 110 mm. It has to be stated that this test strongly depended on IQ in terms of sharpness of the imaging system. The peripheral region of the inserts was not characterized by a well defined edge but was smeared out. Therefore, it was not well identifiable.

3.2.2.3 Spatial resolution

Using the high resolution module of the CATPhan® phantom (figure (3.4)), spatial resolution can be evaluated. This is done by determining the highest number of line pairs that was still distinguishable in the transverse view of the reconstructed volumetric image. The purpose of this check is to demonstrate that the 3D spatial resolution meets the required specification of at least 7 line pairs visible per centimeter.

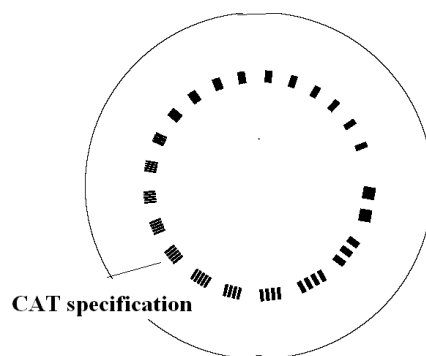


Figure 3.4: High resolution module in the CATPhan® phantom

The mean number of frequency groups, definable in the CBCT images, was 6.6 ± 0.7 lp/cm. It is obvious that the specification stated by the CAT was not met in this case. In figure (3.5), the bar chart for the monthly evaluations is shown.

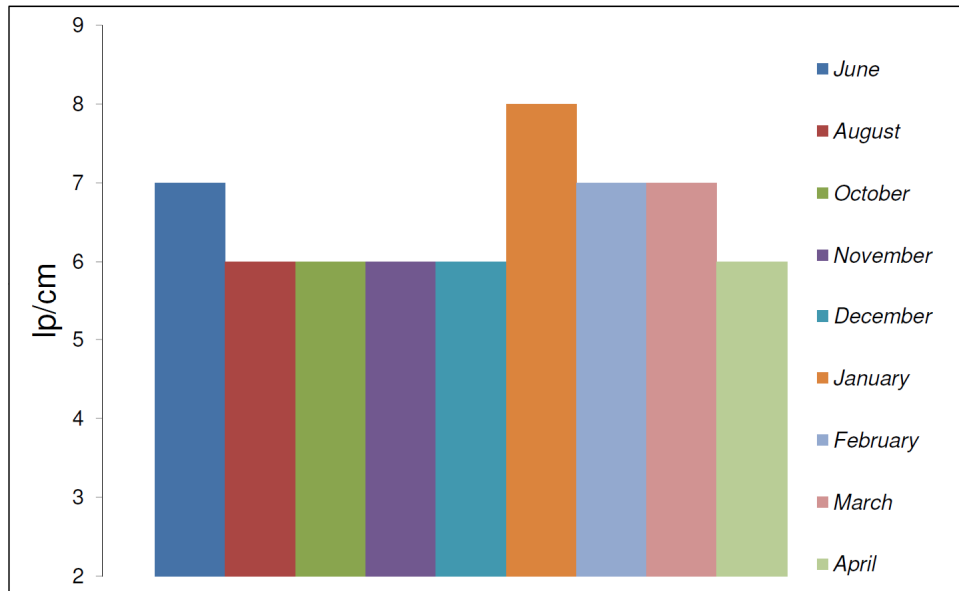


Figure 3.5: Results of the spatial resolution evaluation

It is clearly visible that the CAT specification was not fulfilled in the first few months. Spatial resolution suddenly increased, when a gain calibration was performed in January. In the course of 3 month after correction, the resolution limit returned to its former, worse value. However, it has to be stated that the test of determining spatial resolution optically was extremely observer and windowing level dependent. In order to bypass such dependencies and make a more objective determination, the Modulation Transfer Function (MTF) was used to specify spatial resolution.

3.2.2.4 Modulation Transfer Function

Another way to describe spatial resolution of an imaging system is the Modulation Transfer Function (MTF). The method of determining the resolution limit by use of the MTF is a very adequate method, because it is much less observer dependent. The MTF describes the ability of an optical system to gain an image, which varies in optical density and brightness in exactly the same way as the imaged object does.

A more intuitive explanation of this is how an imaging system transfers spatial frequencies that the imaged object consists of. Mathematically, the MTF is obtained by calculating a Fourier Transformation of a so called Point Spread Function (PSF). The PSF describes the response of an imaging system to a point object. As a consequence of blurring and bending effects, the ideally pillbox shaped PSF can be considered to have a Gaussian shaped form. The point object, which can be used to receive the PSF and consequently the MTF, was represented by the tungsten wire, located in the uniformity module of the CATPhan® phantom. Its diameter was known to be 0.28 mm. Due to the small extend of the wire and the corresponding pixel size, it could confidently be considered as a point source. Consequently, a Matlab script was used in order to determine the PSF of the tungsten wire and perform the requested Fourier transform. In figure (3.6), the workflow of determining the MTF of an imaging system is depicted. Three instances of optional outcome regarding obtained PSF and appropriate MTF are pictured. In the image, P refers to a pillbox answer, E to an exponential and G to a Gaussian response, respectively. Normally, MTF is normalized to 1 at 0 spatial frequencies.

In the course of image QA, the values of the MTF were reported at 50% and at 10% signal modulation for the CBCT scanner. The place, where the MTF of an optical system reaches 10% of the entrance contrast can be considered as the resolution limit of the system.

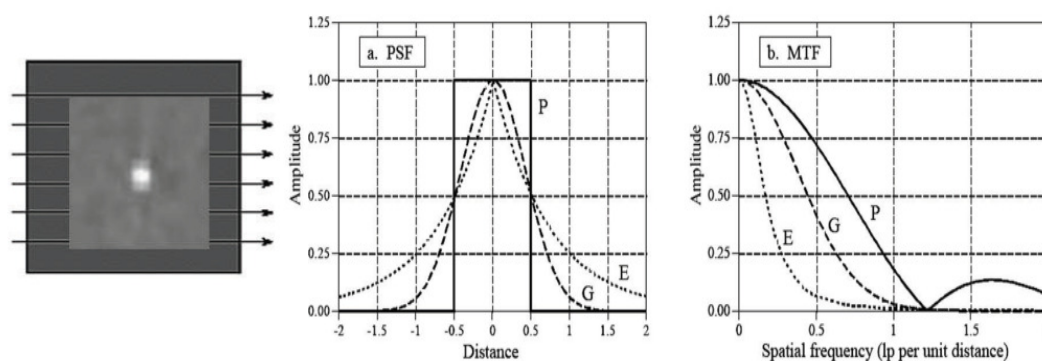


Figure 3.6: Examples of PSF and MTF

In the following charts, the resulting MTFs are visualized. In figure (3.7), all MTFs are plotted, determined over the 10 month period of investigation. It can be seen that there are doubtless discrepancies between each month. The behavior of the MTF

improved reasonably in January. As a reason, the gain calibration can be named. After the three following months, the MTF returned to its former, worse course.

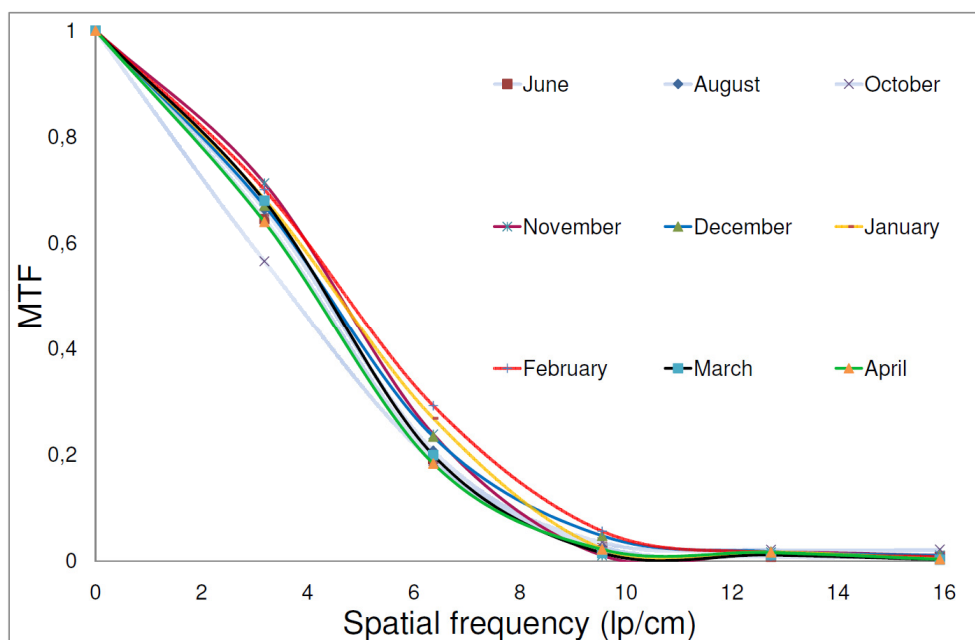


Figure 3.7: Results of the evaluation of the MTF

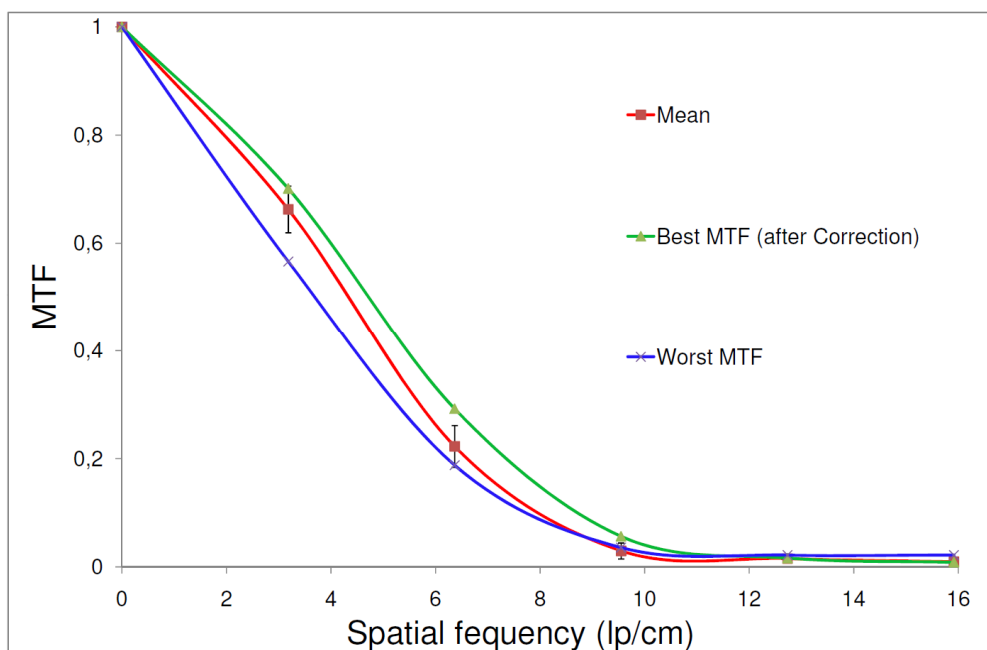


Figure 3.8: Mean, best and worst MTF

In figure (3.8), the mean behaviour, fringed by best and worst results of the MTF, is illustrated. Worst MTF was obtained in October, while best was detected in January, immediately after the previously mentioned calibration.

For the average MTF, a f_{50} value of 4.15 ± 0.15 lp/cm and a f_{10} value 8 lp/cm was detected, respectively. In the case of the worst MTF, 3.9 and 7.9 lp/cm and in best case 4.4 and 8.3 lp/cm were discovered for f_{50} and f_{10} , respectively. Due to relatively obvious discrepancies between worst and best MTFs, a frequent gain calibration, at least quarterly, is advisable by all means.

3.2.2.5 Uniformity

Uniformity is the consistency of Hounsfield Units (HU) (see section 5.2) in a CBCT image of a homogeneous phantom. Several types of artifacts provoke a heterogeneous distribution of HU values across the scan field. In order to evaluate the uniformity, so called regions of interest (ROI) were marked within the image of the uniformity module in the transversal view. One ROI was located in the center of the image. Other three ROIs were placed at angles of 0° , 120° and 270° surrounding the center. One had to take care that the ROIs were not placed in the outlying regions of the image, because there inconsistency of HUs was not avoidable due to beam hardening effects. Consequently, just the inner area of the acquired image underwent evaluation. By the use of the XVI software, average HU values could be measured within the ROIs and hence image uniformity was evaluated by the use of the following formula.

$$MPD = \frac{(\bar{x}_{\max} - \bar{x}_{\min})}{\bar{x}_{\min}} \cdot 100\% \quad (3.2)$$

Here, MPD names the Maximum Percentage Difference in HU values and \bar{x}_{\max} and \bar{x}_{\min} refer to their maximal and the minimal mean number, respectively.

The purpose of this test was to demonstrate that uniformity meets the CAT specification for the MPD of lower than 2%. In the following chart the results are depicted.

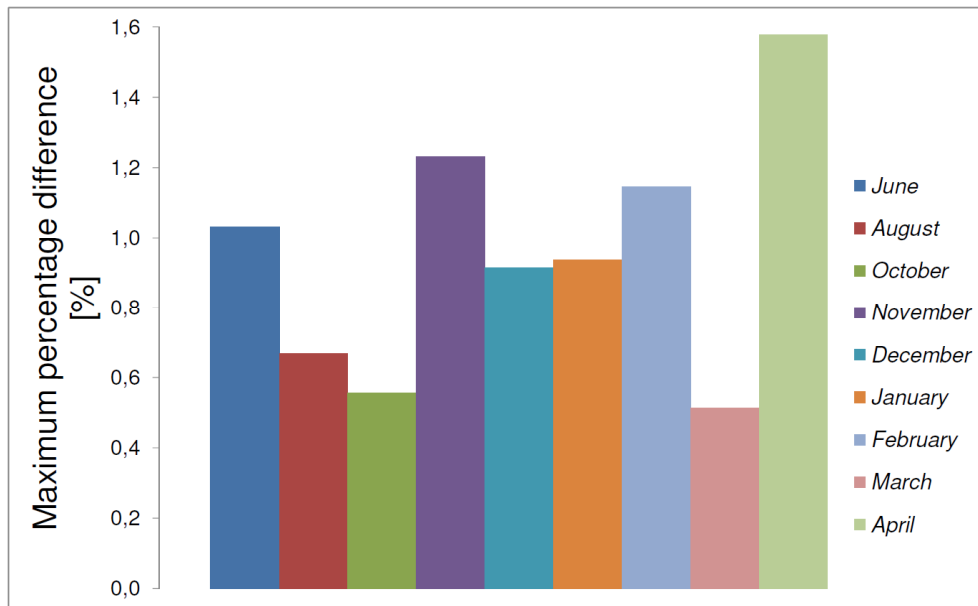


Figure 3.9: Results of the uniformity evaluation

One can see that the specification of the CAT was always fulfilled.

3.2.2.6 3D registration and geometric accuracy tests

The purpose of the 3D registration accuracy test was to check the accuracy of the matching of kV and MV isocenter. This test is crucial due to the need of reliability on coincidence of planned and delivered isocenter. In figure (3.10), a schematic explanation of the matching process regarding kV and MV isocenter is shown. The specification given by Elekta was 1 mm. All of the following tests were done by scanning the single ball bearing phantom by the use of the '*CAT-Image registration*' preset. The initial setup of the ball bearing phantom was done by using the in-room laser system, according to which the steel ball was aligned. In the reconstructed image, a reference image, provided by the manufacturer, appeared automatically. The scan could be moved manually so that it matched the reference plane in all three dimensions. The amount of displacement was calculated automatically and had to be corrected manually by using the vernier screws on the ball bearing holder. After correction, another scan was acquired, where the offset must not exceed 1 mm in any direction in order to determine kV isocenter. For comparison purposes, eight MV images were taken at the four cardinal gantry angles and at collimator settings of 0° and 180°. Based on analysis of the acquired kV and MV images, the deviation of

the position of the ball from the location of the MV beam isocenter was calculated for x, y, and z. Flexmap tables, which compensate for gravitation induced flexes of flat panels, were also taken into account by the XVI software. The difference between MV and kV isocenter in all three directions should be below 0.5 mm. In figure (3.11), the finally obtained difference between kV and MV isocenter are depicted. They were in good agreement with the specifications of the CAT.

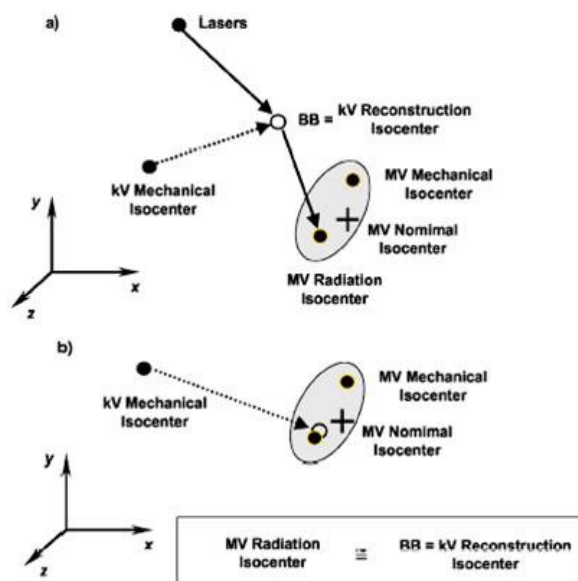


Figure 3.10: Schematic illustration of the kV to MV isocenter matching process [2]

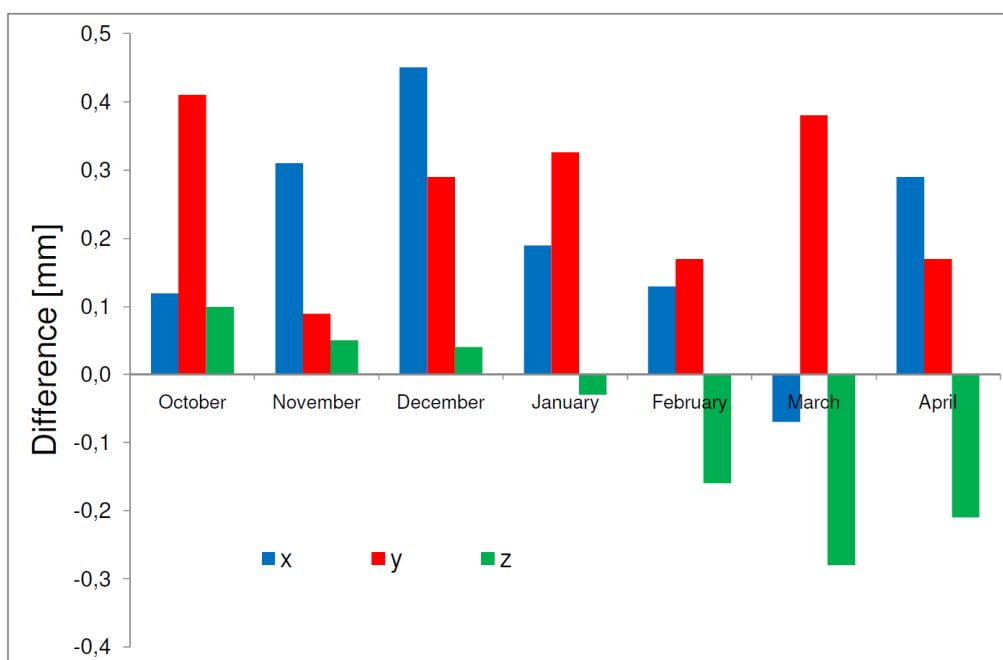


Figure 3.11: Deviations of the kV- to the MV isocenter.

3.2.3 Table movement assistant accuracy

The purpose of this test was to monitor the accuracy of the table move assistant. Using the single ball bearing phantom, which was positioned at the isocenter, the couch was shifted manually by 15 mm in each direction. With the preset '*CAT - Image Registration*', a volumetric image was acquired and in the registration window the steel ball was shifted manually, so that it matched the reference image in all three planes. The manual shift was converted to corrections, so that the table could be moved automatically by the calculated distances. Again, a volume scan was acquired and in the registration window the matching of the images should be confirmed. Deviations of the positions of the steel ball within the two volumetric images in submillimeter range could be determined by the software. The CAT stated that the offset of the table had to be smaller than 1 mm in any direction. In figure (3.12), the obtained results of the table movement accuracy tests are depicted.

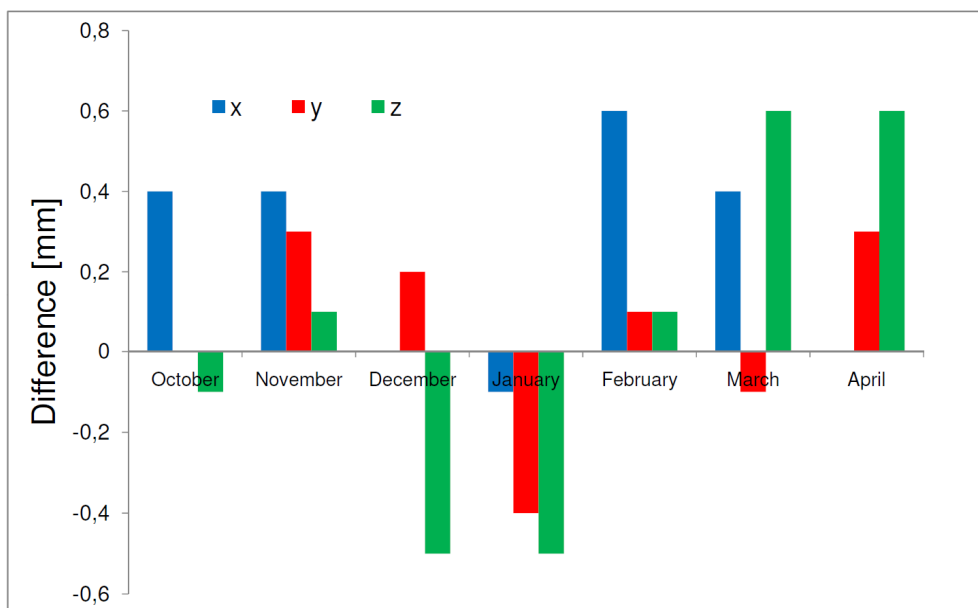


Figure 3.12: Results of the table movement accuracy test

Table movement was found to be very accurate until April and the CAT specifications were met in all samples. In April, the treatment table was exchanged due to operation problems. Afterwards, although still in tolerance, the highest deviations of the table were measured. An average offset value of 0.24 ± 0.27 mm, 0.06 ± 0.25 mm and 0.04 ± 0.45 mm for x, y and z direction was detected, respectively. The precision of

the table movement assistant is absolutely important, since final patient's positioning errors, detected by CBCT, are corrected using the automated assistant. When taking into account the mechanical precision of the table movement assistant, pixel size of the XVI system and inherent inaccuracies of the measurement software, the results of the tests were within the experimental uncertainty of 1 mm.

4 Basic Beam Data

4.1 Introduction

For tuning of a treatment planning system, a certain set of basic beam data is required. The amount of required beam data depends on the treatment planning system and the applied dose calculation algorithm. The basic beam data described in the following, namely nominal linac output, percentage depth dose curves, dose profiles and scatter factors, were specific for the treatment planning system iPlan® of BrainLAB. With the acquisition and implementation of the beam data into iPlan®, treatment planning for the Elekta Synergy® treatment unit with the Elekta Beam Modulator™ is enabled. Basic beam data were collected for the pencil beam (PBA) dose calculation algorithm as well as for the Monte Carlo algorithm (MCA).

The accuracy of the dose algorithm is directly related to the accuracy and the range of the beam data measurements. It has to be assured that measurements cover the range of field sizes and depths that will be used in later treatment planning and delivering.

It is not possible to measure dose distributions directly in patients. Therefore, irradiation of clinical cases is simulated by verification phantoms. All beam data were collected by recording dose distributions and scatter factors in the full scatter water phantom (Wellhöfer Blue Phantom), described in section (2.5.1.1)

4.2 Nominal linac output

For dose calculating purposes, the TPS needs to gain information about the dose, which the linac delivers to a certain point in a patient or a phantom. An ionization chamber, located in the treatment head, produces a reading proportional to this dose. It is dependent on various beam parameters and therefore, the monitor chamber must be calibrated. A calibration is usually performed such, that one Monitor Unit (MU) corresponds to one cGy at a specified point in the phantom, delivered by a

beam traversing a specified Field Size (FS). In our case, the linac was tuned in such a way that one MU corresponds to 1 cGy in 100 mm depth in a water phantom with a Source to Surface Distance (SSD) of 900 mm. Measurements had to be done, in order to verify this absolute beam calibration. Additionally, measurements of the nominal linac output in 100 mm depth with a SSD of 1000 mm were required for the MCA. The normalization field size was 104 mm x 96 mm in both cases. For this measurement, a Farmer type ionization chamber, connected to an UNIDOS electrometer, was used to display the produced amount of charge carriers in its active volume. After compensating for influences like air pressure, temperature, chamber parameters and beam quality, results were converted to Gray using the IAEA TRS 398 protocol [31]. With the knowledge of the delivered MUs, one can verify the output of the linac to be adequate. The results of the verification measurements are shown in the following table.

<u>Nominal linac output [cGy/MU]</u>			
<i>Energy [MV]</i>	6	10	18
<i>SSD 900 mm</i>	0.994	0.99	0.99
<i>d = 100 mm (PBA and MCA)</i>			
<i>Deviation from expected value of 1 cGy/MU [%]</i>	-0.6	-0.99	0.99
<i>SSD 1000 mm</i>	0.828	0.821	0.827
<i>d = 100 mm (MCA)</i>			

Table 4.1: Results of the nominal linac output measurements

4.3 Percentage depth dose

4.3.1 Definition of the required data sets

Absorbed dose in a phantom and finally in the treated patient varies with depth. For dose prediction in a certain point within the patient, a TPS has to account for such dose variations. They are dependent on various conditions such as beam energy, depth, field size and SSD. In order to establish a relationship between dose and depth, the water phantom was dosimetrically scanned along its central axis by the use of a diode. One method to characterize the dose distribution along the central axis is to calculate the Percentage Depth Dose (PDD). PDD is the dose, obtained from dose measurements, normalized at a certain reference depth. Mathematically it is expressed as follows.

$$PDD = \frac{D(d)}{D(d_0)} \cdot 100\% \quad (4.1)$$

In this formula, $D(d)$ represents the dose, obtained in a certain depth d and $D(d_0)$ refers to the dose in a reference depth, which is in high photon case mostly the depth d_{\max} , where maximum dose occurs.

4.3.2 Results

The iPlan® TPS required depth dose curves for all beam qualities available, i.e. energies of 6 MV, 10 MV and 18 MV and several FSs. The PDDs of the FSs, which are listed in table (4.2), were requested for both, as well as MCA. While for the PBA, PDDs were required just for water, PDDs for the MCA had to be measured in water as well as in air. For measurements, again diodes of Wellhöfer Scanditronix (see section 2.4.1) were used. In case of air PDDs, an additional build up cup was placed onto the detector in order to warrant secondary charged particle equilibrium. The thickness of the copper build up cups was 4 mm for 6 MV and 10 MV and 8 mm for 18 MV, respectively.

Requested field sizes for PDD measurements [mm x mm]

PBA	MCA
8 x 8	8 x 8
16 x 16	16 x 16
24 x 24	32 x 32
32 x 32	48 x 48
48 x 48	80 x 80
80 x 80	104 x 96
104 x 96	160 x 160
120 x 120	50 x 160
160 x 160	100 x 160
210 x 160	210 x 48
	210 x 96

Table 4.2: Requested field sizes for PBA and MCA measurements

All PDDs were recorded with a SSD of 900 mm up to a depth of 275 mm within the blue phantom in 1 mm steps. As an example, PDDs of all three energies and a reference FS of 104 mm x 96 mm are shown in figure (4.1). In this case, dose was normalized to 100% in a depth of 100 mm. In this representation, it can be seen that the skin dose increased with energy of the incident beam. Another effect of varying photon energy was the different shape of the dose build up region. The tangents on the PDD curves became steeper for smaller energies. Consequently, the depth, where maximum penetration occurred, was shifted towards greater depth for higher energies.

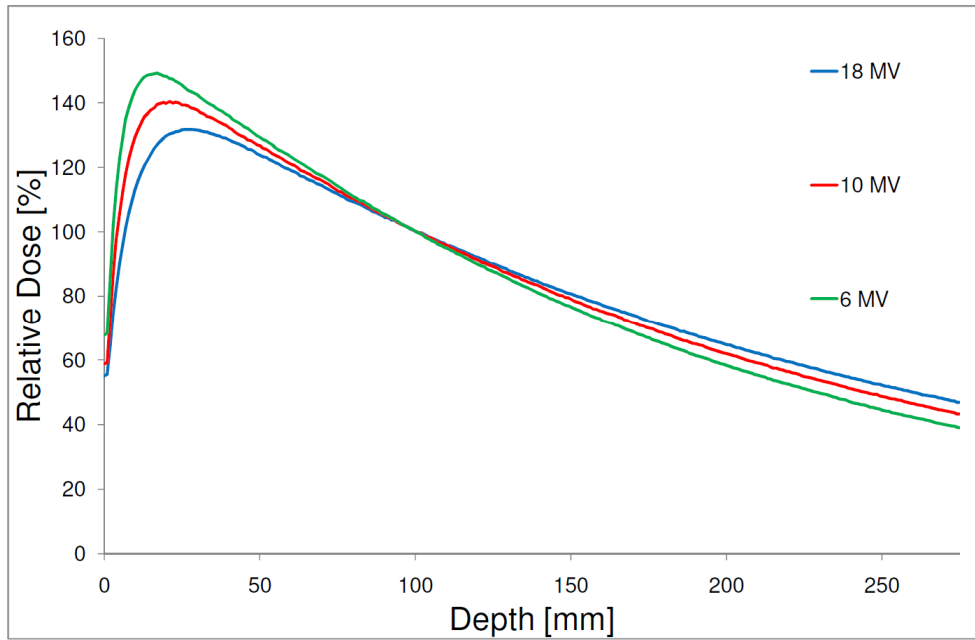


Figure 4.1: PDDs for a 104 mm x 96 mm field, normalized in 100 mm depth.

One can compare depths, where dose maximum occurred, for different energies and different field sizes. In table (4.3), a few results of the comparison are listed.

	<u>Dose maximum depth (d_{max}) [mm]</u>						
	16 x 16	24 x 24	48 x 48	80 x 80	104 x 96	160 x 160	210 x 48
6 MV	16	15	16	17	17	14	16
10 MV	20	21	21	23	21	18	21
18 MV	25	27	28	30	27	25	29

Table 4.3: d_{max} for representative FSs and energies

The shift of d_{max} with increasing beam energy was expected due to the production of secondary electrons, which are scattered more predominantly in forward direction. With rising energies, they consequently deposit their energy a larger distance away from their site of origin.

There are two factors, which influence d_{max} . The beam hardening effect moves d_{max} towards larger depth and the electron contamination lifts it towards the surface. The biggest value of d_{max} was invariably obtained from the 80 x 80 field. Afterwards,

electron contamination from scattering processes in the collimating system disturbed the equilibrium and forced d_{\max} towards shallower depth.

For rectangular FSs, a correction had to be applied. According to d_{\max} and PDD, a rectangular field with a certain area is not equal to a square field with the same area. This is caused by scatter influences. A rectangular field is then equivalent to a square field, as they have the same area to perimeter ratio. The following formulas are helpful for a quick calculation of the equivalent square FS [22].

$$\frac{A}{P} = \frac{a \cdot b}{2 \cdot (a + b)} \quad (4.2)$$

In the formula above, A stands for the area of the field and P for its perimeter. a and b represent width and length of the field, respectively. Because in squares, both sides are equal, a formula for the side length of the equivalent square field can be derived.

$$a = 4 \cdot \frac{A}{P} \quad (4.3)$$

Consequently, by applying such a correction, the rectangular fields in the previous table of the comparison of d_{\max} fitted again into the theory.

In the next two charts, the results of PDDs for 6 MV (figure (4.2)) and 18 MV (figure (4.3)) are visualized for different FSs. Here, the PDDs were normalized to d_{\max} . The impact of a change of FS is clearly visible. The less pronounced dose fall-off of the PDDs, caused by an increasing FS, depends on augmenting scatter radiation in greater depths. Because scattering probability lowers with increasing energy and high energy photons are predominantly scattered in forward direction, the field size dependancy was less pronounced for higher energy beams than for lower [6].

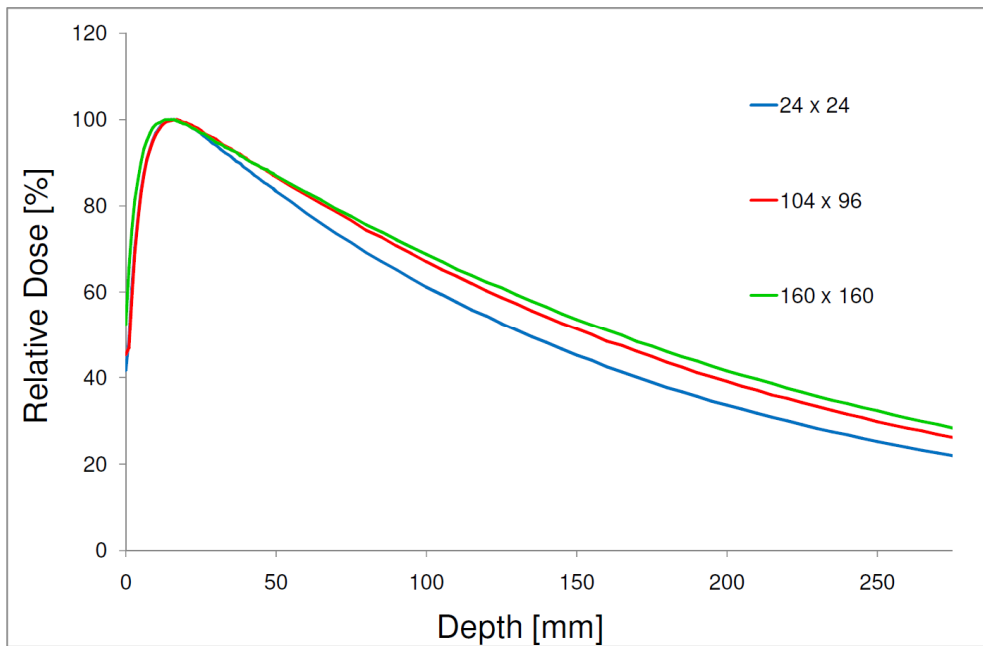


Figure 4.2: 6 MV PDD for different FSs

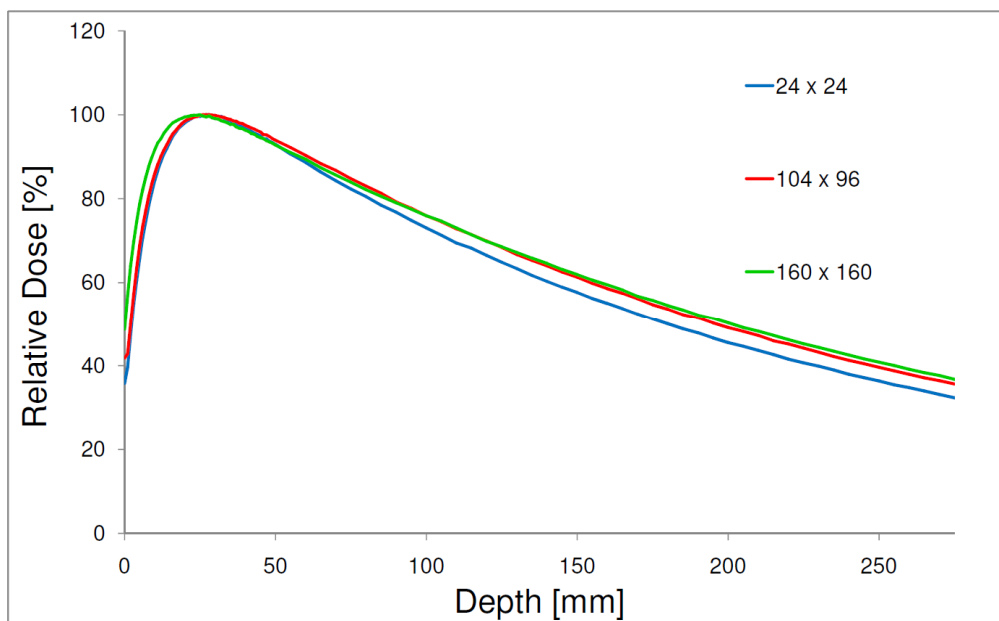


Figure 4.3: 18 MV PDD for different FSs

Air PDDs of all energies for 32 x 32, 104 x 96 and 160 x 160 mm² FSs, are plotted in figure (4.4). Similar behaviour of air PDDs, compared to their counterparts in water, could be detected. As one can see, the discrepancies of the curves were not well pronounced due to the lack of dense matter. The individual curves lied more or less upon another.

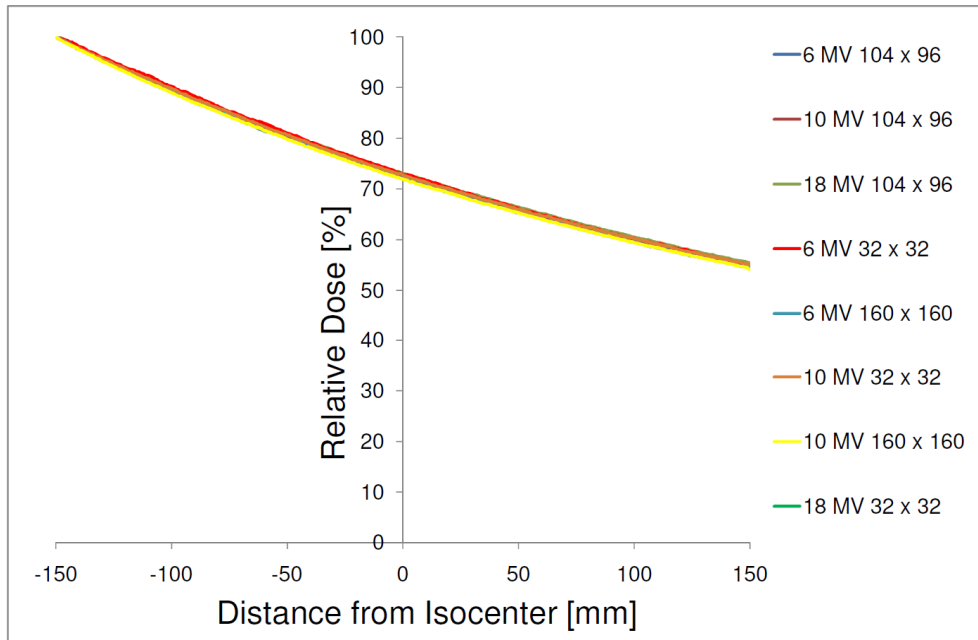


Figure 4.4: PDD in air of all energies for various FS

The results of the air measurements were implemented into the TPS.

4.4 Dose profiles

4.4.1 Definition of the required data sets

Generally, dose profiles indicate the dose variations in off-axis direction in a certain depth.

There are two different kinds of dose profiles. One has to distinguish between diagonal radial and transversal dose profiles. In the case of diagonal radial profiles, the path of the measurement chamber is diagonal across the phantom. In transversal case, the detector moves along and perpendicular to the leaves of the Multi Leaf Collimator (MLC), which shape the required FS. In figure (4.5), a schematic setup of the dose profile measurements is depicted. In the following sections, the two modes are explained in more detail.

Regarding transversal dose profiles, all profiles had also to be determined in air for the MCA, while for PBA only water profiles were required.

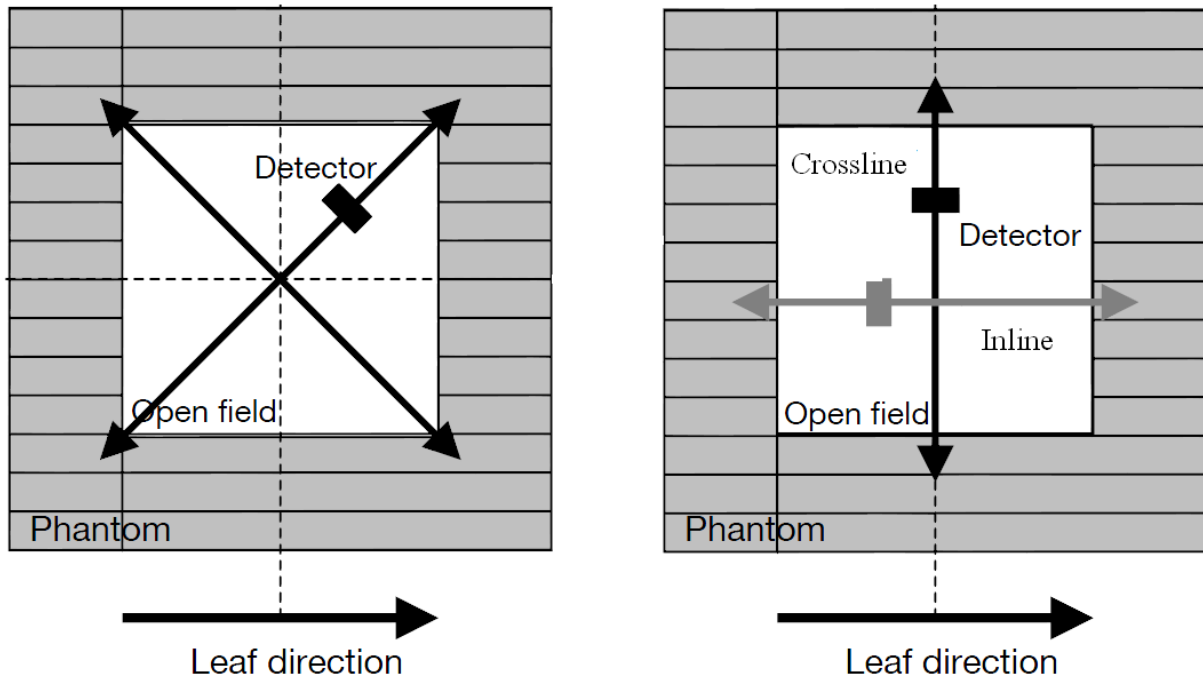


Figure 4.5: Beam's eye view indicating the direction of measurement for diagonal radial (left figure) and transversal profiles (right figure), respectively [23].

4.4.2 Diagonal radial dose profiles

4.4.2.1 Measurement setup

Determination of diagonal radial dose profiles was required for the pencil beam dose calculation algorithm only. The same SSD was set as for the PDD measurements. Again, the diode from Wellhöfer Scanditronix was used. All diagonal radial profiles were measured in several depths, i.e. 5 mm, 14 mm, 25 mm, 50 mm, 100 mm, 200 mm and 350 mm, respectively. Two branches were recorded, one at 37° and the other at 143° diagonally across the required field size of 104 mm x 96 mm. Both datasets were centered and symmetrized and crossline and inline values were converted to absolute radius values using the Pythagorean Theorem. The two branches, obtained from different angle measurements, were averaged and the profiles were normalized to 100% at the radius value, where maximum dose occurred. In this format, diagonal radial dose profiles were communicated to BrainLAB for further data processing procedures. From the measured profiles, the TPS requested radial factors could be derived in order to correct for eventual off axis

inhomogeneities. Afterwards, the obtained radial factors were transferred back for implementation into iPlan®. Due to the assumption of the radial factors to be rotational symmetric, the previous centering- and symmetrizing processes of the datasets was justified.

4.4.2.2 Results

In the following charts, the diagonal radial profiles as well as the processed radial factors are shown for 18 MV.

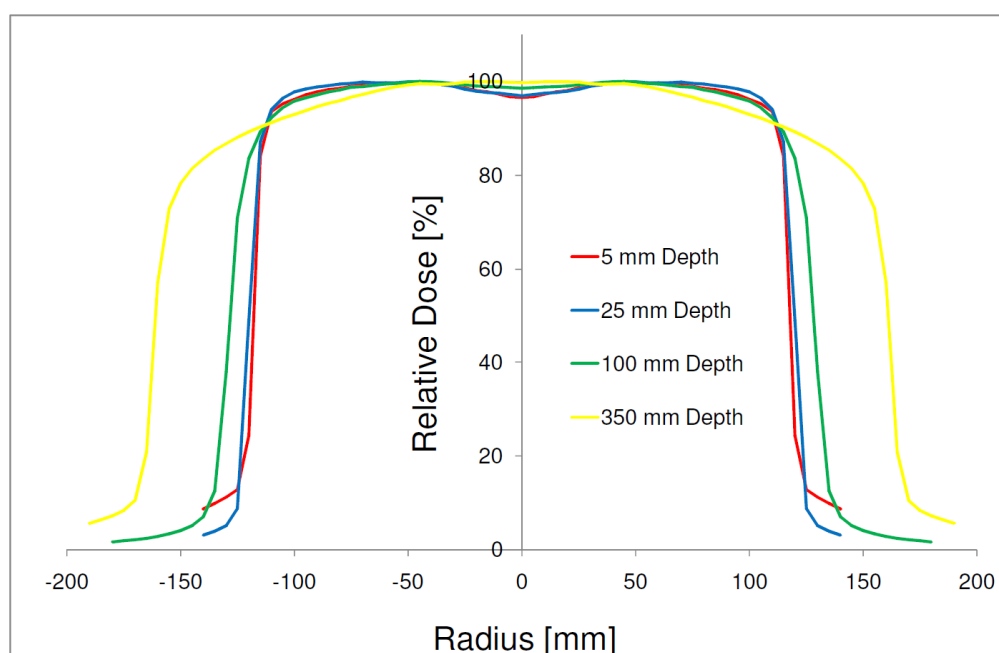


Figure 4.6: 18 MV diagonal radial profiles in various depth, normalized at the radius value where maximum dose occurred.

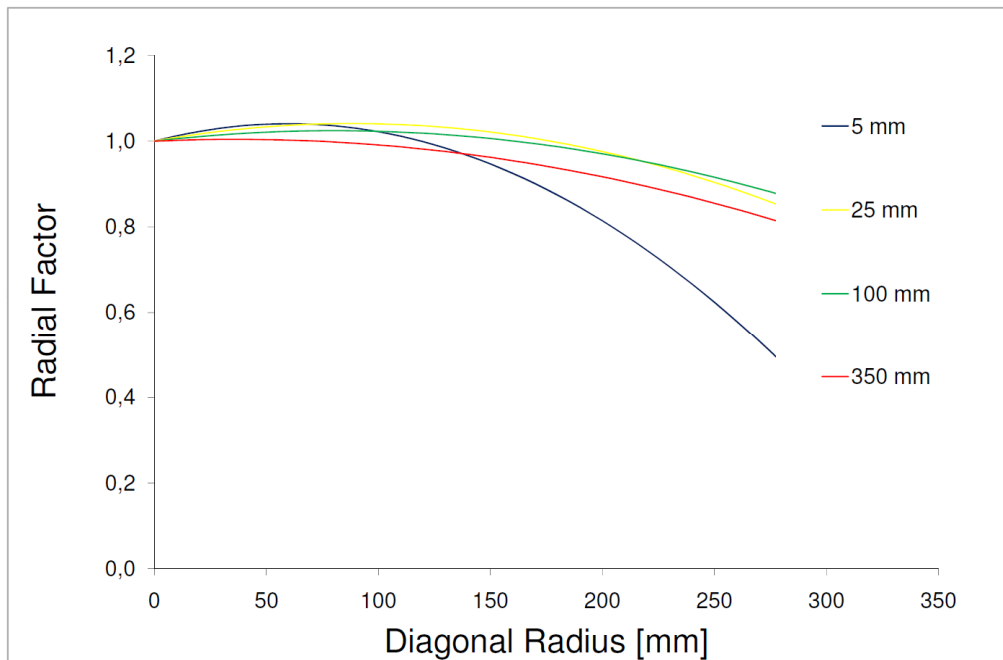


Figure 4.7: Processed radial factors for correction of off axis inhomogeneities.

4.4.3 Transversal dose profiles

Transversal dose profiles were required for the pencil beam algorithm as well as for the Monte Carlo algorithm. They were requested in order to adjust the source function correction and the radiologic field correction. The source function correction is an empirical way of simulating an extended beam source and other effects, which smear out the beam edge. For this reason, the TPS convolves a Gaussian formed curve with certain amplitude and given standard derivation with the calculated dose distribution in order to take the blurring into account. This only influences the penumbra region, which is explained in detail in the next section.

The radiologic field correction allows compensation for small deviations of the radiologic field according to the field size defined by the MLC. Such deviations are caused by non geometric field shapes, round leaf ends and tongue and groove design.

4.4.3.1 Penumbra

The term penumbra refers to a region at the edge of the radiation beam, over which the relative dose changes quickly as a function of the distance from the beam axis. There are several kinds of penumbras, such as the transmission penumbra, the geometric penumbra and the scatter based penumbra.

The transmission penumbra is produced by photons, transmitted through the edge of the collimator.

The geometric penumbra depends on the diameter of the source, SSD and depth.

The combined effect of transmission and geometric penumbras is a region of dose variation at the field edges. A dose profile can be recorded across the beam and its external regions at a certain depth in order to display the extend of the penumbra.

When measuring in a phantom, additional scatter components influence the penumbra. Hence, in dosimetry, the physical penumbra is described by the distance of two specified isodose curves. In this study, the 80% and the 20% isodose curves were used, respectively, as shown in figure (4.8).

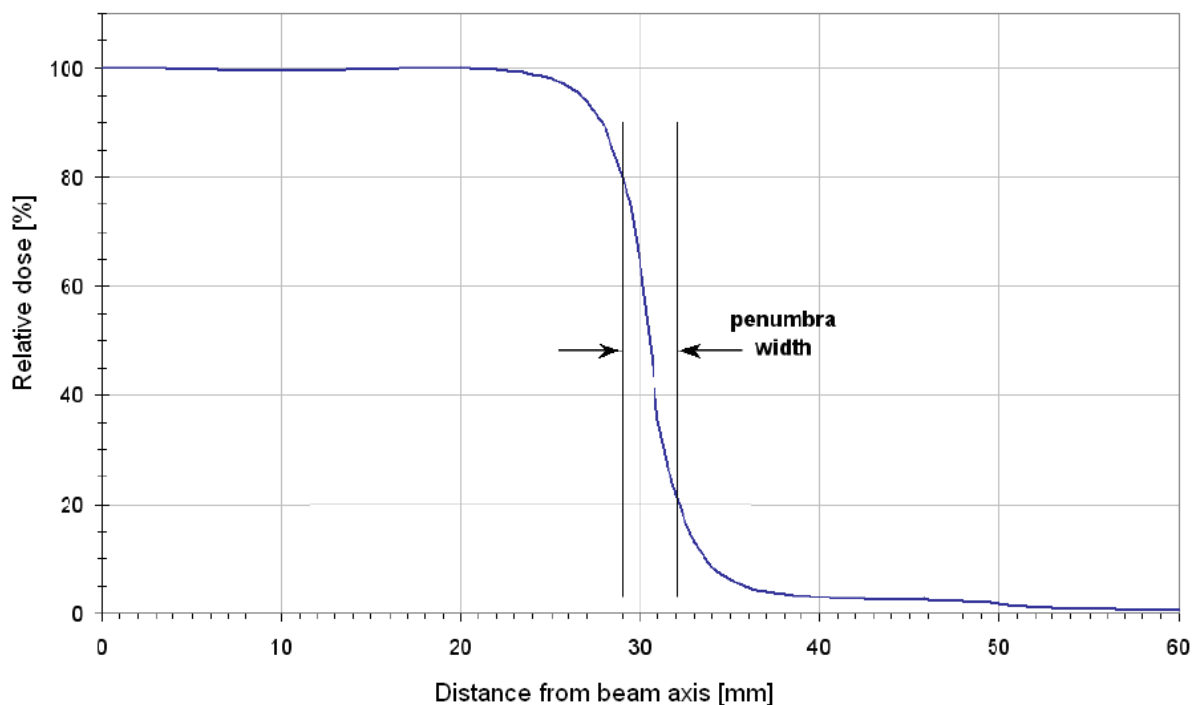


Figure 4.8: Illustration of the definition of the penumbra as distance of the 20% and 80% isodoses

4.4.3.2 Measurement setup

In case of basic beam data measurements according to the PBA, BrainLAB transmitted a so called '*Patient Setup Field*', which was used as a template to adjust the field shape. It was set as follows. The leafs 14, 18 – 22 and 25 – 28 were open and were positioned at -75 mm on the left and at 25 mm on the right side. In figure (4.9), the mentioned field shape is illustrated graphically.

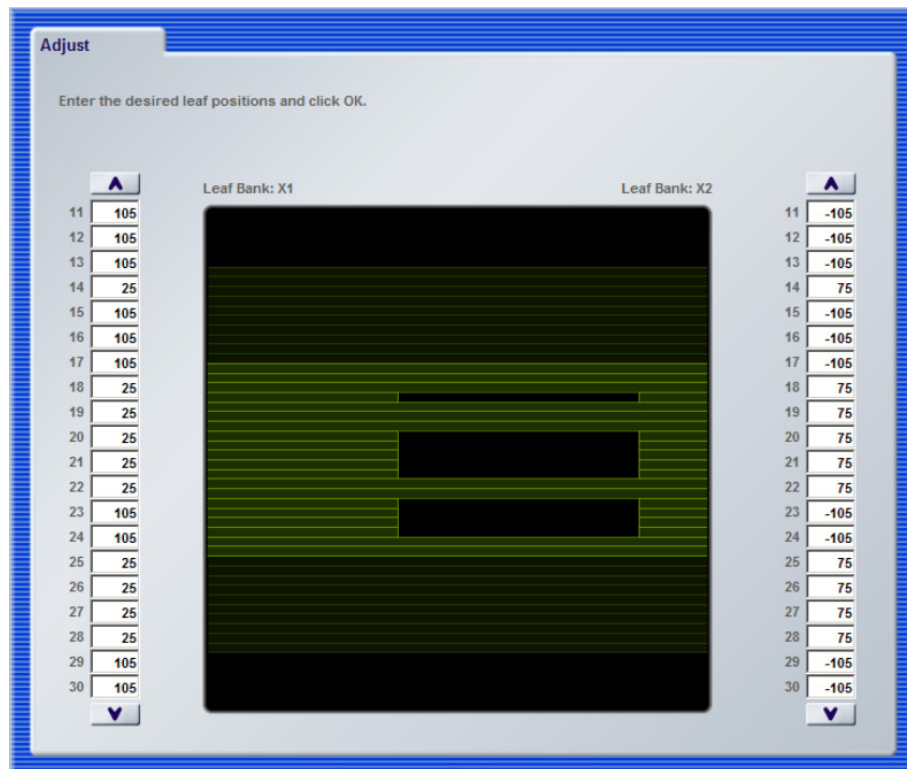


Figure 4.9: BrainLAB patient setup field

Two profiles were recorded in depth of d_{\max} according to each energy and at 100 mm and 200 mm depth. One along the leaf direction (inline) and the other perpendicular to the leaf direction (crossline). The obtained transversal dose profiles were normalized at the location where maximum dose occurred. Additionally, the penumbra of the profiles had to be checked. The penumbra region should be approximately 4 mm for depth less than 50 mm, as specified by the working instructions transmitted by BrainLAB [23].

4.4.3.3 Results

In the following charts (figure (4.10) and figure (4.11)), the measured 6 MV transversal dose profiles in inline and crossline direction are shown.

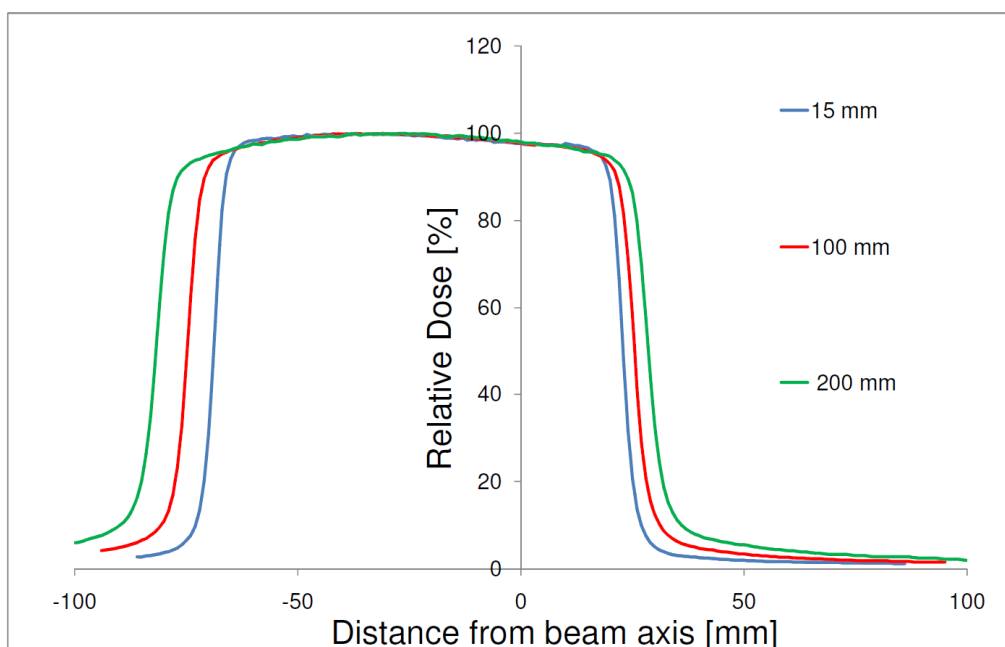


Figure 4.10: Measured 6 MV inline transversal profiles

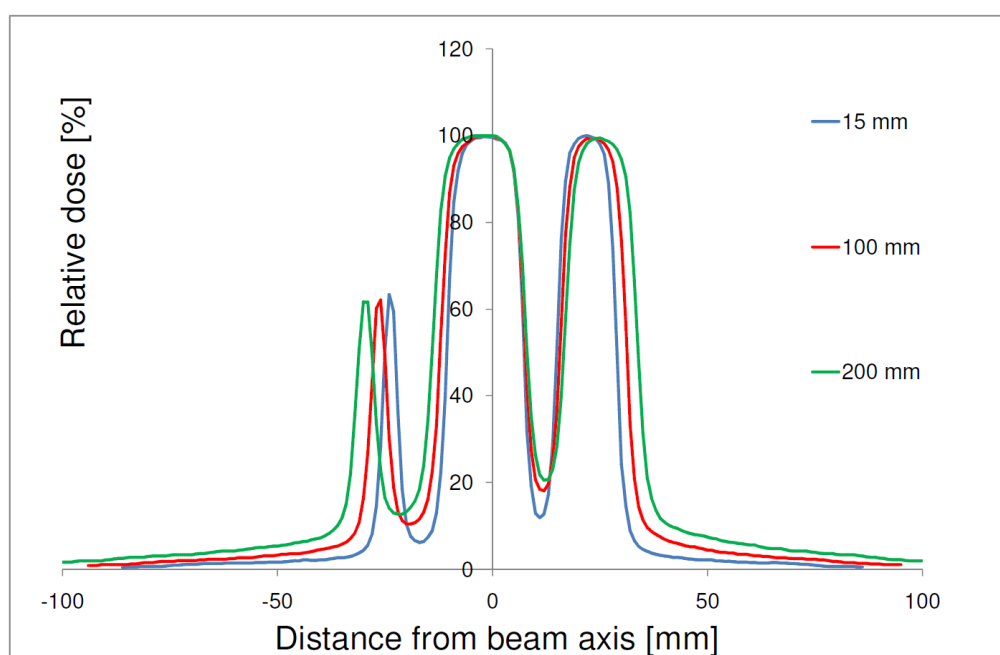


Figure 4.11: Measured 6 MV crossline transversal profiles

In table (4.4), the respective widths of the penumbras in inline direction are listed. One can see that the above mentioned specifications are met. Obviously, the penumbra widths increased with increasing depths. It is also visible that the size of the penumbra was dependent on energy because the higher the energy, the more transparent the leaves of the MLC become.

<u>Penumbra width of the inline profiles [mm]</u>			
	$d_{max} \equiv 15, 25, 30 \text{ mm depth}$	100 mm depth	200 mm depth
6 MV	3.9	4.8	5.7
10 MV	4.2	5	5.8
18 MV	4.9	5.5	6.3

Table 4.4: Results of the penumbra of the patient setup field in inline direction for all energies at various depths

In case of measurements of transversal dose profiles according to the MCA, other FSs were required. The FSs, for which transversal dose profiles in various depths were requested, were such as listed in table (4.2). The measurement setup was equal to the acquisition of dose profiles with the patient setup field for the PBA. Again, transversal dose profiles were recorded at depths of d_{max} for the particular energies and at 100 mm and 200 mm depth. Using the example of the 6 MV beam and a representative FS of 210 mm x 48 mm, a comparison of the profiles in different depths took place. The resulting plot is shown below.

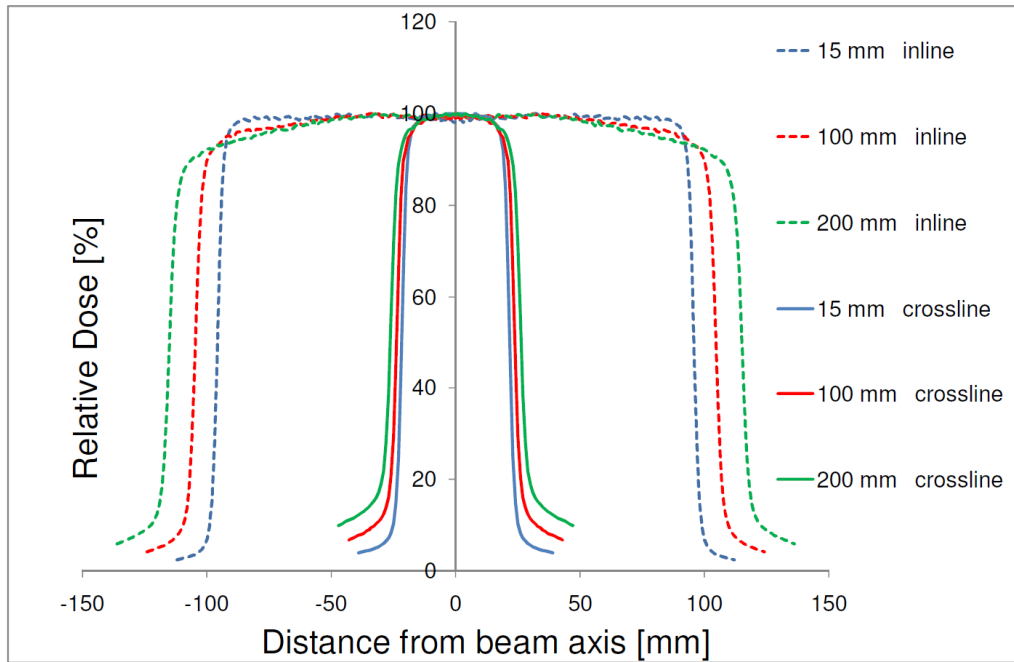


Figure 4.12: 6 MV inline and crossline transversal profiles for a FS of 210 mm x 48 mm

The results of the penumbra widths are listed in table (4.5).

Penumbra width [mm]

Inline profile of 210 mm x 48 mm field

	$d_{max} \equiv 15, 25, 30 \text{ mm depth}$	100 mm depth	200 mm depth
6 MV	3.4	4.4	5.5
10 MV	3.7	4.5	5.5
18 MV	3.7	4.5	5.5

Crossline profile of 210 mm x 48 mm field

	$d_{max} \equiv 15, 25, 30 \text{ mm depth}$	100 mm depth	200 mm depth
6 MV	3.3	4.0	5.3
10 MV	3.9	4.6	5.5
18 MV	3.9	4.6	5.5

Table 4.5: Results of the penumbra for all energies in various depths in water

All transversal dose profiles concerning MCA were measured in water as well as in air. In the following chart (figure (4.13)) and table (4.6), the results of the measurements in air are presented. Air profiles were recorded with the diode in combination with a build up cap.

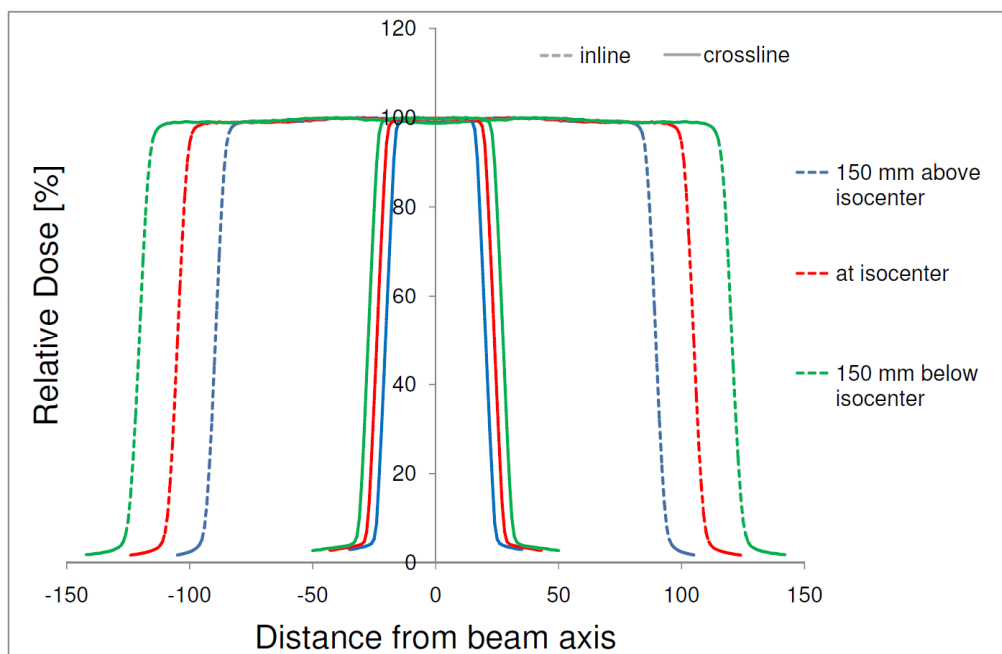


Figure 4.13: 6 MV inline and crossline profiles in air for a FS of 210 mm x 48 mm

Penumbra width [mm]

Inline profile of 210 mm x 48 mm field

	<i>150 mm above isocenter</i>	<i>At isocenter</i>	<i>150 mm below isocenter</i>
<i>6 MV</i>	5.1	5.4	5.5
<i>10 MV</i>	5.0	5.3	5.5
<i>18 MV</i>	5.4	5.5	5.9

Crossline profile of 210 mm x 48 mm field

	<i>150 mm above isocenter</i>	<i>At isocenter</i>	<i>150 mm below isocenter</i>
<i>6 MV</i>	5.0	5.0	5.1
<i>10 MV</i>	5.0	5.0	5.1
<i>18 MV</i>	5.3	5.4	5.4

Table 4.6: Results of the penumbra in air for all energies at various distances from target

For the air profiles it can be seen that they were sharper at the edges of the beam. This is caused by the reduction of scatter radiation. The penumbra width was more or less comparable to the results of the water measurements. It was obvious that the penumbra is larger for greater depth, but less pronounced in the case of air measurements. Another result was an increasing penumbra with increasing energy. This again is caused by the fact that the field shaping leafs of the MLC become more transparent for beams with rising energy.

4.5 Scatter factors

4.5.1 Definition

The dose, which is delivered to a specific point in a phantom or a patient, contains two different components. The first component consists the primary photons, which are emitted from the X-ray target. The second contribution is the dose delivered by scattered photons. The scattered photons may originate either from the collimating device or from the phantom, in which measurements take place. Both contributions can be considered separately. The contribution from the collimating device can be measured by a simple setup in (no phantom) and the contribution of phantom scatter by placing a detector in the full scatter water phantom in order to take phantom scattering into account as well.

Due to variation of the linac output, as a result of different FSs, a treatment planning system needs to know the exact relationship for each output (OP) compared to a reference setting in order to predict dose distributions for different field sizes.

The scattered radiation, originating from the collimator and the components in the treatment head, is highly dependent on the FS. The Output Factor (OPF) in air describes the field size dependent difference of the linac output (OP). It is defined as the quotient of the OP of the linac for a given FS and the output for a certain reference FS, as stated in formula (4.4).

$$OPF_{air} = \frac{OP_{(FSZ)}}{OP_{(FSZ_{ref})}} \quad (4.4)$$

In the context of this study, a 104 mm x 96 mm field served as a reference field.

It was measured in air in the isocenter under reference conditions with an ionization chamber and a build up cap.

The scatter, caused by the phantom, depends on the irradiated volume, the characteristics of the medium and of the radiation quality. A quantitative description of this scatter radiation is the so called phantom scatter ratio (PSR). It describes the change of delivered dose to a reference depth in a water phantom, taking into account scattered photons from the phantom, as the FS is changed. It is defined as the quotient of the Dose Rate (DR) for a given FS and the DR for the 104 mm x 96 mm reference field, as illustrated in formula (4.5).

$$PSR = \frac{DR_{(FSZ)}}{DR_{(FSZ_{ref})}} \quad (4.5)$$

The PSR cannot be measured directly. A way round has to be undertaken by using the Total Scatter Factor (TSF), which can be measured by placing a detector in a reference depth of a water phantom with a certain SSD. By exchanging PSR through TSF in formula (4.5), TSF can be obtained. TSF sums up the scatter contributions from both, collimator and phantom material.

By using the following equation (formula (4.6)), PSR can be specified to

$$PSR = \frac{TSF}{OPF} \quad (4.6).$$

Since scatter factors provide information relative to the nominal linac output, it was important to measure under the same reference conditions concerning SSD and reference depth, as stated in section (4.2). For the implementation in iPlan®, TSFs and OPFs of all FSs, as listed in table (4.2), were required. According to formula (4.3), rectangular fields had to be converted into the corresponding square fields in order to satisfy the monotone progress of the scatter-FS-curve. The results were as follows.

4.5.2 Results

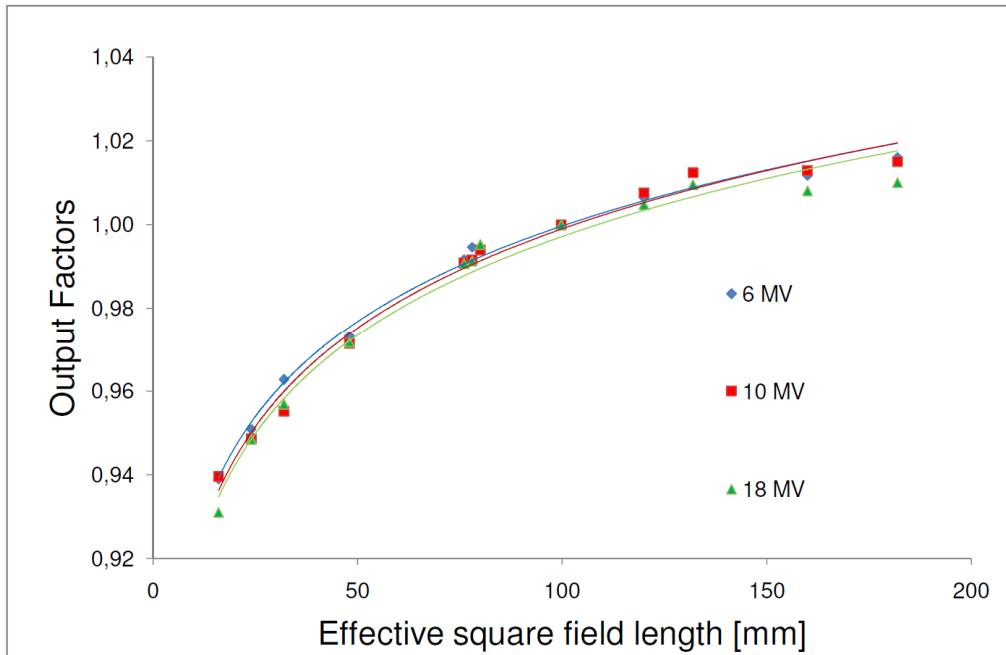


Figure 4.14: Output factors in air for effective field size lengths and the respective logarithmical fits

From the resulting chart (figure 4.14) is visible that scatter increased with increasing effective FS. This was expected due to the augmenting number of opportunities of the photons to be scattered, either from collimator leaves or flattening filter. Subsequently, the discrete sample points were fitted logarithmically and the fits are also shown in figure (4.14).

In the following, the results of the TSFs are shown.

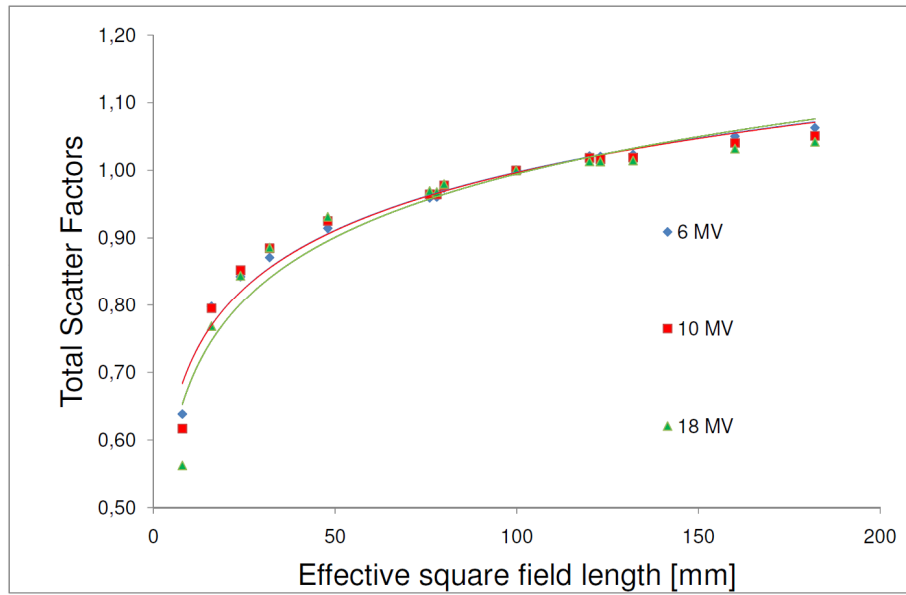


Figure 4.15: Total scatter factors for effective field size lengths and the respective logarithmical fits

As expected, TSFs also increased with increasing effective FS. Compared to the results of the OPF measurements, it was obvious that TSFs vary in a much more pronounced manner than OPFs did. This can be explained by the consideration of non proportional more scatter possibilities for a single photon due to the material above the point of measurement. From these results, PSRs could be derived by utilizing equation (4.6). The results were as depicted in figure (4.16).

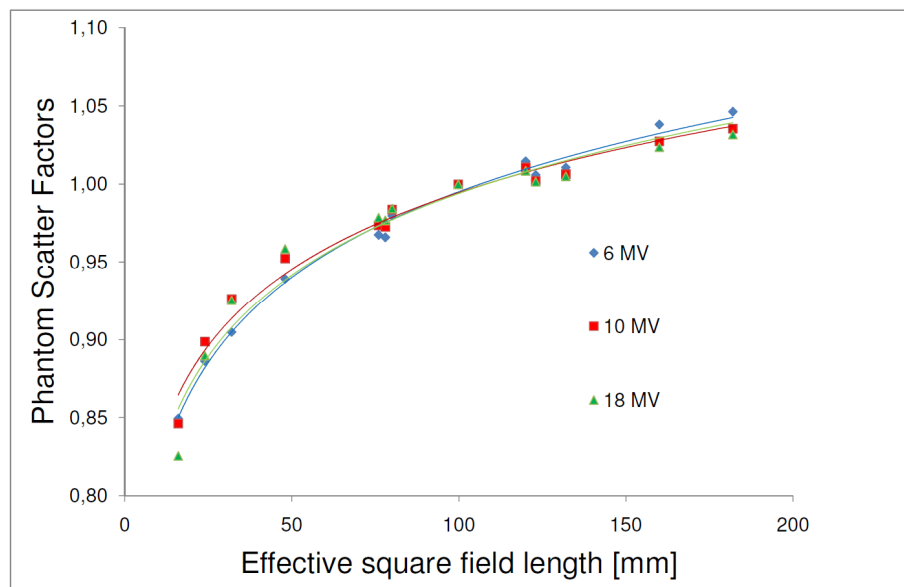


Figure 4.16: Phantom scatter factors for effective field size lengths and the respective logarithmical fits

4.6 Acceptance and commissioning of iPlan®

After the collection and implementation of the basic beam data, the commissioning of the TPS took place. Such a commissioning procedure requires a quantitative comparison between measured and calculated dose distributions, in order to check correctness and accuracy of the TPS. A common way of determining accordance of calculated and measured dose is by the use of the so called Gamma evaluation. A parameter, the γ -Index, is introduced to develop a pass or fail acceptance test. The method of Gamma evaluation is briefly described in the next chapter.

4.6.1 Gamma evaluation

In order to perform a Gamma evaluation, measurement data serve as reference data. As a next step, two criteria have to be defined, i.e. dose- difference criterion (ΔD_M) and Distance To Agreement criterion (DTA) (Δd_M). In figure (4.17), a graphical illustration of the way, how the γ - Index is calculated, is shown.

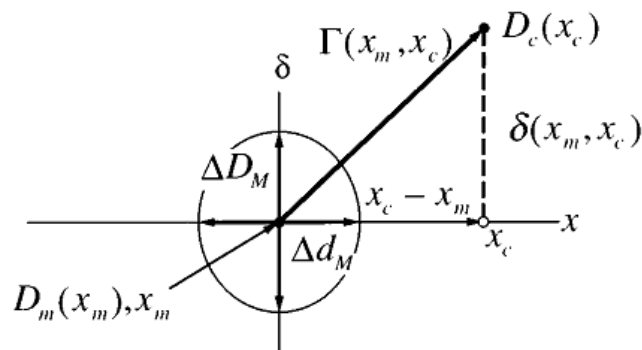


Figure (4.17): Illustration of the principle of Gamma evaluation

The γ -Index depicts a method to simultaneously consider both criteria, dose difference and DTA criterion. In the origin of figure (4.17), the measuring point is located, around which an ellipse is drawn, whose surface represents acceptance boundary conditions. The equation of the applied ellipse is as follows.

$$\sqrt{\frac{x^2(\vec{x}_m, \vec{x})}{\Delta d^2_M} + \frac{\delta^2(\vec{x}_m, \vec{x})}{\Delta D^2_M}} = 1 \quad (4.7)$$

Where

$$x = |\vec{x} - \vec{x}_m| \quad (4.8)$$

and

$$\delta = D(\vec{x}) - D_m(\vec{x}_m) \quad (4.9)$$

The index m refers to the measured quantity. $D_c(\vec{x}_c)$ in the chart above depicts the calculated dose at the calculated position. If the vector, originating from the origin of the coordinate system and pointing to this position, doesn't intersect the surface of the ellipse, the calculation passes at the point of measurement.

One can define a function $\Gamma(\vec{x}_m, \vec{x}_c)$ to characterize an ellipse for dose comparison purposes and a consequential scalar $\gamma(\vec{x}_m)$ as follows.

$$\Gamma(\vec{x}_m, \vec{x}_c) = \sqrt{\frac{x^2(\vec{x}_m, \vec{x}_c)}{\Delta d^2_M} + \frac{\delta^2(\vec{x}_m, \vec{x}_c)}{\Delta D^2_M}} \quad (4.10)$$

and

$$\gamma(\vec{x}_m) = \min\{\Gamma(\vec{x}_m, \vec{x}_c)\} \forall \vec{x}_c \quad (4.11)$$

By this definition of shortest distance between a calculated dose point and a reference point, the requested pass or fail test is generated.

One can say that the initial criteria are fulfilled, if $\gamma(\vec{x}_m) \leq 1$ or not fulfilled, if $\gamma(\vec{x}_m) > 1$ [25]. Afterwards, the calculation is carried out for all measurement points in order to receive full information on agreement or disagreement.

For a detailed explanation, [25] and [26] can be consulted.

4.6.2 Results

Some aspects of commissioning of the pencil beam algorithm in iPlan® are presented next. In a first step, a relative dosimetry comparison of PDDs and dose profiles for all energies and certain square fields took place (a). Thereafter, another relative comparison of dose profiles of the irregular field geometry (Patient setup field by BrainLAB (figure (4.9))) was fulfilled (b).

a) Gamma evaluation of depth dose curves and dose profiles

To compare ionization chamber measurements in the water phantom to the dose distributions, calculated by iPlan® TPS, an in-house developed software (Excel macro) was applied. This software was previously tested for dosimetric comparison purposes between film, chamber, diode measurements and TPS calculations.

For the presentation of results, the γ - Index was calculated for depth dose curves and dose profiles. From these data sets, representative values such as maximum value, mean value and standard deviation were extracted.

To evaluate the dose calculation accuracy of the TPS, a DTA of 2 mm and a dose difference criterion of 2% were chosen.

For field sizes of 24x24, 48x48, 104x104 and 160x160 mm², PDDs were measured and extracted from iPlan® TPS, respectively. All the profiles were measured and evaluated at 100 mm depth and a SSD of 900 mm. The results of the Gamma analysis of the PDDs are listed in the table below.

Representative Gamma Indexes for PDD comparisons

	6MV				10 MV				18MV			
FS	24x24	48x48	104x104	160x160	24x24	48x48	104x104	160x160	24x24	48x48	104x104	160x160
γ -max	0.14	0.13	0.08	0.11	0.12	0.13	0.13	0.13	0.13	0.12	0.13	0.13
γ -mean	0.05	0.04	0.02	0.03	0.04	0.04	0.03	0.03	0.03	0.03	0.03	0.03
γ -stdev	0.03	0.03	0.02	0.03	0.03	0.03	0.02	0.03	0.03	0.03	0.02	0.03

Table 4.7: Results of the Gamma evaluation of PDDs

No trends or systematic dependencies were found for these evaluations. The calculated depth dose of the TPS agreed very well with data obtained from ion chamber measurements.

Below, the plots of the Gamma evaluation of the best and the worst case are shown.

The square field of 104 mm x 104 mm showed best results with an energy of 6 MV.

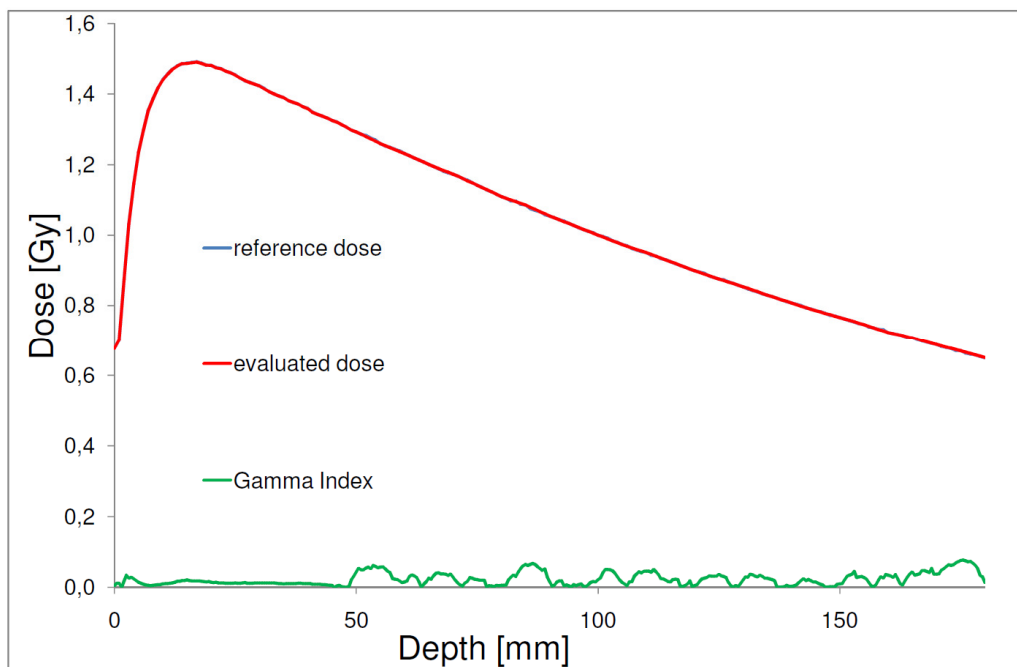


Figure 4.18: 6 MV Gamma evaluation of PDD for 104 mm x 104 mm FS (best result)

Worst results were obtained from the 24 mm x 24 mm square field with an energy of 6 MV. This is shown in figure (4.19) on the next page.

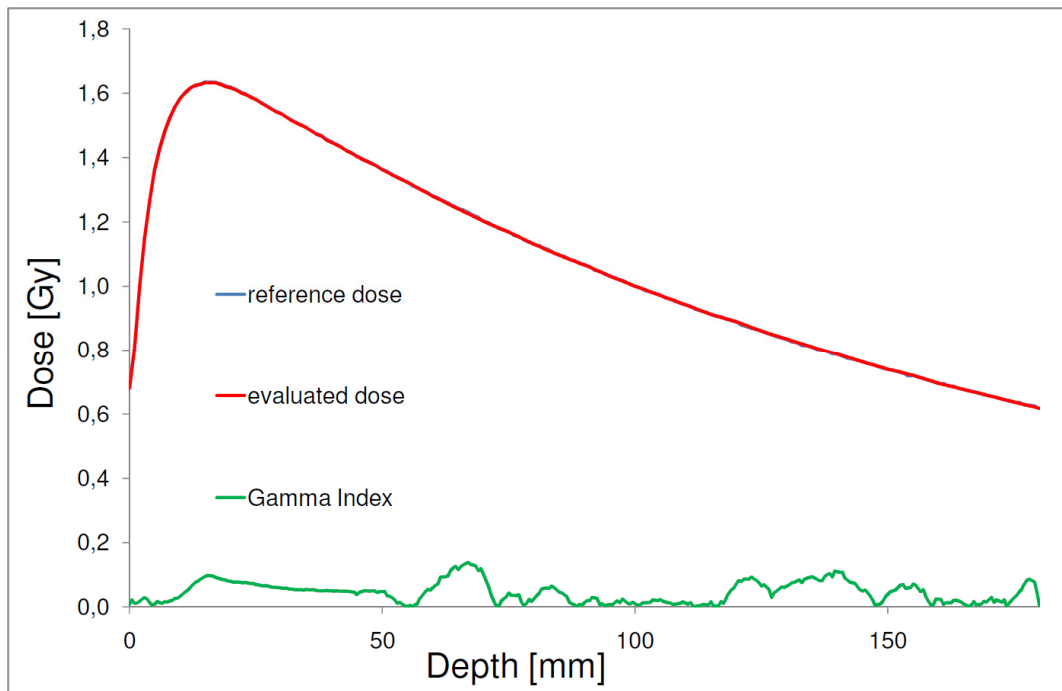


Figure 4.19: 6 MV Gamma evaluation of PDD for 24 mm x 24 mm FS (worst result)

In case of lateral dose profile comparisons, the results showed more discrepancies. Maximal Gamma Indexes of up to 3 were obtained in the penumbra region. This worst case is illustrated in figure (4.20).

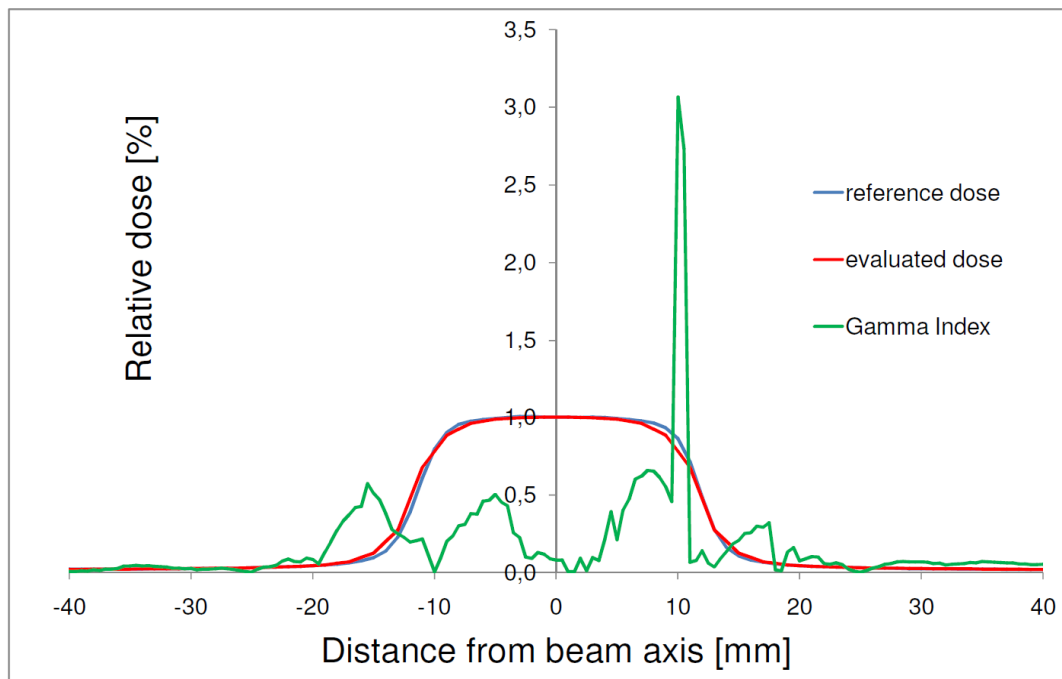


Figure 4.20: 6 MV Gamma evaluation of a crossline profile for 24 mm x 24 mm FS (worst result)

Average γ -Indexes were located in the region of 0.2 up to γ - values of maximal 0.43. In the next table, representative Gamma Indexes according to lateral dose comparisons are listed.

Representative Gamma Indexes for dose profile comparisons

	<i>6MV crossline</i>			<i>10MV crossline</i>			<i>18MV crossline</i>		
<i>FS</i>	<i>24 x 24</i>	<i>104 x 104</i>	<i>160 x 160</i>	<i>24 x 24</i>	<i>104 x 104</i>	<i>160 x 160</i>	<i>24 x 24</i>	<i>104 x 104</i>	<i>160 x 160</i>
<i>γ-max</i>	3.07	2.06	0.53	0.78	0.78	0.98	1.14	0.78	1.67
<i>γ-mean</i>	0.11	0.32	0.21	0.14	0.29	0.43	0.18	0.29	0.37
<i>γ-stdev</i>	0.29	0.40	0.15	0.17	0.18	0.22	0.31	0.20	0.43

	<i>6MV inline</i>			<i>10MV inline</i>			<i>18MV inline</i>		
<i>Depth</i>	<i>24 x 24</i>	<i>104 x 104</i>	<i>160 x 160</i>	<i>24 x 24</i>	<i>104 x 104</i>	<i>160 x 160</i>	<i>24 x 24</i>	<i>104 x 104</i>	<i>160 x 160</i>
<i>γ-max</i>	0.63	0.56	0.81	0.49	0.83	1.16	0.40	0.77	1.22
<i>γ-mean</i>	0.12	0.14	0.16	0.13	0.26	0.33	0.10	0.23	0.32
<i>γ-stdev</i>	0.12	0.11	0.14	0.12	0.19	0.27	0.09	0.19	0.33

Table 4.8: Results of the Gamma evaluation of dose profiles of square fields

b) Gamma evaluation of the irregular field profiles

In this case, measured data of the collection of the basic beam data were used as a reference data set. The BrainLAB patient setup field was suggested for acceptance testing purposes. In the table below, the obtained results are listed.

Representative Gamma Indexes for dose profile comparisons of patient setup field

	<i>6MV crossline</i>			<i>10MV crossline</i>			<i>18MV crossline</i>		
<i>Depth</i>	<i>15 mm</i>	<i>100 mm</i>	<i>200 mm</i>	<i>25 mm</i>	<i>100 mm</i>	<i>200 mm</i>	<i>30 mm</i>	<i>100 mm</i>	<i>200 mm</i>
<i>γ-max</i>	1.45	2.03	2.25	0.10	2.08	2.27	2.000	3.96	4.55
<i>γ-mean</i>	0.19	0.26	0.35	0.24	0.21	0.31	0.28	0.30	0.38
<i>γ-stdev</i>	0.20	0.32	0.36	0.18	0.26	0.40	0.24	0.51	0.66

	<i>6MV inline</i>			<i>10MV inline</i>			<i>18MV inline</i>		
<i>Depth</i>	<i>15 mm</i>	<i>100 mm</i>	<i>200 mm</i>	<i>25 mm</i>	<i>100 mm</i>	<i>200 mm</i>	<i>30 mm</i>	<i>100 mm</i>	<i>200 mm</i>
<i>γ-max</i>	1.19	0.79	0.75	1.16	0.80	0.73	1.230	1.06	0.850
<i>γ-mean</i>	0.30	0.26	0.28	0.31	0.30	0.30	0.37	0.31	0.29
<i>γ-stdev</i>	0.26	0.22	0.20	0.25	0.19	0.17	0.32	0.27	0.21

Table 4.9: Results of the Gamma evaluation of dose profiles of the patient setup field

Best results regarding average γ -Indexes showed the crossline profile of 6 MV in 15 mm depth, which is depicted in figure (4.21).

According to both, maximal and mean γ -Indexes, the Gamma evaluation of the crossline profile, obtained from the 18 MV beam at a depth of 200 mm, showed worst results. This scenario is plotted in the chart thereafter. Mostly, the maximum Gamma values were located in the dose valleys, i.e. beneath the blocking leaves in the patient setup field. In the region, which represents a small FS, e.g. at the place where just one leaf was open, large Gamma values could be detected as well. One can claim that the accuracy of dose calculation decreases in regions of strongly pronounced dose gradients.

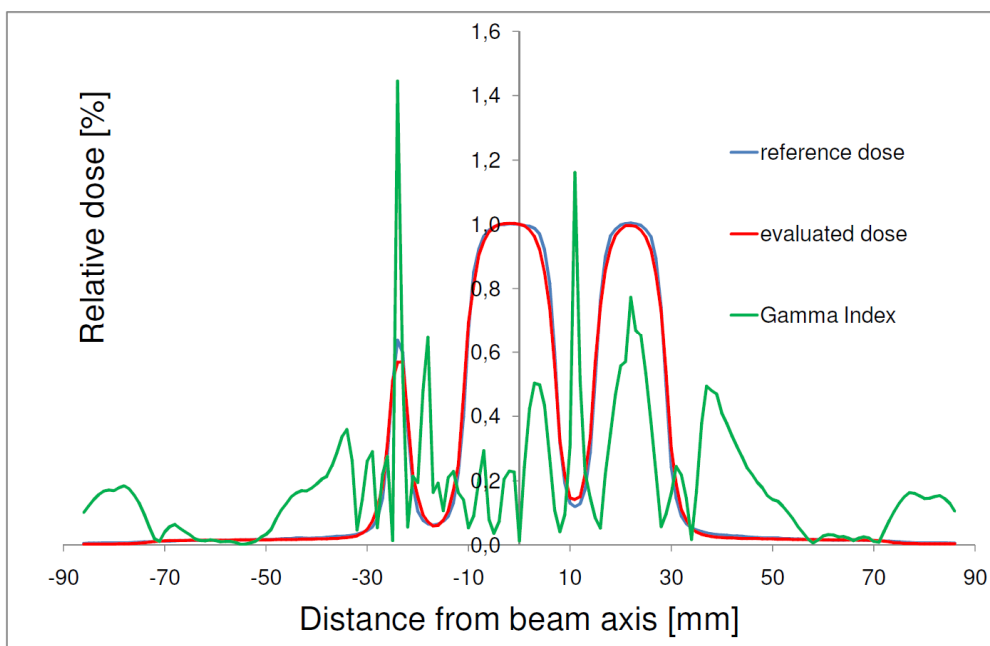


Figure 4.21 : 6 MV Gamma evaluation in 15 mm depth (best case)

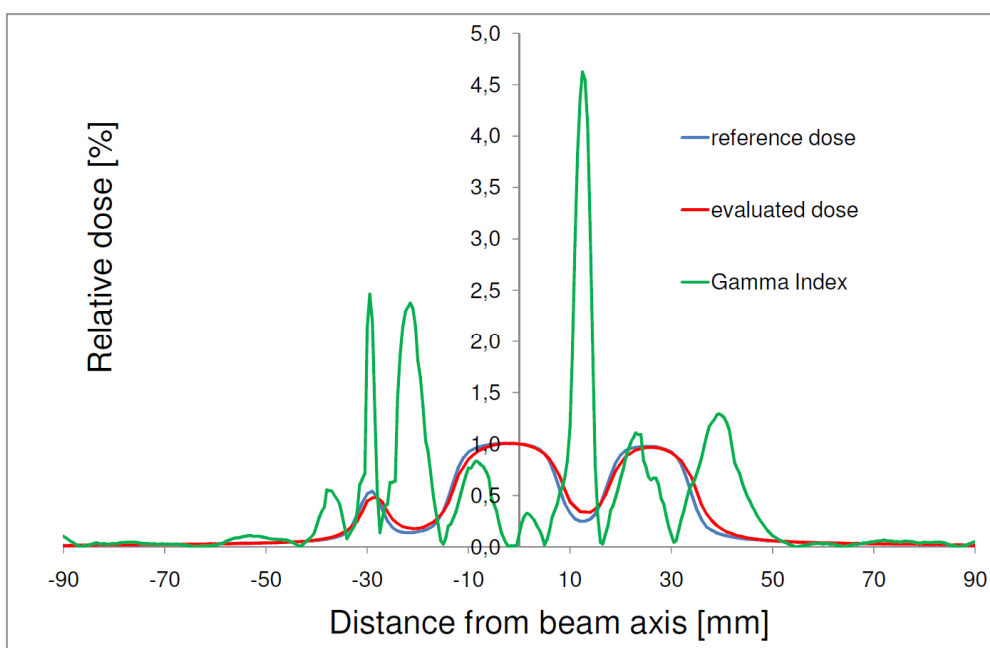


Figure 4.22: 18 MV Gamma evaluation in 200 mm depth (worst case)

In case of Monte Carlo algorithm commissioning, acceptance was performed by an engineer of BrainLAB. For this purpose, the MCA had to be verified by comparison with the PBA using dose calculations in a virtual water phantom. The accepted limit for the maximum dose difference within a radius of 40 mm of the central beam axis of

PBA and MCA could be achieved. Also the constrain for the deviation of PBA and MCA calculated position of the 50% isodose of 0 mm could be approved.

In both cases, PBA as well as MCA, the accuracy of dose prediction was clinically acceptable, due to the very low mean deviations from the doses obtained by measurements. Very high values of the γ -Index occurred seldomly and thus they were clinically acceptable.

For patients single beams are not used and for composite treatment plans deviations between measurements and calculations are more complex.

5 Adaptive Dose Calculation

5.1 Introduction

New technologies and methods in radiation oncology, such as Intensity Modulated Radiation Therapy (IMRT), require accurate beam targeting and image guidance. By the implementation of IGRT, the large safety margins around the CTV can be reduced and consequently, sparing of OARs and healthy tissue can be achieved [27]. Also underdosage of the tumor may be avoided by the possibility to deliver higher dose to the Planning Target Volume.

So far, CBCT data sets were mostly used for corrections of patient positioning uncertainties. This can be achieved by matching CBCT images, acquired prior to every treatment fraction, to bony as well as to soft tissue reference structures in the initial planning CT.

The next logical step in usage of CBCT data is to test the applicability for ART. As a consequence of a fractionated radiation treatment and long treatment times (up to 6 weeks), anatomical changes in the body of the patient can occur. Changes can be weight loss of the patient, atelectasis and shrinking tumor [29]. A possible solution to take this into account might be a quasi real time re-planning procedure of the treatment plan, based on CBCT images. The re-planning task incorporates recontouring and modifications of the initial treatment plan. Consequently, patient's conditions at the treatment day could be considered [28].

In the last chapter of this study it should be evaluated, whether CBCT based dose calculation is accurate enough for clinical implementation. In case of sufficient accuracy, this would provide a powerful option to assess the daily and accumulated dose in diverse OARs and the tumor, without using repetitive planning CTs.

The procedure for evaluating dose accuracy was as follows. The most important step for treatment planning purposes based on CBCT data is to determine so called HU/ED Calibration curves. They provide a relation between Hounsfield Units (HU) (see section (5.2)), obtained from CT and CBCT images, and Electron Density (ED)

of the imaged materials. ED information is a necessary input for each dose calculation algorithm. These calibration curves were established by scanning various phantoms (see section (2.5.3)) with CT and CBCT, respectively, and determining HUs in their material inserts. By plotting the obtained HUs as a function of ED, the calibration curve was found. Thereafter, an inhomogeneous slab phantom was scanned and a dose calculation for an Anterior-Posterior (AP) beam was carried out. With the help of a Gamma evaluation, the PDDs, which were obtained from CT- and CBCT-based dose calculation, were compared.

5.2 Hounsfield units

The quantity of Hounsfield Units (HU) is a physical quantity, which describes the density of a certain material in relation to water. The HU value comprises a simple linear transformation, in order to relate various attenuation coefficients of different materials to the attenuation coefficient of water. Mathematically, the HU scale is defined as follows.

$$HU = 1000 \cdot \left(\frac{\mu - \mu_w}{\mu_w} \right) \quad (5.1)$$

Where μ_w refers to the absorption coefficient of water. The HU scale is frequently used in clinical practice because water can be considered to be the most dominant material in the human body. HUs of voxels and ROIs can be readout in the software environment of the TPS. Attenuation coefficients and hence HUs depend amongst other factors on ED and therefore also on the relative ED related to water. Below, ED always refers to the ED relative to water.

5.3 HU/ED calibration curves

All HU/ED calibration curves were obtained by imaging two phantoms, the Gammex® RMI and CATPhan® phantom. Each phantom contains different tissue equivalent and tissue substitute material inserts. The two phantoms were scanned with various

imaging protocols, in order to receive proper correlation curves representing each clinically used protocol. According to the CBCT case, the protocols, including their appropriate image acquisition parameters, which were used for the generation of calibration curves, are listed in table (2.3) in chapter (2.1.2). Regarding CT images, which were used for dose comparison purposes, the clinical presets H&N, chest and pelvis were considered. They were all acquired by the use of the Siemens Volume Zoom CT scanner, mentioned in section (2.2).

By the construction of the appropriate HU/ED curves, the dependency on image acquisition parameters of the protocols was evaluated.

After image acquisition, CT and CBCT data sets of the two phantoms were loaded into the TPS iPlan®. By using the integrated HU measuring tool in the TPS software, several samples were taken in each insert, in order to obtain average values. In case of the Gammex® RMI phantom, the ED of the inserts could be found in the manufacturer manual. According to the CATPhan® phantom, ED had to be determined from CT scans which had been acquired with the chest protocol, after having calibrated the CT using the Gammex® RMI based relationship between HUs and EDs.

In figure (5.1), the HU/ED correlation curves obtained from CT scans of both phantoms are depicted.

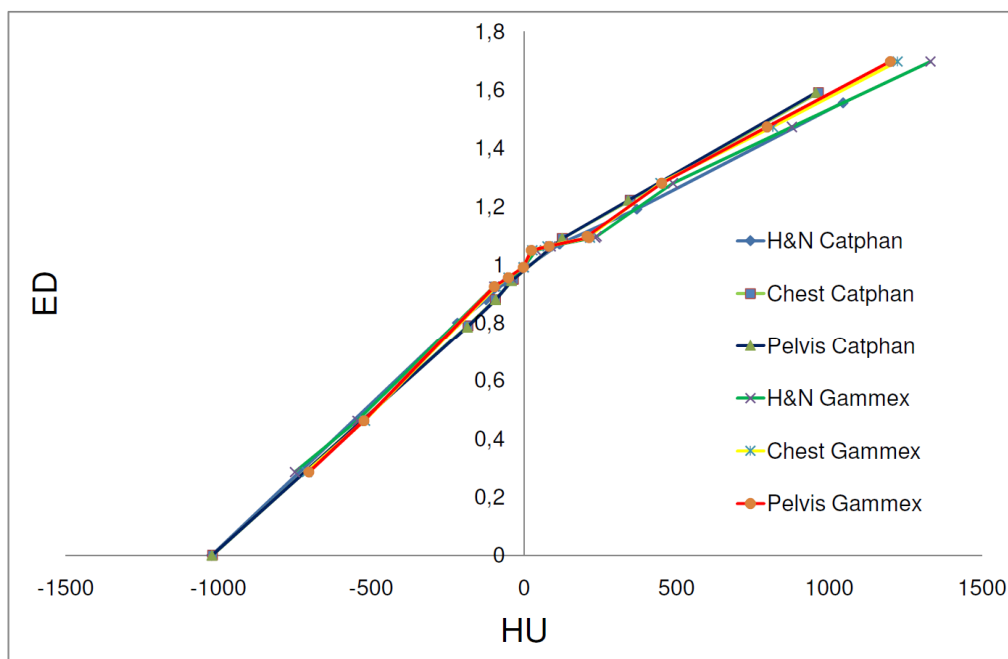


Figure 5.1: HU/ED calibration curves for CT based dose calculation

Just slight discrepancies between the curves were detected. For dose calculation, only correlation curves obtained from the CT scans of the Gammex® RMI phantom were used. This was decided for two reasons. Firstly, the Gammex® RMI phantom is a CT phantom, which is especially designed for ED calibration purposes of CT scanners and therefore, its material inserts correspond to tissue within the human body. In contrast, the CATPhan® phantom is a CT image quality phantom containing tissue substitute materials and hence not designed for ED calibration. Secondly, the Gammex® RMI based correlation curves are quite similar in a big range around ED of water. This is exactly the range we are most interested in and therefore, the CATPhan® phantom was dismissed for CT calibration purposes. If one takes a closer look to the Gammex® RMI phantom based curves, one will detect that the curves for the chest and pelvis presets lied on top of one another. The H&N protocol showed also very good consistency up to EDs of approximately 1.2. The H&N curve deviated up to 4% from the other curves thereafter. Such deviations in ED are clinically negligible for dose calculation and hence the Gammex® RMI chest or pelvis HU/ED curve could be utilized for all dose calculation purposes [30].

In the following figures (figure (5.2) and figure (5.3)), the obtained calibration curves for the CBCT device are shown.

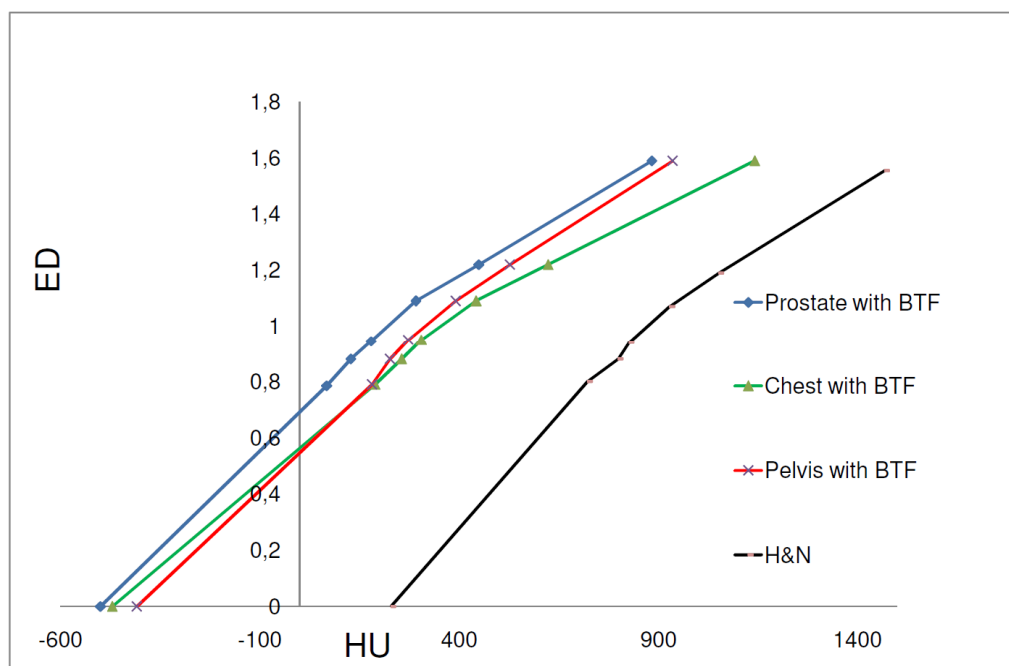


Figure 5.2: CATPhan® based HU/ED calibration curves for CBCT based dose calculation

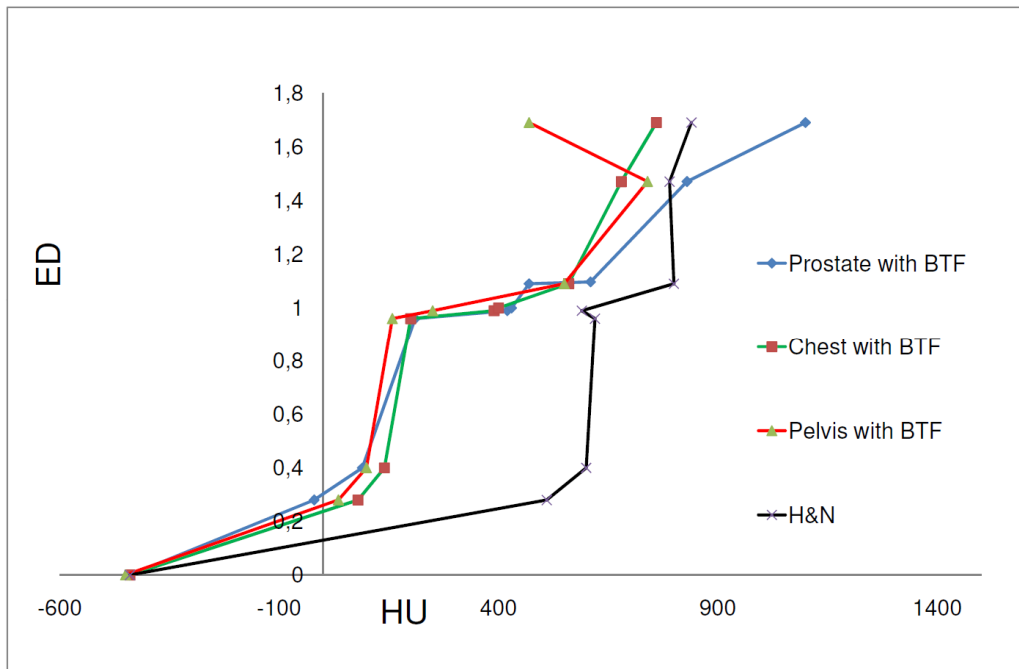


Figure 5.3: HU/ED calibration curves based on Gammex® RMI phantom scans for CBCT based dose calculation

In the case of calibrations curves for CBCT based dose calculations, discrepancies of the curves between each other and the underlying phantoms were extreme. Regarding the CATPhan® phantom based curves (figure (5.2)), one can see almost strict parallel behavior. Different scanning protocols provoked only a zero shift. Moreover, the curves demonstrated a similar run to the desired CT calibration curves. When comparing the experimentally detected EDs from the CBCT datasets to those obtained from CT images, the average deviations is 27%. To demonstrate that, one CATPhan® based curve is shown together with its corresponding CT counterpart in figure (5.4). All curves were fitted bilinearly before being implemented into iPlan® TPS for dose calculation. The linear regression formulas are shown in the following chart for one particular correlation curve (Chest with BTF).

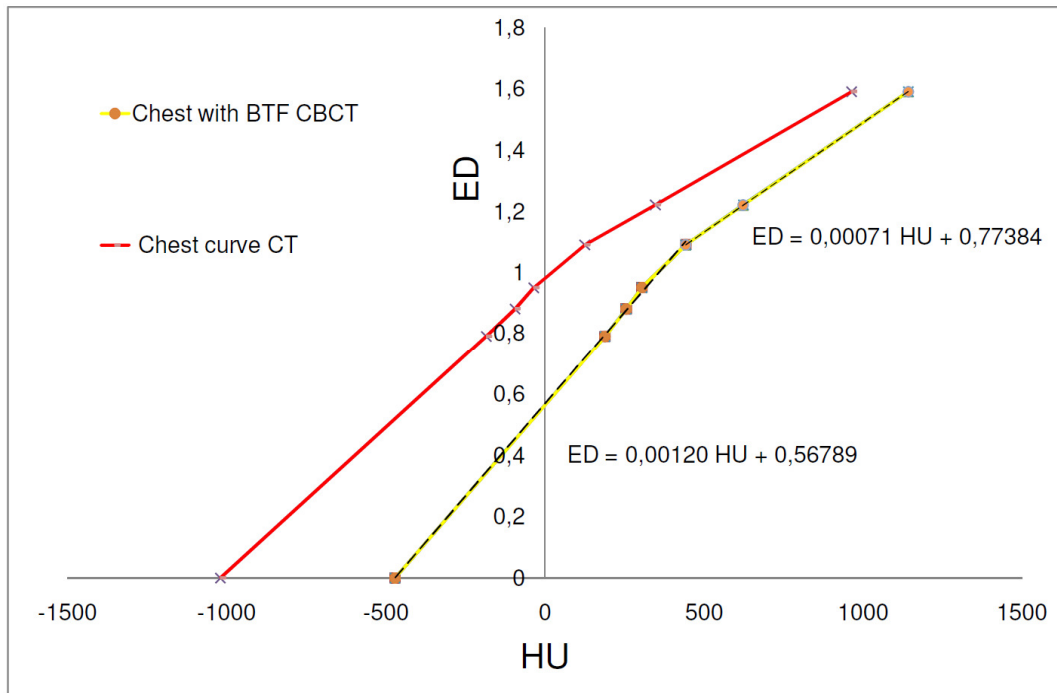


Figure 5.4: Comparison of CBCT Chest curve with BTF to corresponding CT curve

In figure (5.3), HU/ED calibration curves, based on CBCT images, which were obtained by scanning the Gammex® RMI phantom, are depicted. Here, no parallel behavior of the curves is noticeable, in contrast to the CATPhan® counterparts. Even the requirement, that ED should be proportional to the measured HUs, is violated in some cases (e.g. in the case of the H&N curve around the solid water insert). Furthermore, almost no similarities of the curves compared to the CT curves were detectable.

The discrepancies of the curves, obtained from the two phantoms, could be interpreted as follows. The scatter conditions of the two phantoms are totally different. While the CATPhan® phantom is a cylinder with a diameter of 150 mm and a length of 200 mm, the Gammex® RMI phantom consists of a narrow, big and round slice with a diameter of 330 mm and a length of 50 mm. In case of the firstly mentioned phantom, the comprising cylinder filled almost the entire FOV in the isocenter of the CBCT. By this fact, full scatter conditions were guaranteed and hence, tissue within the human body was well simulated. In contrast to this, the single slice of the Gammex® RMI phantom covered only a small fraction of the FOV of the CBCT and therefore, unfavorable scatter conditions were created, which led to image artifacts. Additionally, it came to wide intensity fluctuations across the flat panel detector, which gave additional rise to artifacts.

Several images of both phantoms are shown next. Image quality deficiencies of the CBCT images against CT images can be clearly seen.

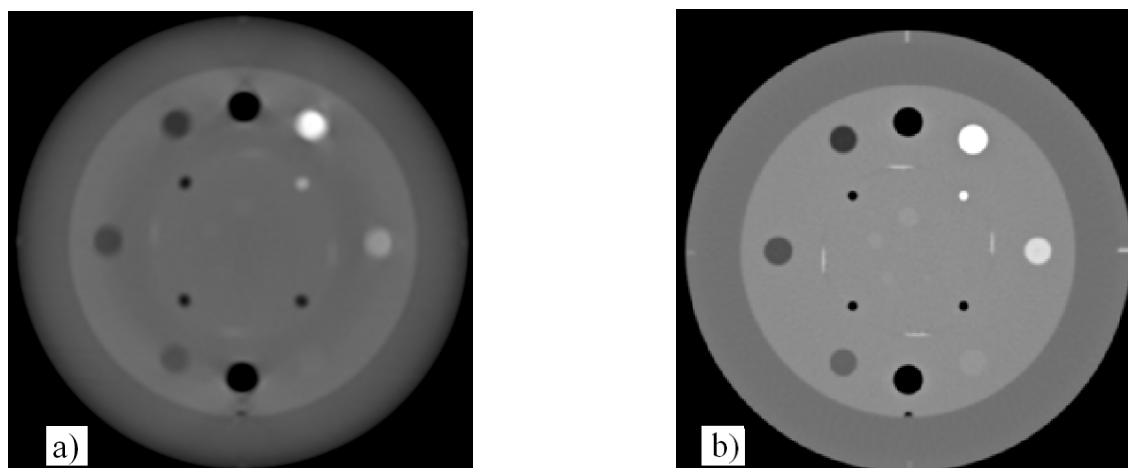


Figure 5.5: Acquired images of the CATPhan® phantom, with a) CBCT (Chest with BTF) and b) CT Chest

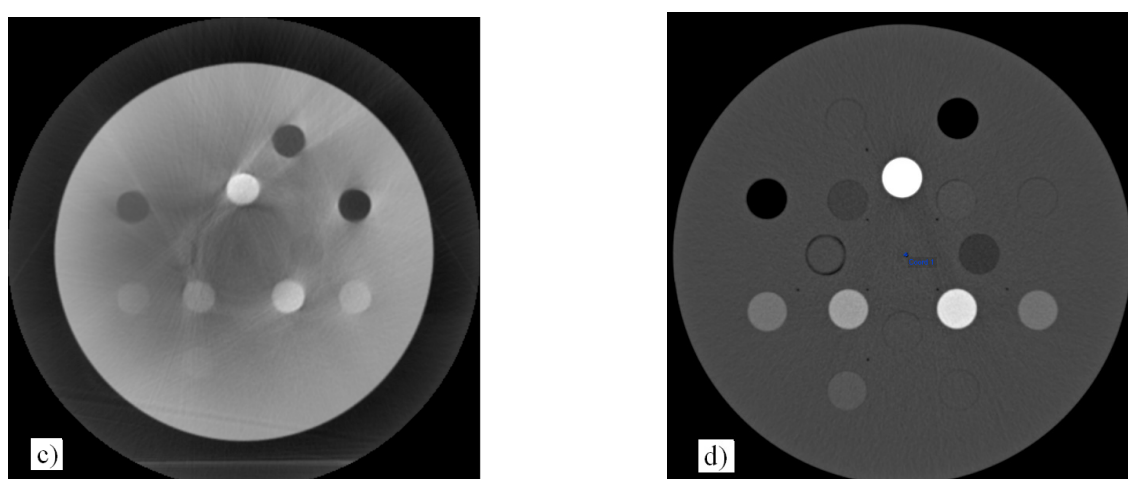


Figure 5.6: Acquired images of the Gammex® RMI phantom, with c) CBCT (Chest with BTF) and d) CT Chest

These 4 images were either acquired with the chest protocol with BTF on CBCT and with the corresponding chest protocol on CT. For dose calculation, based on CBCT data sets, it was decided to rely on the HU/ED calibration curves based on the CATPhan® phantom, for the above stated reasons. In order to have an appropriate HU/ED correlation for each protocol, all obtained CBCT curves were imported into iPlan®. For the further dose calculation and comparison in the context of this study,

the chest curve obtained with BTF (figure (5.4)) was used, because it represents the most frequently used clinical protocol.

5.3.1 Scanning parameter dependency

The fact that the obtained HUs of the CBCT images varied strongly with the settings of the image acquisition parameters was clearly visible in figure (5.2) and figure (5.3). The curves, which were obtained from scanning the CATPhan® phantom, were analyzed in more detail. In the following chart (figure (5.7)), the mean values of HUs, detected in the various inserts, are plotted with respect to the corresponding materials.

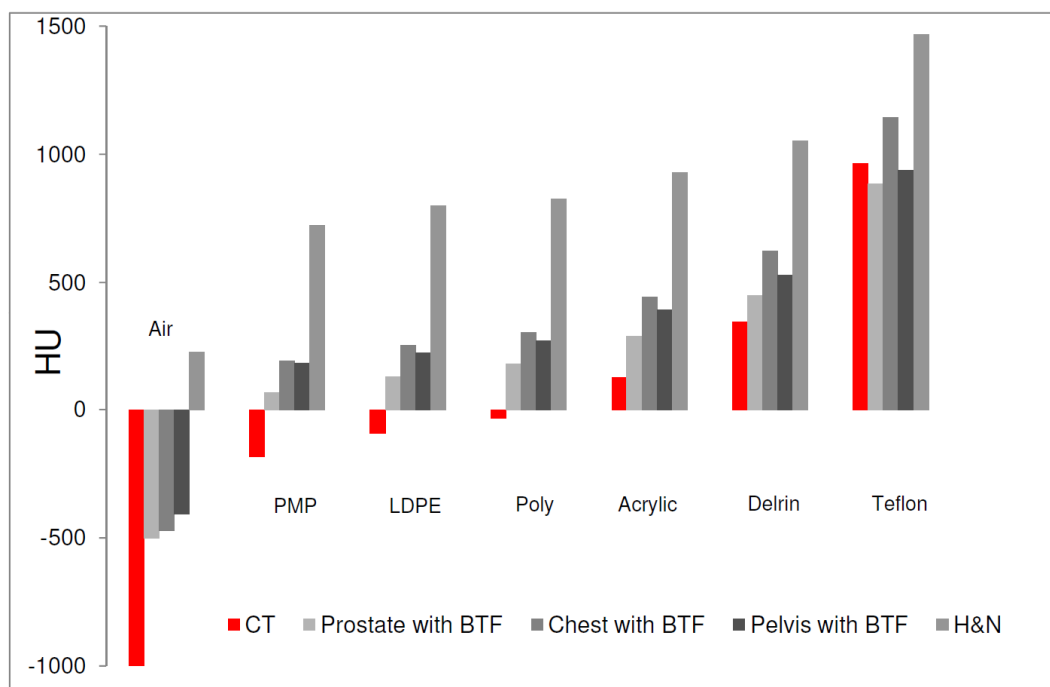


Figure 5.7: Parameter settings dependency of obtained HU

Vast variations of HUs, caused by different parameter settings could be detected. When bearing in mind that tube voltage was variable and mAs settings varied between 30 mAs up to 1000 mAs, this result is obvious. The mean values of HU in the air insert vary most. In this case, the standard deviation was ± 339 HU. Going towards denser materials, variation decreased quickly and reached a minimum value

of ± 184 HU in the Teflon insert. For protocols without BTF, tendentially even higher HUs can be expected, although such cases are not shown in figure (5.7). Once again, due to the cone shaped beam in CBCT, scatter effects posed a severe problem, when comparing image quality to CT. Huge deviations in HUs of all curves, according values obtained from CT, were discernable. Mean values in CT images are also displayed in the chart above.

5.3.2 Temporal stability

Another task, which was of interest in the framework of this study, was the determination of temporal stability of the CBCT correlation curves. For this purpose, one protocol, namely the '*image quality*' protocol, was used as a representative protocol. If temporal stability was confirmed in this case, no time trend could be assumed for the other curves as well. The reason for performing the test on this special protocol was that various data sets were already available. The temporal stability tests were carried out on CBCT images of the CATPhan® phantom, which were already utilized for QA purposes of the CBCT device (chapter 3). In the course of the QA procedure, images of the phantom were acquired over a period of 10 months. In the software environment of the TPS, the 7 material inserts were delineated in several slices and again, average HUs and their deviations were recorded in all images. In the following chart (figure (5.8)), the results of the evaluation of the temporal stability are shown.

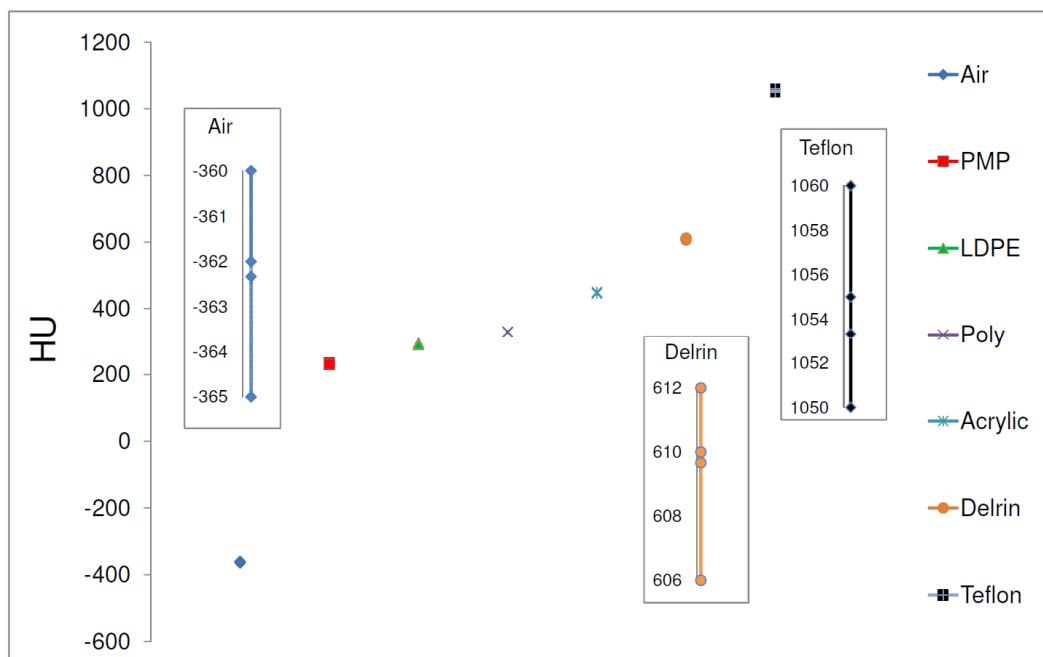


Figure 5.8: Temporal stability of the HU. Spots representing a series of individual monthly samples, depicted in some cases by the widened scale.

In the diagram above, the values of the HUs for the evaluation period are plotted as a function of material inserts. A small variation of HUs around the appropriate mean value of several HUs was detected. The multiple ordinates in the chart represent a widened scale of the principal ordinate. Onto these axes, the mean values of HUs, obtained from the single monthly samples, are depicted for three examples, air, delrin and Teflon. Otherwise, the very small variations would graphically not be resolvable. In table (5.1), the maximum deviations are listed.

Temporal stability of HUs within 10 month

Material insert	Air	PMP	LDPE	Polystyrene	Acrylic	Delrin	Teflon
Mean value [HU]	-362	230	290	328	446	609	1053
Standard deviation [HU]	2	2	2	1	2	2	5
Maximal deviation [HU]	22	24	24	20	24	26	30

Table 5.1: Results of stability test of HU/ED curves

Regarding the results, HU/ED correlation curves can be considered to be temporally stable. With the previous determinations, the basis for dose calculation with iPlan® was provided.

5.4 Dose differences due to curve exchange

In this section, dose differences, arising from the application of different HU/ED calibration curves, should be characterized qualitatively and quantitatively. For this purpose, one single CBCT image of the in-house pelvis phantom (figure (2.14)) was acquired. The data set was loaded into iPlan® and the automatically created outer contour was adjusted as accurate as possible. This was necessary, because the autocontouring algorithm utilizes a certain threshold HU value to identify contours. Thus, an accurate segmentation of the phantom was not automatically achievable due to the presence of image artifacts in the CBCT image. Three materials, such as water, lung tissue and cortical bone with relative ED of 1, 2.28 and 1.47, respectively, were used as sample materials in order to determine dose differences. With the recently established correlation curves it was calculated, which HUs correspond to the requested EDs in each protocol. By the use of a special tool in iPlan® it was possible to assign certain HUs to delineated structures. Therefore, the appropriate HUs characterizing above stated materials were assigned to the outer contour. This was done in order to simulate the pelvis phantom to be constructed of one of the three materials and imaged by the use of a certain protocol.

Subsequently, a point of interest was set in a depth of 100 mm under the segmented surface of the phantom in the CBCT image. Around this point of interest, a fictive spherical PTV was contoured, to which a dose of 2 Gray (Gy) should be delivered. By a successive application of the various HU/ED calibration curves, the MUs to fulfill the above mentioned dose prescription, were compared. The results of these tests are shown in the following chart.

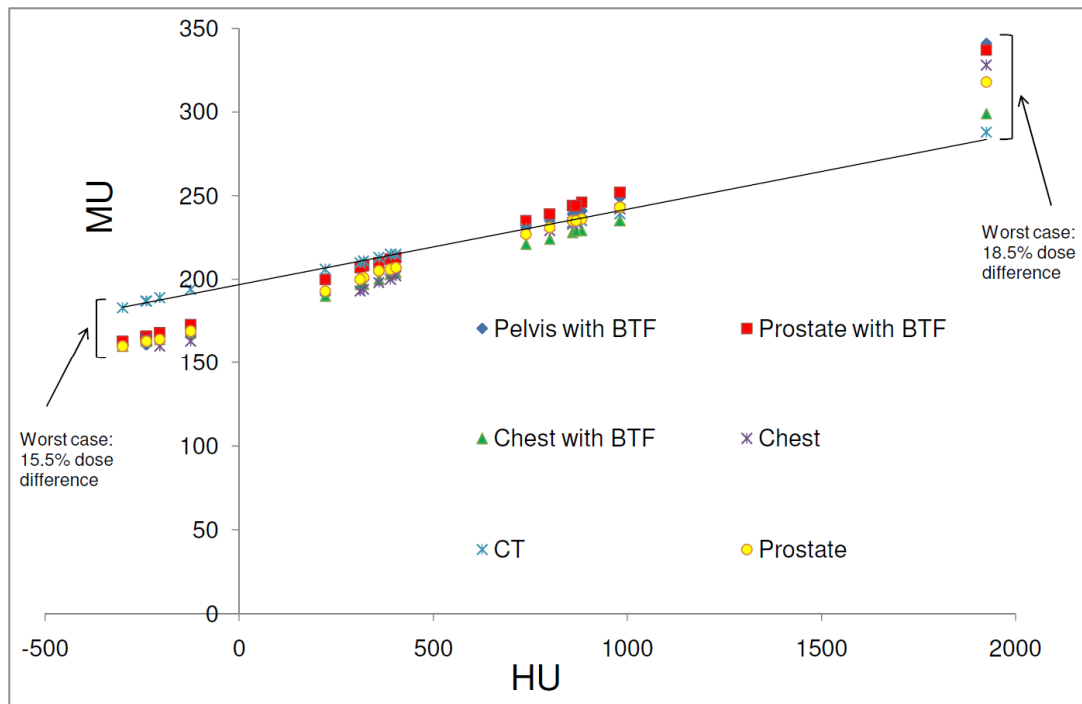


Figure 5.9: Dose differences due to application of different calibration curves

It was most obvious, that the slope of the curve, obtained from CT, was significantly flatter than of those from CBCT. The CT sample points were fitted for a better graphical illustration. In any case, the CT HU/ED calibration curve cannot be utilized for dose calculation based on CBCT images. This would vastly exceed the clinical tolerances of dose accuracy. Towards the lower part of the graphs, a worst case scenario, which led to a dose difference of 15%, is highlighted. In the upper region of HUs, the possible dose differences were even more significant. As a worst case scenario, the dose difference based on application of the CT curve and the Pelvis curve with BTF is marked. Dose difference of 18.5% could occur due to an accidental application of non adequate calibration curves. For the classification of all maximum dose deviations in the three inserts, which can occur in case of misapplication of calibration curves, figure (5.10), was generated. In this plot, all maximum dose differences were depicted as a function of HUs, which represent the material inserts water, lung tissue and cortical bone. In figure (5.10), each differently colored area highlights one material insert. Lung tissue is represented by the yellow, water by the blue and cortical bone by the green shaded area. Because the H&N correlation curve is located far away of the other curves (see figure (5.2)), the corresponding HUs were shifted to the right and consequently didn't lie within the respective areas.

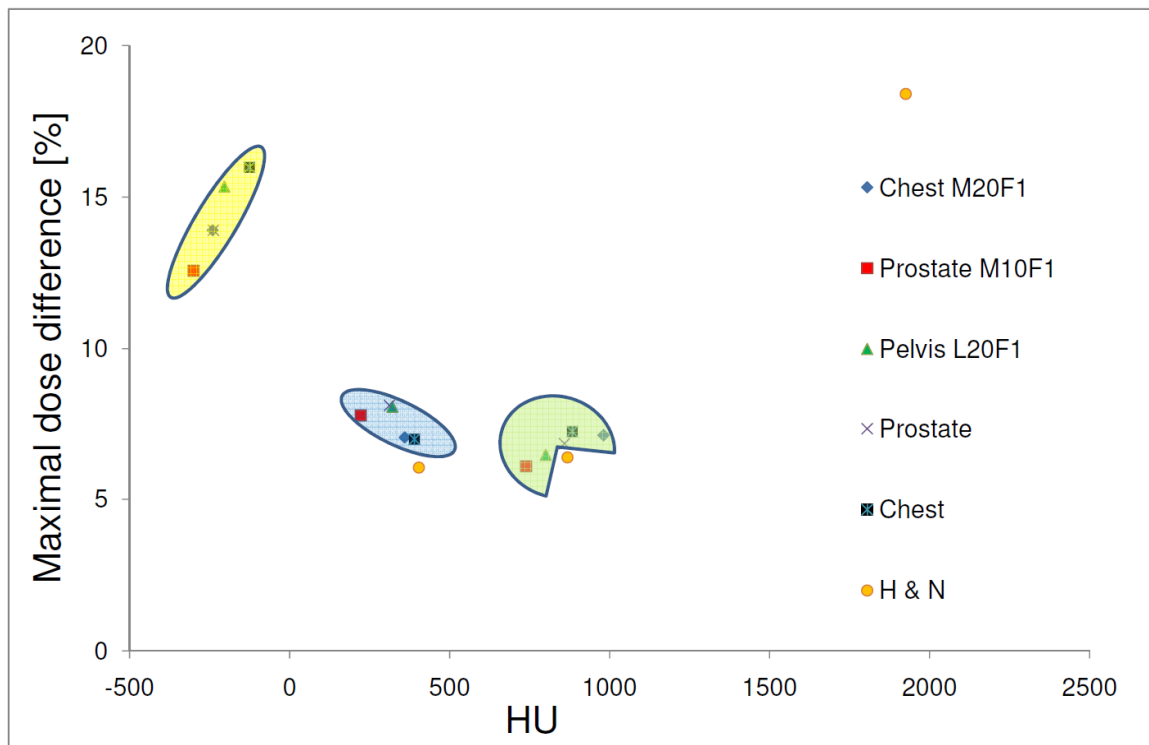


Figure 5.10: Maximum possible dose difference of respective material inserts

5.5 Dose comparison

5.5.1 Preparation and method

In this section, the feasibility of dose calculation based on CBCT data sets was evaluated. For setting ART into clinical routine, physicists as well as physicians have to be aware and confident of its accuracy.

The inhomogeneous slab phantom, which was described in section (2.5.4.2), was scanned twice for this purpose, with the CT and with the CBCT, respectively. For the CBCT image, the clinical chest protocol with bow tie filter was used, as it is the most frequently used in clinical practice. For the image acquisition with the CT, the appropriate chest protocol was applied. The following figures show the images of the slab phantom, obtained from CT (figure (5.11)) and CBCT (figure (5.12)).

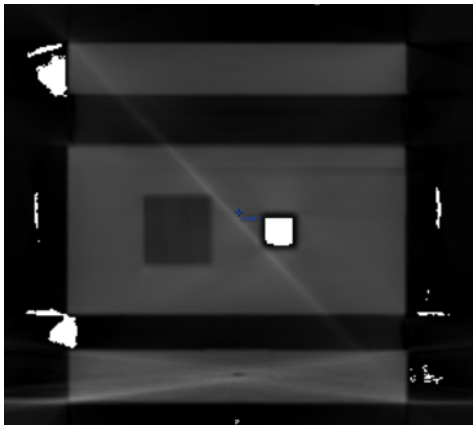


Figure 5.11: CBCT image of the slab phantom

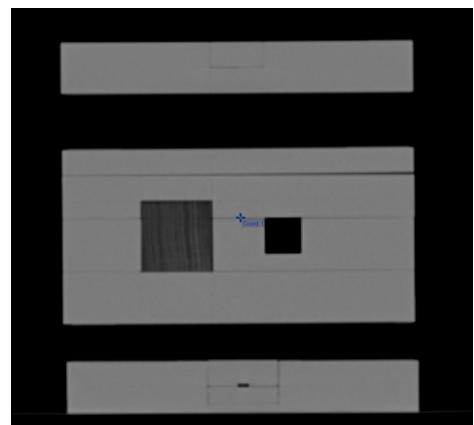


Figure 5.12: CT image of the slab phantom

In figure (5.11), several streak artifacts are visible, the most obvious one diagonal through the phantom. The white spots in the center and at the edges of the phantom were caused by the transformation of CT numbers in the CBCT software to HUs in the TPS software. By this reconfiguration, certain CT numbers slide out from the lower range of the HU scale and appear on its upper edge. Consequently, low density materials seem to be extremely dense. In figure (5.11), the central spot depicts the air channel, which traverses the polystyrene plates. It caused a huge

artifact and hence it was contoured and the HUs of air were assigned. The CT image was almost artifact free and thus optimal for planning purposes.

After image acquisition, the images were imported into the TPS and in its software environment a virtual PTV was created at a depth of 100 mm, which corresponded to the isocenter of the linac. Two Gray should be delivered to this volume by the application of an isocentric 64 x 64 mm² field of an AP field. This was carried out for 6 MV, 10 MV and 18 MV, respectively.

For illustration purposes, a screenshot of the planning step is shown in figure (5.13). On the upper right side, the beams eye view with the applied field is depicted, which is formed by the MLC. One level below, one can see the transverse slice with the isodose distributions. On its left, an orientation sight representation is visible in order to visualize the direction of the incident beam, is visible.

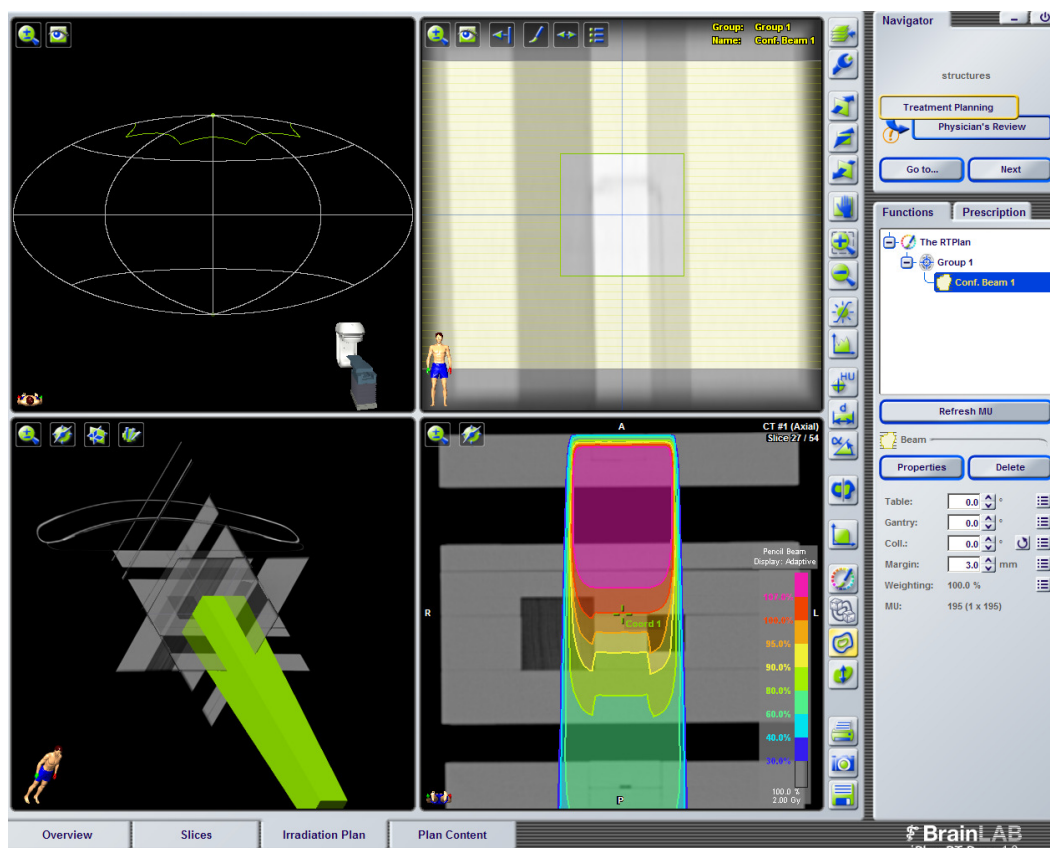


Figure 5.13: Screenshot of the planning procedure in iPlan®

Afterwards, the TPS was utilized to calculate the dose distributions, based on CT and on CBCT images. Depth dose curves as well as lateral dose profiles were extracted and compared to each other. This was done by applying a Gamma evaluation with a

dose variation criterion of 2% and 3% and a DTA of 2 mm and 3 mm for PBA and MCA, respectively. The results of this comparison are illustrated in the next paragraph.

5.5.2 Results

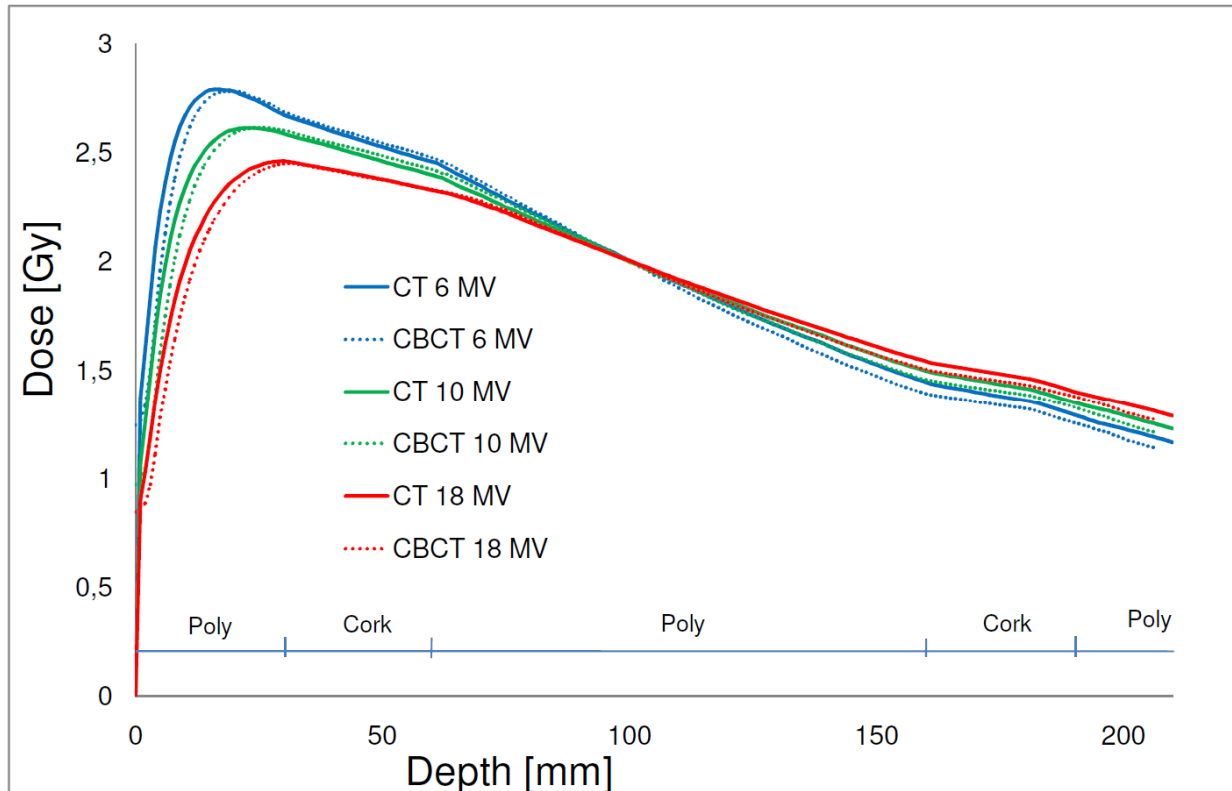


Figure 5.14: Depth dose comparison with PBA (CT vs. CBCT)

In the chart above, depth dose curves for all considered energies, obtained from CT- and CBCT based dose calculations, are shown. Hereby, the pencil beam dose calculation algorithm was used. An underestimation of the dose in the dose build up region regarding CBCT planning was evident in all cases. This was maybe caused by a significant reduction of the outer contour of the phantom in the CBCT image due to cupping artifacts. Phantoms material is subsequently forced to appear less dense in the outer regions and hence dose was underestimated. When cupping artifacts vanished towards d_{\max} , differences were less apparent until a depth of approximately 100 mm. From this point on, dose differences increased again. This might be explained by the location of the air channel, traversing the phantom. This long air

insert was located exactly at this depth and gave rise to a disastrous image artifact, as mentioned in the paragraph above. Due to radiation shielding effects, matter below appeared to be less dense again. In the following figure, the subsequent Gamma evaluation is illustrated using the example of a 6 MV beam. In the upper region of the chart, the depth dose curves are shown once again. In the lower area, the Gamma curve is outlined, which illustrates the clinical acceptance criteria,. The figure also contains information of the depths, where the various material slabs were located. Thereafter, a table comprising significant Gamma indexes characterizing dose comparisons for all energies, i.e. mean values and maximum value, is shown.

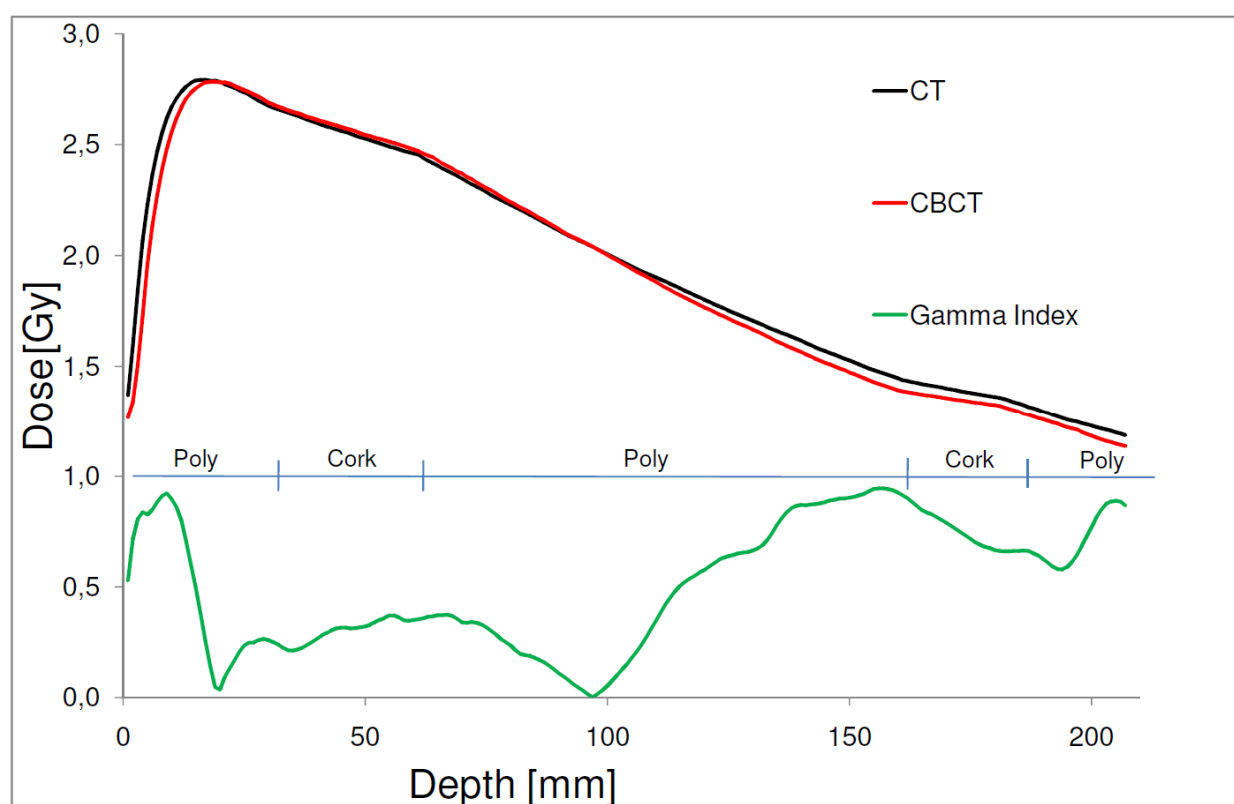


Figure 5.15: Gamma evaluation of 6 MV depth dose distributions with PBA

Representative Gamma Indexes of PDD comparisons

	6 MV	10 MV	18 MV
γ -mean	0.51	0.47	0.44
γ -max	0.94	0.87	0.93

Table 5.2: Results of the Gamma evaluation of dose comparison with PBA (CT vs. CBCT)

The same procedure as for depths dose curves was carried out for dose profiles as well. For the dose profile comparison, a lateral dose profile at the depth where the isocenter was located was extracted. In figure (5.16), the resulting plot for the 6 MV profile and the performed Gamma evaluation are depicted.

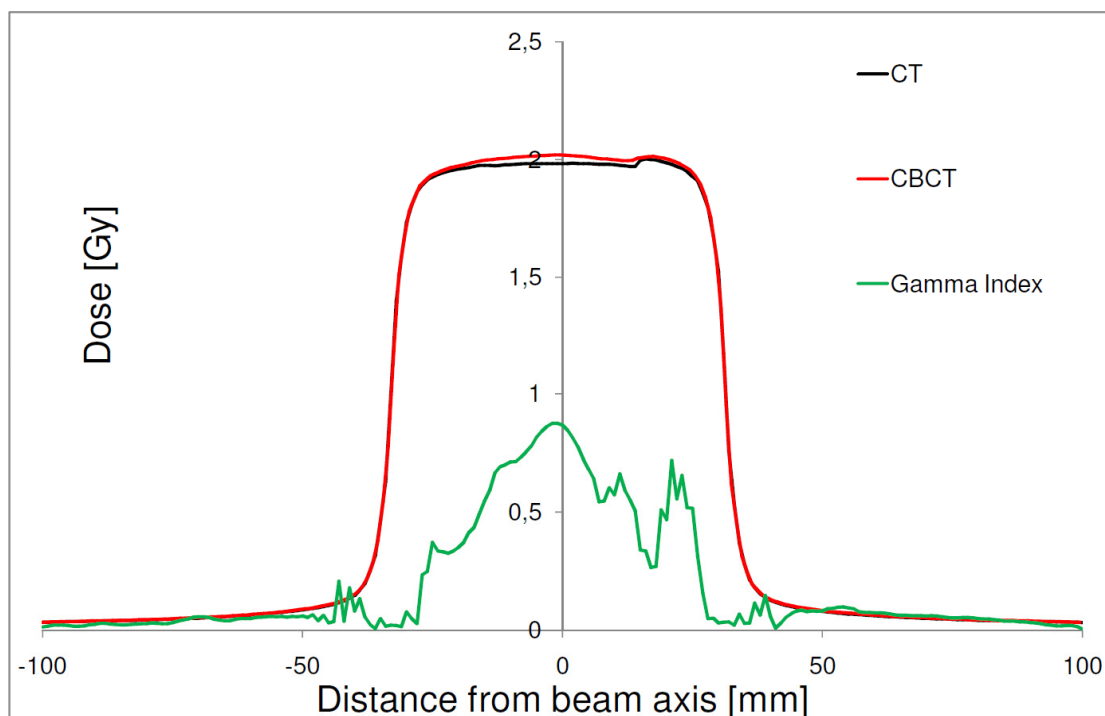


Figure 5.16: Gamma evaluation for a representative 6 MV dose profile with PBA (CT vs. CBCT)

Subsequently, the representative Gamma Indexes are listed for all energies.

*Representative Gamma Indexes of lateral dose profile comparisons in
100 mm depth (PBA)*

	<i>6 MV</i>	<i>10 MV</i>	<i>18 MV</i>
<i>γ-mean</i>	0.24	0.01	0.11
<i>γ-max</i>	0.87	0.38	0.56

Table 5.3: Results of the Gamma evaluation of dose profile comparison in the isocenter, calculated by PBA (CT vs. CBCT)

Obviously, even with very severe acceptance criteria, the Gamma Indexes never exceeded 1. This was the condition for a possible implementation into clinical use. Additionally, the same procedure was repeated for the MCA. Here, the acceptance criteria were increased to 3% dose variation and 3 mm DTA. This was done because larger deviations of PDDs and dose profiles were determined, due to larger statistical variances. Consequently, with the previously used Gamma criteria of 2% and 2 mm, the dimensions of the Gamma Indexes increased substantially. In figure (5.17), the results of PDD comparisons for MC case are depicted. Using the example of the 6 MV beam, the respective Gamma evaluation is shown thereafter, followed by table (5.4), where representative Gamma Indexes for all energies are listed.

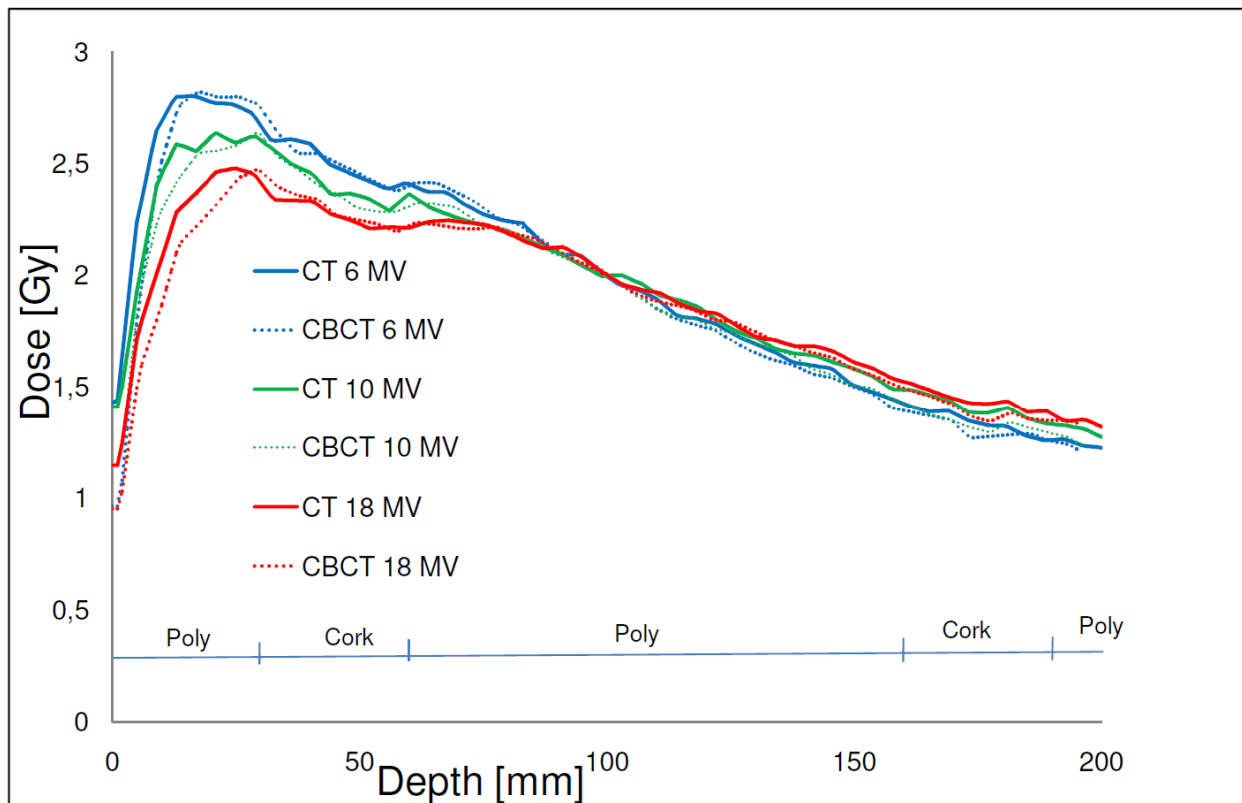


Figure 5.17: Depth dose comparison with MCA (CT vs. CBCT)

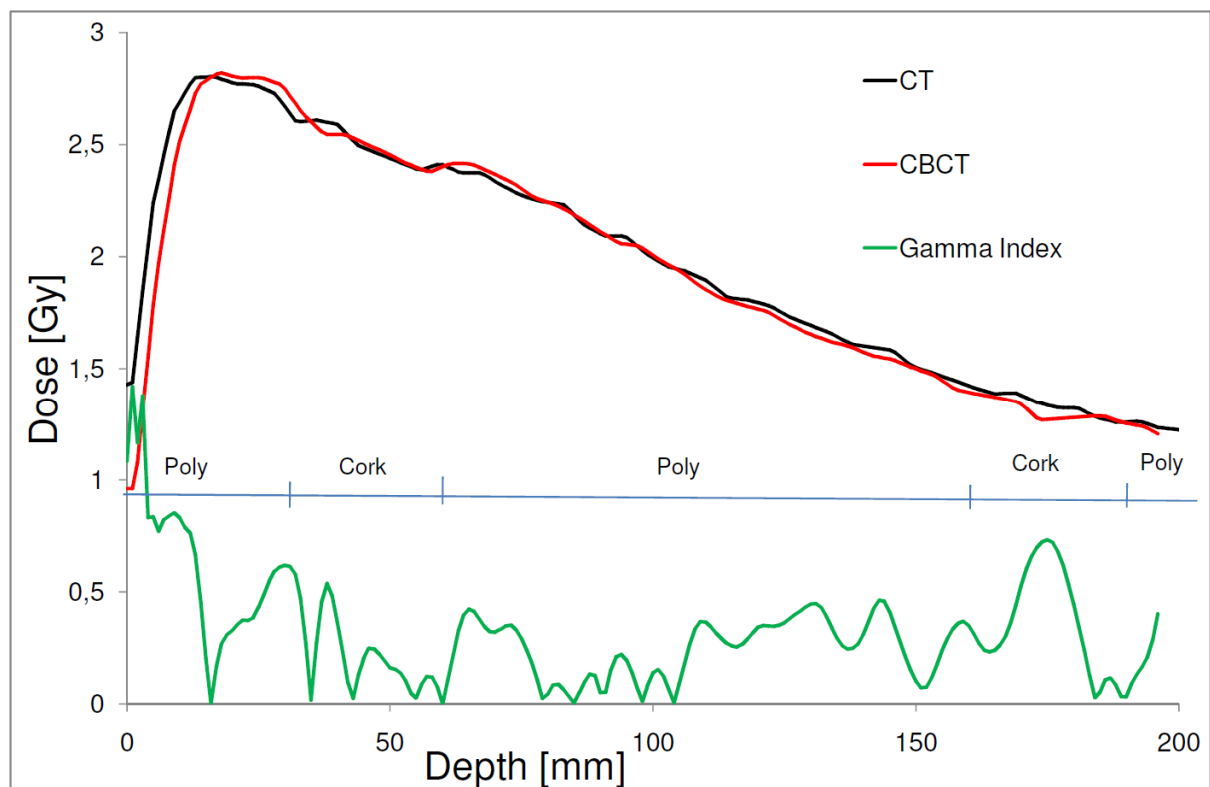


Figure 5.18: Gamma evaluation of 6 MV dose profile with MCA

Representative Gamma Indexes of PDD comparison

	<i>6 MV</i>	<i>10 MV</i>	<i>18 MV</i>
<i>γ-mean</i>	0.32	0.70	0.58
<i>γ-max</i>	1.41	1.87	2.19

Table 5.4: Results of the Gamma evaluation of PDD comparison with PBA (CT vs. CBCT)

Lateral dose profiles were also extracted from the TPS for MCA comparison purposes. The result is illustrated in figure (5.19) for 6 MV dose profiles at 100 mm depth as an example.

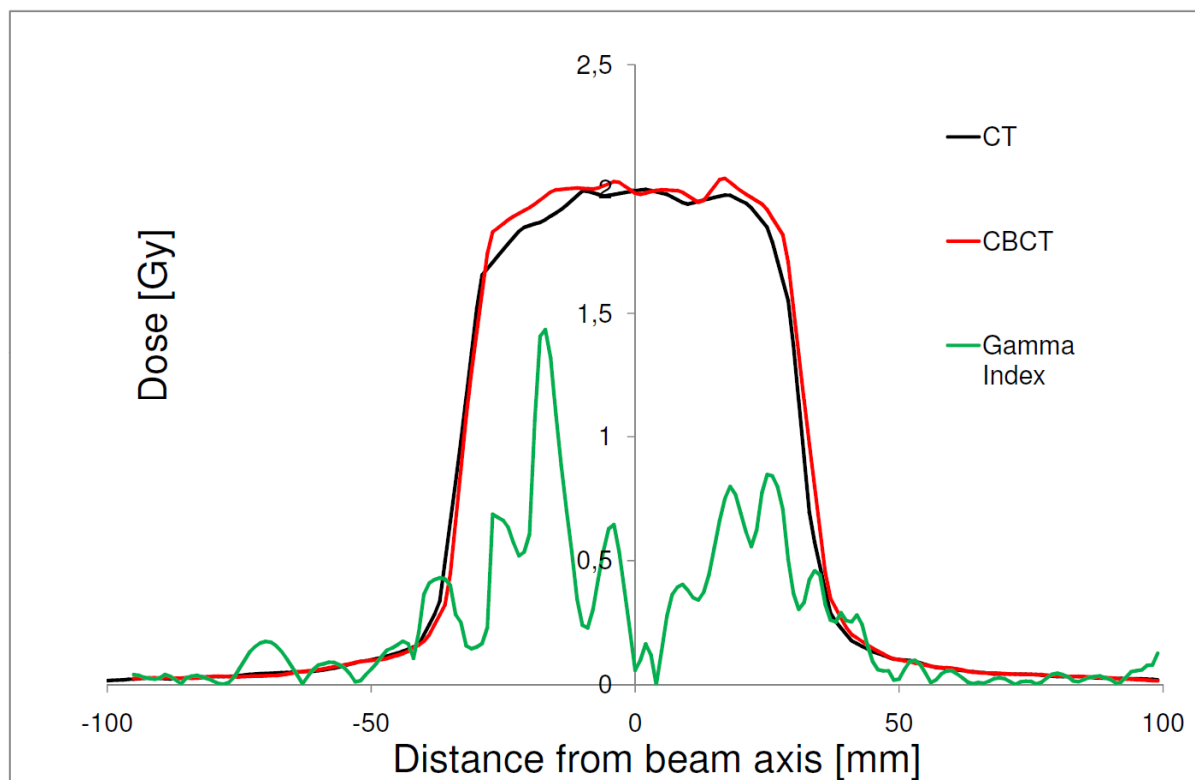


Figure 5.19: Gamma evaluation for a representative 6 MV dose profile with MCA (CT vs. CBCT)

As expected for the results of the dose distributions calculated by the MCA, Gamma Indexes were much larger compared to PBA. Because most of the evaluation points passed a Gamma evaluation with less severe acceptance criteria compared to PBA, MCA can be considered as clinically applicable as well. In table (5.5), the usual Gamma Indexes for lateral dose profiles of all energies are listed.

Representative Gamma Indexes for lateral dose profiles in 100 mm depth
(MCA)

	<i>6 MV</i>	<i>10 MV</i>	<i>18 MV</i>
<i>γ-mean</i>	0.24	0.23	0.28
<i>γ-max</i>	1.44	1.57	1.50

Table 5.5: Results of the Gamma evaluation of dose profile comparison in the isocenter, calculated by MCA (CT vs. CBCT)

6 Summary and outlook

In the context of this study, various aspects influencing the performance of CBCT as a major tool for ART were investigated.

Except for the MTF measurements, none of the evaluated image quality as well as registration accuracy parameters showed a time trend over the investigation period. MTF was found to deteriorate with time. This has still to be examined in more detail. By conduction of a gain calibration procedure, MTF could immediately be reset to a better behavior. Hence, frequent gain calibration is recommended on a quarterly basis. Generally, it can be stated that all of the checks, MTF excluded, met the specifications of the CAT. The used '*Image Quality*' protocol, which is especially designed for IQ purposes, uses a special reconstruction algorithm with a very high resolution and high mAs settings. It is not used in clinical practice and therefore it can not represent the full range of clinical routine protocols. At least it is an indicator for detection of most of the known errors in CBCT technology.

Because CBCT is a relatively new imaging device, data on the number of parameters in the QA process and the experience of performing these tests are limited. Some of the performed checks were based on the customer acceptance test, suggested by Elekta, and on the diploma thesis of Mag. Marlies Pasler, who performed pilot runs of QA processes on the same device in 2007/2008. In our case, all achieved results were comparable to the results of the investigation mentioned above including a longer total observation period.

Generally, the results of the IQ test procedure, obtained in the frame of this study in combination with the findings of Ms. Pasler, showed accurate performance for various purposes of ART, i.e. detection of patient positioning errors as well as CBCT based dose calculation.

This work also aimed at commissioning of the TPS iPlan® of BrainLAB. The acquisition of the basic beam data sets, required by this TPS as well as their implementation and acceptance, was successfully performed. From several Gamma

evaluations it was visible that the largest dose differences occurred in steep dose gradient regions.

Furthermore, the usability of CBCT images for ART was investigated in first steps. It was obtained that the performance of the various protocols was highly dependent on parameter settings, such as kV and mAs settings, filtering and collimation. Large deviations of HUs between the pCT- and the CBCT images were detected. The results and the deviations were comparable to Richter et al. [27], who carried out a similar calibration procedure. Consequently, the application of a HU/ED correlation curve, based on CT images, would lead to clinically not acceptable dose differences, when applied to CBCT data sets. Due to additional high discrepancies in HUs of the CBCT protocols among each other, several correlation curves were requested, in order to provide a proper relationship between HUs and EDs for the respective protocols.

Dose calculation, based on CBCT images, was performed and compared to CT based dose calculation. Dose calculations were carried out on images acquired from a in-house developed slab phantom, consisting of alternating material plates, in order to simulate an inhomogeneous human body. The calibration curve of the chest protocol, obtained with BTF was applied for this purpose. By the application of this HU/ED correlation curve, dose calculation resulted in small errors, compared to CT.

The results of this work showed that under certain conditions, dose calculation based on CBCT data sets, is feasible. However, one has to take into account image artifacts, which make a severe impact on dose calculation. This problem may be bypassed through better reconstruction algorithms that trace image artifacts already in frequency space and subsequently correct for them.

Another supporting way to handle imaging errors better may be the use of so called autosegmentation tools. Hereby, specific HUs might be assigned to certain volumes, perturbed by artifacts. This should be investigated in more detail.

Further studies, which should reveal dosimetric advantages of ART, are planned for the future. Potential areas of interest concerning CRT and IMRT applications are H&N- and pelvis area (prostate and rectum).

Bibliography

- [1] J. Bissonnette, D. Moseley, E. White. Quality Assurance for the geometric accuracy of Cone-Beam CT guidance in Radiation Therapy. *Int. J. Radiation Oncology Biol. Phys.*, 71(1) pp. 575 - 561, 2008
- [2] M. Pasler. Quality Assurance and Radiation Protection Aspects of IGRT. Diploma Thesis. Medical University of Vienna
- [3] B. Knäusl. Dosimetric Characteristics of a Flattening Filter Free Photon Beam. Diploma Thesis. Medical University of Vienna
- [4] B. Curran, J. Balter, I. Chetty. Integrating New Technologies into the Clinic: Monte Carlo and Image Guided Radiation Therapy. Medical Physics Publishing, Wisconsin/Medical Physics Monograph No. 32
- [5] H. Krieger, Petzold. *Strahlenphysik, Dosimetrie und Strahlenschutz* Bd.1 Grundlagen. B.G.Teubner Stuttgart, 1992
- [6] F. M. Khan. *The Physics of Radiation Therapy*. Lippcott Williams & Wilkins, Third edition, 2003
- [7] J. Van Dyk. *The Modern Technology of Radiation Oncology*. Medical Physics Publishing, Wisconsin
- [8] International Commission on Radiation Units. ICRU Report 50. Prescribing, Recording and Reporting Photon Beam Therapy. ICRU, 1993
- [9] D. Jaffray, J. Siewerdsen. Cone-Beam computed tomography with a flat panel Imager: Initial performance characterization. *Med. Phys.* 27 (6), June 2000

- [10] M. Sakakimoto, N. Nishiyama, H. Satoh. An implementation of a feldkamp algorithm for medical imaging on cell. IBM Corporations, System and Technology group, 2005
- [11] L. Feldkamp, L. Davis, J. Kress. Practical cone beam algorithm. Journal of the Optical Society of America, A1: pp. 612 – 619, 1984
- [12] Elekta Limited. Clinical User Manual for XVI R4.0, 2006
- [13] www.optoelectronics.perkinelmer.com
- [14] P. Roberts, V. Hansen, A. Niven. A low Z linac and flat panel imager: Comparison with the conventional imaging approach. Phys. Med. Biol. 53, pp. 6305 – 6319, 2008
- [15] P. Mayles, A. Nahum, J. Rosenwald. Handbook of Radiotherapy Physics. Taylor and Francis Group, LLC, 2007.
- [16] www.stratecservices.nl/images/products/Blue_Phantom.pdf
- [17] Leeds Test Object. TOR 18 fg. Routine Test Objects, X-Ray Phantoms Handbook
- [18] D. Goodenough. Catphan® 500 and 600 Manual. The phantom laboratory, Incorporated, Salem, NY 12865 – 0511, 2006
- [19] Gammex Handbook, Manual 467 Users Guide
- [20] Elekta Limited. Customer Acceptance Tests for XVI R.4, 2006
- [21] International Electrotechnical Commission. Evaluation and routine testing in medical imaging departments. IEC 61223 – 3 – 5, 2004

- [22] T. Sterling, H. Perry, I. Katz. Deviation of a mathematical expression for the PDD of Cobalt-60 beams and visualization of multiple field dose distribution. *The British Journal of Radiology*, 37: 544, 1964
- [23] Working Instruction. Beam Measurement Pencil Beam (Elekta Beam Modulator) WOI 10 – 138 – 03
- [24] International Commission on Radiation Units. ICRU Report 62. Prescribing, Recording and Reporting Photon Beam Therapy (Supplement to ICRU Report 50). ICRU, 1999
- [25] D. Low, W. Harms, S. Mutic. A technique for the quantitative evaluation of dose calculations. *Med. Phys.* 25 (5), pp. 656 -. 661, 1998
- [26] W. Harms, D. Low, J. Wong. A software tool for the quantitative evaluation of 3D Dose calculation algorithms. *Med. Phys.* 25 (10), pp. 1830 – 1836, 1998
- [27] A. Richter, Q. Hu, D. Steglich. Investigation of the usability of cone beam CT data sets for dose calculation. *Radiation Oncology* 3 (42), 2008
- [28] S. Yoo, F.F. Yin. Dosimetric feasibility of cone beam CT- based treatment planning. *Int. J. Radiation Oncology Biol. Phys.*, 66 (5), pp. 1533 – 1561, 2006
- [29] J. Barker, A. Garden, K. Ang. Quantification of volumetric and geometric changes occurring during fractionated Radiotherapy for Head – and – Neck cancer using an integrated CT/Linear accelerator system. *Int. J. Radiation Oncology Biol. Phys.*, 59 (4), pp. 960 – 970, 2004
- [30] S. Thomas. Relative electron density calibration of CT Scanners for Radiotherapy treatment planning. *The British Journal of Radiology*, 72, pp. 781- 786, 1999
- [31] IAEA TRS – 398. Absorbed Dose Determination in External Radiotherapy, 2004

Abstract

Background

Cone Beam Computed Tomography (CBCT), integrated to the medical linac, is currently utilized for correction of patient positioning uncertainties. Additional possible applications of these image data sets are conceivable for Adaptive Radiation Therapy (ART). By repetitive imaging, one can react on anatomical changes in the patient (e.g. by the adaptation of the irradiation plan) and hence a more sparing therapy can be achieved. In the actual study should be investigated in early steps to what extent CBCT images are feasible for treatment planning purposes in ART.

Materials and Methods

All evaluations were done with the CBCT device integrated to the *Elekta Synergy®* linac at the Department of Radiotherapy at the Medical University of Vienna/AKH Vienna. The images, which were used for dose comparison studies, were acquired with a conventional multi slice CT scanner of Siemens (*Siemens VolumeZoom*). For two calibration phantoms (CATPhan® and Gammex® RMI), the average Hounsfield Units (HU) were detected in various material inserts in CT and in CBCT images. Furthermore, the dependency of HU values on image acquisition parameters (tube voltage, mAs, filtering and collimation) was evaluated and HU/ED (Electron Density) correlation curves of various clinical protocols were established. In the course of an extensive Quality Assurance (QA) process of the CBCT device, representative Image Quality (IQ) parameters were observed and the calibration curves were tested concerning their long-term stability. Subsequently, dose variations, compared to the planning CT, were calculated for an Anterior – Posterior (AP) treatment plan with the Treatment Planning System (TPS) iPlan® of BrainLAB. For commissioning of iPlan®, basic beam data sets had been acquired and implemented. For the determination of dose calculation accuracy, a gamma evaluation was applied. The gamma evaluation was performed on data sets of an inhomogeneous multipurpose phantom with polystyrene as well as cork inserts.

Results

Generally, IQ parameters in CBCT images were demonstrated to be accurate enough for a possible implementation for ART. In comparison to the CT, the experimentally determined CBCT HU/ED correlation curves of both calibration phantoms showed average deviations of 27% in ED. In contrast to the Gammex® RMI based correlation curves, the CATPhan® curves exhibited parallel behavior among each other and obvious similarities to the desired CT correlation curves. Thus, they were applied for dose calculation based on CBCT images. The requirement of temporal stability could be satisfied for one image protocol (*Image Quality* protocol). Over the investigation period of 10 month, maximum deviations of 30 HU around the actual mean values of the inserts in the CATPhan® phantom could be determined. A comparison of depth dose curves between CBCT- and CT based dose calculation, relying on the Pencil Beam Algorithm (PBA), showed mean Gamma Indexes up to 0.51 and maximum values of 0.94. For dose profile comparison, 0.24 and 0.874 was found for mean and maximum Gamma Indexes, respectively. An underestimation of dose could be detected in case of CBCT based dose calculation due to a significant reduction of the outer contour of the phantom in CBCT images. Concerning dose calculation, carried out by utilizing the Monte Carlo Algorithm (MCA), the representative Gamma Indexes were higher and more pronounced.

Discussion

In the frame of this study, the feasibility of CBCT based dose calculation for ART under certain conditions could be confirmed. However, one has to bear in mind that image artifacts highly influence the accuracy of dose calculation relying on CBCT images. A possible opportunity for handling this problem might be advanced image reconstruction algorithms in order to trace artifacts already in frequency space and hence minimize image errors. Additionally, an autosegmentation tool may be used in order to autocontour artifact affected volumes and assign well defined HUs in order to bypass their influence on dose calculation.

Consequently, CBCT images can be used for positioning correction on the treatment table as well as for contemporaneous adaptive re-planning. Further studies that show the dosimetric advantage of ART are planned for CRT and IMRT for H&N- and pelvis cases.

Zusammenfassung

Hintergrund

Cone Beam Computed Tomography (CBCT) am Linearbeschleuniger wird momentan vorwiegend zur Korrektur von Positionierungsungenauigkeiten des Patienten eingesetzt. Weitere Verwendungsmöglichkeiten dieser zusätzlichen Bilddatensätze bieten sich in der adaptiven Strahlentherapie (ART) an. Durch repetitives Imaging kann auf anatomische Veränderungen (z.B. durch Änderung des Bestrahlungsplanes) reagiert und die Therapie schonender gestaltet werden. In dieser Arbeit soll in einem ersten Schritt untersucht werden, inwieweit CBCT Daten für die Dosisberechnung in der ART geeignet sind.

Material und Methoden

Alle Untersuchungen wurden mit dem CBCT am Elekta-Linearbeschleuniger Synergy® in der Abteilung für Strahlentherapie an der Medizinischen Universität Wien/AKH Wien durchgeführt. Die zum Dosisvergleich herangezogenen Bilder wurden mittels eines konventionellen Multi Slice CT Scanners von Siemens (*Siemens VolumeZoom*) aufgenommen. Für zwei Kalibrierphantome (CATPhan® und Gammex® RMI) wurden sowohl in den CT- als auch in den CBCT- Aufnahmen die mittleren Hounsfield Einheiten (HU) für materialspezifische Einsätze ermittelt. Weiters wurde der Einfluss der zur Bildakquisition eingestellten Parameter (Röhrenspannung, mAs, Kollimation und Filterung) auf die HUs bestimmt und HU/ED (Elektronendichte) Korrelationskurven der diversen klinischen Protokolle für die Dosisberechnung erstellt. Im Zuge einer ausgedehnten Qualitätssicherung wurden wichtige Parameter der Bildqualität in CBCT Bildern untersucht, anhand welcher unter anderem die Korrelationskurven auf ihre Langzeitstabilität getestet wurden. Anschließend wurden Dosisverteilungen für einen Anterior – Posterior (AP) Bestrahlungsplan mittels des Bestrahlungsplanungssystems iPlan® von BrainLAB berechnet und die dosimetrische Genauigkeit im Vergleich zum PlanungsCT evaluiert. Zur Inbetriebnahme von iPlan® waren Basisdaten für die einzelnen Strahlqualitäten des Bestrahlungsgeräts gemessen und erfolgreich implementiert worden. Zur Abschätzung dieser Genauigkeit wurde eine Gamma Evaluierung

durchgeführt. Diese Gammaevaluierung wurde an Datensätzen eines inhomogenen Verifikationsphantoms mit Korkeinsätzen vollzogen.

Resultate

Die Bildqualitätssicherung zeigte, dass eine prinzipielle Anwendung von CBCT Datensätzen für ART denkbar ist. Im Vergleich zum CT zeigten die experimentell gewonnen HU/ED Korrelationskurven beider Kalibrierphantome Abweichungen von durchschnittlich 27 % in ED. Im Gegensatz zu Korrelationskurven, welche auf dem Gammex® RMI phantom beruhten, zeigten die CATPhan® Kurven einen parallelen Verlauf und große Ähnlichkeit zu den gewünschten CT Kurven. Aus diesem Grund wurden sie zur nachfolgenden, auf CBCT Daten beruhenden Dosisberechnung herangezogen. Die Forderung nach verlässlichen und zeitlich stabilen Korrelationskurven konnte für ein Protokoll (*Image Quality* Protokoll) gezeigt werden. Im Verlauf von 10 Monaten wurde eine maximale Schwankung um den jeweiligen HU Mittelwert der Einsätze im CATPhan® Phantom von 30 HUs beobachtet. Ein Vergleich der Tiefendosisverteilungen für CT- und CBCT- gestützte, auf dem Pencil Beam Algorithmus (PBA) beruhende Dosisberechnung zeigte mittlere Gammawerte von bis zu 0.51 und maximale Gammawerte von ≤ 0.94 . Sichtbar war eine Unterschätzung der Dosis im CBCT im Dosisaufbau, welche auf eine Reduzierung der Außenkontur zurückführen ließ. Für laterale Dosisprofile kam es zu mittleren Gamma Indizes von 0.24 und maximalen Werten von 0.87. Der Vergleich der Dosisberechnungen, welche mittels des Monte Carlo Algorithmus (MCA) durchgeführt wurde, zeigten tendenziell höhere Gamma Werte.

Diskussion

Diese Arbeit zeigt, dass CBCT Aufnahmen unter gewissen Bedingungen für die Dosisberechnung eingesetzt werden können. Es muss jedoch berücksichtigt werden, dass die auf CBCT beruhende Dosisberechnung stark durch Bildartefakte beeinflusst ist. Durch verbesserte Rekonstruktionsalgorithmen könnten Bildfehler bereits im Fourierraum als solche erkannt und demzufolge minimiert werden. Außerdem könnte ein Autosegmentierungstool verwendet werden, um von Artefakten durchsetzten Volumina spezifische HU zuzuweisen und somit den störenden Einfluss der Bildartefakte auf die Dosisberechnung zu umgehen.

Ein CBCT Datensatz kann folglich sowohl zur Positionskorrektur des Patienten am Behandlungstisch als auch gleichzeitig zur adaptiven Planung herangezogen werden. Weitere Studien, welche dosimetrische Vorteile der ART in Bezug auf den Patienten zeigen sollen, sind für CRT und IMRT im Kopf- Hals- und Beckenbereich geplant.

Curriculum Vitae

Personal Information

Name: Johannes Hopfgartner
Date of Birth: 27.11.1984 Bruneck/Südtirol/Italy
Address: Laudongasse 22/3, 1080 Wien/Austria
Telephone: 0043-(0)650-8724644

Education

1990 - 1995 Elementary school: J-Bachlechner, Bruneck
1995 - 1998 Grammar school: Dr. J-Röd, Bruneck
1998 – 2003 Classical Gymnasium Nikolaus Cusanus, Bruneck
School leaving examination (Matura): July 2003

2003 - 2004 Studies of Astronomy, University Vienna
2004 – 2009 Studies of Physics, University Vienna

October 2008 - June 2009 Diplomathesis: First Steps of Implementation of Image Guided
Adaptive Radiation Therapy, AKH Vienna

Working Experience

July-August September Schwaerzer GmbH (Forge and Metalworking)
(1999 – 2006) Noeckler OHG (Forge and Metalworking)

July-August-September GKN Sinter Metals AG (Metal Industry)
(2007 – 2008)

Skills

Foreign languages: English, Italian
Presentation: May 2009 ÖGMP annual meeting 2009, Krems
Oral presentation: Adaptive Radiotherapie basierend auf In-Room CT Bildgebung – praktische Implementierung und Untersuchungen zur Genauigkeit